

Utah State University

DigitalCommons@USU

---

All Graduate Theses and Dissertations

Graduate Studies

---

5-1998

## Small Strike-Slip Faults in Granitic Rock: Implications for Three-Dimensional Models

Siang Joo Lim

Follow this and additional works at: <https://digitalcommons.usu.edu/etd>



Part of the [Geology Commons](#)

---

### Recommended Citation

Lim, Siang Joo, "Small Strike-Slip Faults in Granitic Rock: Implications for Three-Dimensional Models" (1998). *All Graduate Theses and Dissertations*. 5624.

<https://digitalcommons.usu.edu/etd/5624>

This Thesis is brought to you for free and open access by the Graduate Studies at DigitalCommons@USU. It has been accepted for inclusion in All Graduate Theses and Dissertations by an authorized administrator of DigitalCommons@USU. For more information, please contact [digitalcommons@usu.edu](mailto:digitalcommons@usu.edu).



SMALL STRIKE-SLIP FAULTS IN GRANITIC ROCK: IMPLICATIONS  
FOR THREE-DIMENSIONAL MODELS

by

Siang Joo Lim

A thesis submitted in partial fulfillment  
of the requirements for the degree

of

MASTER OF SCIENCE

in

Geology

Approved:

UTAH STATE UNIVERSITY  
Logan, Utah

1998

## ABSTRACT

Small Strike-Slip Faults in Granitic Rock: Implications  
for Three-Dimensional Models

by

Siang Joo Lim, Master of Science

Utah State University, 1998

Major Professor: James P. Evans  
Department: Geology

The geometry and mineralization features of small left-lateral strike-slip faults and associated fractures in Lake Edison Granodiorite of the central Sierra Nevada, California, were examined in order to model the three-dimensional structure of strike-slip faults. These faults, which are reactivated joints, were also examined to determine fault sizes, starting joint size, and evidence for fluid flow.

The associated secondary fractures are usually found in the dilational quadrants of fault-tip regions. The longest fault-segment trace is 32.14 m; the longest joint trace is 22 m. The joint population length ( $l$ ) is represented by a power-law distribution ( $l^{-n}$ ) and it is  $l^{-1.22}$ . The fault-segment distributions for individual fault populations and the uncensored fault-segment distribution are  $l^{-0.23-0.79}$ , and the compiled fault-segment distribution is  $l^{-1.18}$ . The data on fracture and fault spacing, along with the joint power-law distribution, will aid in the simulation and analysis of fault evolution.

The splay-fracture traces in the faults are linear at depth and the average splay-fracture angle is  $39^\circ \pm 13^\circ$ . The dihedral angle of the splay plane and fault

plane ranges from 20° to 65°. There is a high concentration of splay fractures near the fault. As distance increases perpendicular from the fault, the splay-fracture spacing increases, and splay-fracture frequency decreases. The splay trace length distributions have a high short trace length concentration with a rapid decrease of long trace lengths. The maximum trace length of multiple splay-fracture groups is restricted by their distance orthogonal to the fault trace. The three-dimensional relationship between the splay-fracture plane and fault plane can be inferred from these data.

When present, mineralized quartz appears largely as lenses and few as single continuous veins along the faults. No consistent pattern exists between fault displacement and the locations and dimensions of quartz cavities. There is no visible damage zone near the fault terminations or around the faults. Microstructures in the fault zone consist of cataclasites and patchy gouges, and zones of dynamically recrystallized fault walls. The three-dimensional geometry, along with quartz cavity distribution and thin section analysis, has led to the conclusion that fluid migrates vertically among the faults and fractures.

(148 pages)

In memory of Kim Robeson

## ACKNOWLEDGMENTS

First and foremost, I would like to thank Jim Evans for his guidance, patience, and support throughout the entire study. Jim was willing to listen to ideas and problems associated with the project and life in general. He is the best graduate advisor anyone could ever wish for. I thank Tom Lachmar and Kevin Hestir for serving as committee members and provided guidance on making my thesis better. I would also like to thank all of the Geology Department faculty and staff and they made my study at Utah State University a pleasant experience.

I thank Kim Robeson, my partner in crime, who had done the trailblazing in thesis writing, endured my countless rumblings, and generously shared his ideas and data. Discussions with Colby VanDenburg and Yang Junming were very helpful. I thank Torrey Copfer and Alan Hochberg for their assistance in the field. I thank Amy Hochberg for her editing and her tasty pasta. I would like to thank Vincent Jefferies for cutting the rock samples for thin-section preparation and John Greg Solum for doing the x-ray diffraction. I thank all of the third floor graduate students who have put up with me and my neverending fiddling with the computers without resorting to violence. Last but not least, I thank my parents and my wife for their continuous faith and support.

This study is supported by a grant from the U.S. Department of Energy Office of Basic Energy Science (Grant # DE-FG-03-95ER14526) awarded to Jim Evans.

Siang Joo Lim

## CONTENTS

vi

	Page
ABSTRACT .....	ii
DEDICATION .....	iv
ACKNOWLEDGMENTS.....	v
LIST OF TABLES .....	viii
LIST OF FIGURES .....	ix
INTRODUCTION .....	1
GEOLOGIC SETTING.....	7
PREVIOUS WORK.....	12
TERMINOLOGY.....	23
METHODOLOGY.....	27
Surveying Procedures.....	27
Three-Dimensional Data Calculation .....	29
Thin-Section Preparation .....	31
Three-Dimensional Data and Visualization.....	31
OBSERVATIONS .....	33
Small Splay Structures .....	33
End View of Splay Structures.....	33
Elevation View of Splay Structure.....	39
Summary for Small Splay Structures .....	46

	vii
Small Faults, Fault Groups, and Fault Populations.....	49
Single Fault: KJ-4.....	49
Single Fault: BJ-B.....	58
Fault Group: KJ-5.....	60
Kip Camp Fault Groups.....	63
Bear Creek Fault Group.....	68
Fault Populations.....	74
Kip Camp Fault Population.....	77
Reflecting Bowl Fault Population.....	79
Summary for Reflecting Bowl and Kip Camp Fault Populations.....	84
Thin-Section Observations.....	90
Summary of Observations.....	100
DISCUSSION .....	104
Faults, Secondary Fractures, and Fluid Flow.....	107
Splay-Fracture Geometry and Fault Mechanical Models.....	109
Splay-Fracture Geometry and Three-Dimensional Conceptual Models .....	114
CONCLUSIONS.....	118
REFERENCES.....	120
APPENDICES .....	128
Appendix A Three-Dimensional Data Computation.....	129
Appendix B Ribbon Diagram Color Code .....	134



## LIST OF TABLES

Table		Page
1	THE DIHEDRAL ANGLES BETWEEN FAULT PLANES AND SPLAY-FRACTURE PLANES.....	48
2	STATISTICS OF FAULT KJ-4 NORTH BLOCK AND SOUTH BLOCK SPLAY TRACELENGTHS.....	56

## LIST OF FIGURES

Figure		Page
1	Secondary fracture models from (a) Adam and Sines (1978), (b) Germanovich et al. (1994), (c) Scholz (1990).....	3
2	Martel and Boger (1998) conceptual model of a penny-shaped strike-slip fault and secondary fractures.....	4
3	Geologic map showing the Bear Creek region of the Mount Abbot quadrangle and the study site locations.....	8
4	Aerial photograph of the Bear Creek study area.....	10
5	The three stages of faulting in the Bear Creek area as described in Martel et al. (1988) .....	15
6	The ideal model for process-zone faulting .....	17
7	Diagram illustrating variations of fault surface shape .....	20
8	Major types of fractures based on the relative displacement of the material on opposite sides of the fracture.....	24
9	Diagram illustrating types of fractures discussed in this study .....	25
10	End view of fault SF-2 splay structure.....	34
11	Photographs of fault SF-2 splay structure.....	35
12	Histogram of fault SF-2 splay tracelength .....	36
13	Histogram of fault SF-2 <i>scan-a</i> and <i>scan-b</i> splay-fracture spacing.....	37
14	Three-dimensional visualization of fault SF-2 end-view splay structure .....	38

		x
15	Elevation view of fault SF-1 splay structure .....	40
16	Histogram of fault SF-1 splay tracelength .....	41
17	Plots of splay length vs normalized fault distance along fault SF-1 .....	42
18	The extent of splay-fracture damage on the horizontal surface of fault SF-1.....	43
19	Histogram of fault SF-1 <i>scan-a</i> and <i>scan-b</i> splay-fracture spacing .....	43
20	Distribution of fault SF-1 horizontal surface splay angle.....	44
21	Plots of splay angle vs normalized fault distance for fault SF-1.....	45
22	Distribution of fault SF-1 vertical surface splay angle (splay plane dip).....	46
23	Three-dimensional visualization of fault SF-1 elevation view splay structure .....	47
24	Map of fault KJ-4 showing fracture geometry, mineralization, and offsets.....	50
25	Three-dimensional visualization of fault KJ-4.....	51
26	Histogram of fault KJ-4 <i>scan-a</i> and <i>scan-b</i> splay-fracture spacing.....	53
27	Histogram of fault KJ-4 splay tracelength.....	54
28	Plots of splay tracelength vs normalized fault distance for fault KJ-4.....	55
29	Distribution of fault KJ-4 splay angle .....	56
30	Plots of splay angle vs normalized fault distance for fault KJ-4 .....	57
31	Map of fault BJ-B.....	59
32	Photo of a right-lateral step within fault BJ-B with foliated granodiorite on its right side.....	60
33	Map of fault KJ-5 showing interconnecting fractures between faults.....	62

		xi
34	Histogram of fault KJ-5 splay angle .....	63
35	Map of Kip Camp fault groups .....	65
36	Distribution of Kip Camp splay angles .....	66
37	Bear Creek Camp fault group map .....	70
38	Distribution of Bear Creek Camp splay angles .....	71
39	Histogram of Bear Creek Camp fault step complex splay tracelengths .....	71
40	Histogram of Bear Creek Camp fault step complex <i>scan-a</i> and <i>scan-b</i> splay fracture spacing .....	72
41	Map of Kip Camp outcrop showing geometry and orientations of fault and joint traces and kink bands .....	75
42	Map of Reflecting Bowl outcrop showing geometry and orientations of fault and joints .....	76
43	A top left view of a modified Segall and Pollard (1983a) Kip Camp map showing a gentle topographic rise in three-dimensional visualization .....	78
44	Plot of the frequency of Kip Camp fault segment tracelengths, with a power-law distribution .....	78
45	Histogram of Kip Camp fracture spacing at two scanline locations .....	79
46	Histogram of Kip Camp fault spacing at two scanline locations .....	80
47	Plot of the frequency of Reflecting Bowl fault segment tracelengths, with a power-law distribution .....	81
48	Zipper crack-like band without a central fracture in Reflecting Bowl .....	82
49	Histogram of Reflecting Bowl fracture spacing at three scanline locations .....	83
50	Histogram of Reflecting Bowl fault spacing at three scanline locations .....	84

		xii
51	Photo and map of Reflecting Bowl rhombochasm.....	85
52	Histogram of Reflecting Bowl splay angle.....	86
53	Plots of mineralized cavity dimensions vs fault displacement.....	87
54	Frequency of joint length at Reflecting Bowl exhibiting a power-law distribution with $n = -1.219$ and $r^2 = 0.78$ .....	88
55	Frequency of all mapped fault segment tracelengths showing a power-law distribution with $n = -1.18$ and $r^2 = 0.57$ .....	89
56	Frequency of all fully exposed fault segment tracelengths showing a power-law distribution with $n = -0.79$ and $r^2 = 0.41$ .....	90
57	Histogram of Kip Camp fault segment tracelength.....	91
58	Histogram of Reflecting Bowl fault segment tracelength.....	91
59	Thin section of KJ4/296 from fault KJ-4.....	93
60	Photomicrograph of RS-7 from a Reflecting Bowl fracture showing a feldspar crystal that is not offset by the fracture.....	94
61	Thin section of KJ1/396D from fault KJ-1B.....	95
62	Thin section of RS-6B from a Reflecting Bowl fault.....	97
63	Thin section of BJS-2 from fault BJ-10.....	98
64	Thin section of BJ-28D from a right-lateral step in fault BJ-B.....	99
65	Histogram of compiled splay-fracture angles from all mapped splay fractures.....	102
66	Left-lateral slip patches that have induced splay cracks on an adjacent fault.....	111
67	A fully rendered fault plane and splay fractures fitting the surface trace of a strike-slip fault and its secondary fractures.....	116

A1 A fracture trace diagram with markings and x and y profiles of the topography..... 131

## INTRODUCTION

Faults are a natural phenomenon and are ubiquitous throughout the Earth's crust. They have profound influences on human activities such as resource extraction, waste deposition, and hazard migration. The hydraulic properties of faults influence the migration, trapping, and production of hydrocarbons and the extraction of geothermal fluids. Faults form pathways for groundwater flow that could transport undesirable chemicals and radionuclides from waste sites to the biosphere and guide the deposition of ore-forming fluids. On the other hand, faults could act as barriers to fluid pathways (e.g., Yielding et al., 1997). Previous work has shown that mineral veins associated with faulting underscores the hydrologic importance of the faults (e.g., Long and Witherspoon, 1985; Smith et al., 1990). Human constructions, such as habitats, dams, and bridges, have to be carefully engineered to account for the presence and properties of fault.

A three-dimensional characterization of the structure of faults and the resulting permeability of a rock mass will enhance the identification of potential resource/disposal sites and spur the development of better resource extraction and waste containment technologies. The growth and initiation processes of fault systems begin with small faults and blossom into a complex three-dimensional structure through the linking of small faults (Martel et al., 1988). To fully appreciate the complex structure of fault systems, this project will examine small faults in detail and lead to an understanding of the nucleation and growth of small faults in three dimensions. This study is made possible in part by the development of computer technology to create and depict three-dimensional objects.

Faulting is a complex process and it commonly destroys much previous evidence of its initiation as displacement accumulates. The current understanding of shear fracturing nucleation, propagation, and linkage in crystalline rock is based on

experiments (Brace and Bombolakis, 1963; Reches and Lockner, 1994; Moore and Lockner, 1995) and theoretical works (Segall and Pollard, 1987; Martel and Pollard, 1989; Cowie and Scholz, 1992), augmented by field studies (Segall and Pollard, 1983a; Granier, 1985; Martel et al., 1988; Bürgmann and Pollard, 1994). Faults are three-dimensional structures and most strike-slip fault studies, and almost all field and mechanical analyses, are conducted in a two-dimensional plane typically perpendicular to the fault plane and parallel to the slip direction. Relatively few studies have been conducted on a fault's structural variation with depth in order to guide modeling and mapping.

In recognition of this void, laboratory studies on the three-dimensional shape of a strike-slip fault and its secondary fractures have been conducted (Adams and Sines, 1978; Germanovich et al., 1994) and theoretical models developed (Scholz, 1990; Martel and Boger, 1998). There are two prominent published laboratory-based works by Adams and Sines (1978) and Germanovich et al. (1994) on the secondary fractures around a single three-dimensional shear fracture in plastic blocks (Figs. 1a and 1b, respectively). Scholz (1990) and Martel and Boger (1998) both provided conceptual three-dimensional models arising from mechanics and laboratory studies, respectively (Figs. 1c and 2, respectively).

Adams and Sines (1978) based their conceptual model on compression tests on penny-shaped cracks in rectangular plastic samples (Fig. 1a). The cracks were machined into the surface of two polymethylmethacrylate plastic (PMMA) blocks that were later glued together, having the cracks along a seam. The samples were subjected to unmeasured uniaxial compressive stress with the compression axis at  $45^\circ$  to the cracks. Germanovich et al. (1994) also based their conceptual model on uniaxial compression tests on PMMA samples (Fig. 1b). They formed their penny-shaped crack inside the sample using a laser and there was no seam produced. The



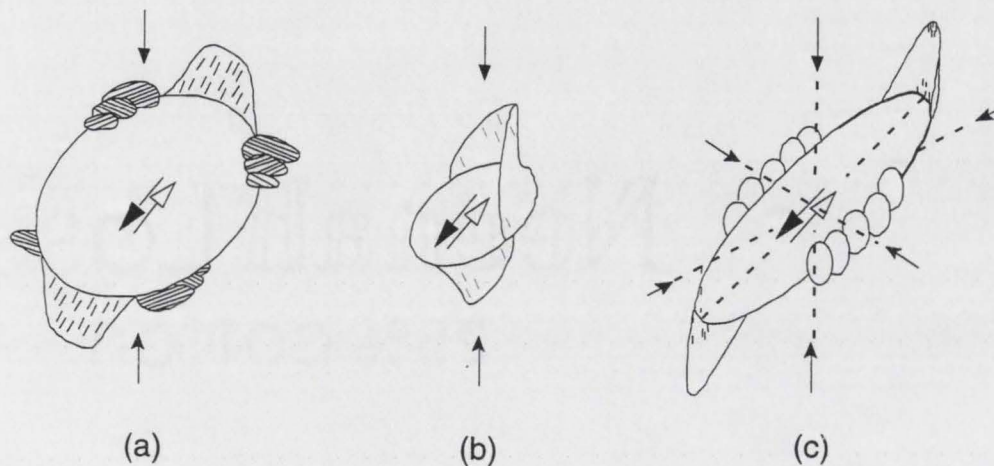


**Figure 1. Secondary fracture models from (a) Adam and Sines (1978), (b) Germanovich et al. (1994), (c) Scholz (1990). Small solid arrows shows orientations of applied compressive stresses. The main fault surface is shown dipping relative to the maximum compressive stress and the secondary fractures are about parallel to the axis of maximum compression. The secondary fractures in the Adams and Sines (1978) model consist of two large continuous fractures and a number of smaller fractures touching the rim of the fault. In the Germanovich et al. (1994) model, there are only large continuous fractures touching the perimeter of the fault. In the Scholz (1990) model, it has two large continuous fractures touching the perimeter of the fault and two zipper crack bands, on the other fault axis, propagating past the fault plane.**

laser produced a powder residue on the crack surface and the sample was immersed in liquid nitrogen to achieve brittleness prior to the compression test. Scholz (1990) distilled his model (Fig. 1c) from published reports and experiment results. Martel and Boger (1998) based their three-dimensional conceptual model (Fig. 2) on the numerical and analytical results of cohesive zone theory (CZT). All models share these similar secondary fracture characteristics:

- 1) The fractures touched the perimeters of the penny-shaped fracture.
- 2) The fractures at propagation tips are larger than fractures along the edges.
- 3) The fractures are about parallel to the axis of maximum compression.

In all of the models except the CZT model (Martel and Boger, 1998) a significant portion of fault is intersected by the larger fractures and the fractures form

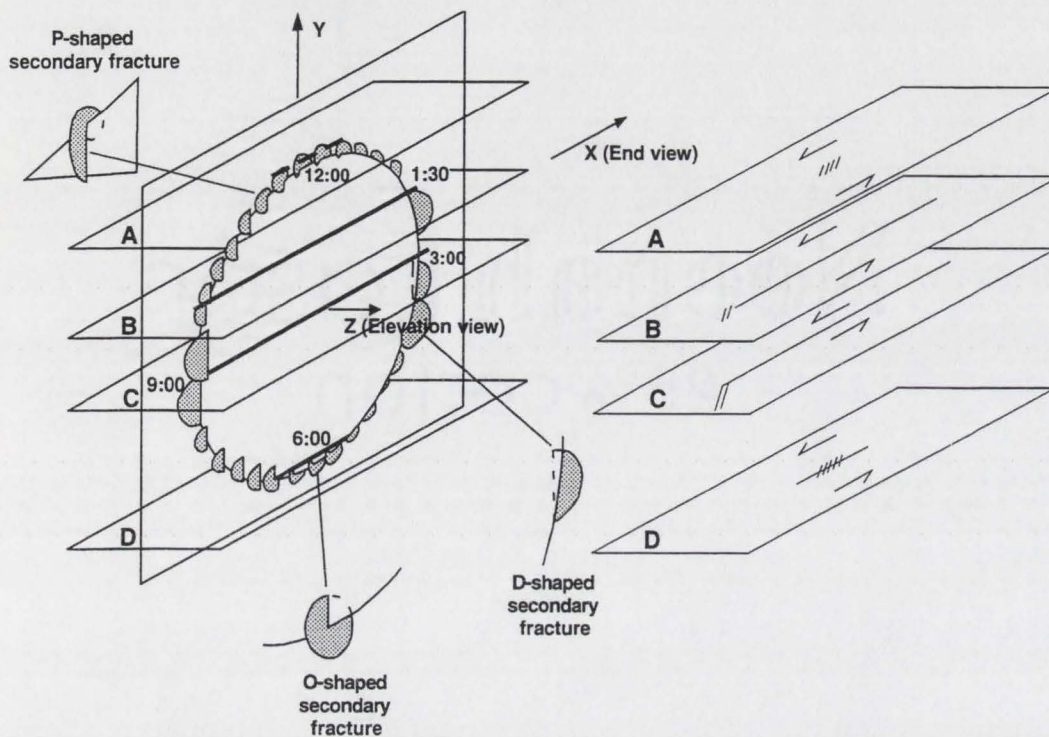


**Figure 2.** Martel and Boger (1998) conceptual model of a penny-shaped strike-slip fault and secondary fractures. Planes A to D indicate four levels of exposures perpendicular to the fault. Fractures in planes A and D are known as zipper crack bands, and they occur only at the 12 and 6 o'clock positions of the penny. Note that the plane A band has no central fracture and plane D does. Planes B and C are the fault and its splay fractures. The cohesive zone is the ring of secondary fractures around the penny. The x-direction is the end view and z-direction is the elevation view.

a continuous curved surface. Both Figure 1a and 1b have no zipper crack band and Figure 1c cannot have a zipper crack band without a central fracture. In addition, the secondary fractures in Figures 1a and 1b did not propagate across the fault plane.

These studies have ignited the debate over which of two competing fracture mechanics models for strike-slip faults, the linear elastic fracture model (LEFM) and the cohesive zone theory (CZT), could better account for the secondary fracture localization. Some outcrop observations cannot be reproduced in the laboratory due to limited sample size or applied boundary conditions (confining pressures, strain rates, temperatures, and other factors). Laboratory experiments would validate or

reject the theoretical models but the ultimate judgment on the success of the model would be how well it correlates with field data.

This project investigates the spatial layout of small left-lateral strike-slip faults in an area with high topographic relief in order to examine the three-dimensional geometry of fracture/fault structures. Fault characteristics such as attitudes, splay points, tips, distribution of veins and mineralizations, topographic details, and other secondary fracture geometries were documented. The data will provide geologic and geometric constraints for future fault-growth modeling (Hestir et al., 1997).

In this thesis, I:

- 1) provide an overview of three-dimensional strike-slip models,
- 2) present the field data of mapped single faults and several small map areas with fault populations,
- 3) examine a small faults to infer their three-dimensional geometry, which is important for mechanical modeling,
- 4) determine the three-dimensional fracture/fault geometry in order to gain insight on how a hydrologically connected fracture/fault system develops, and
- 5) evaluate populations of fractures and faults to estimate joint size and fault size, and the relationship between fault sizes and fluid flow. The small fault populations will provide data sets from which three-dimensional modeling can generate starting joint size and fault size.

An overview of the general structure and geometries of a strike-slip fault and its secondary fractures was presented in this section. This is followed by a general geologic overview of the Bear Creek drainage within the Mount Abbot quadrangle, California, with emphasis on the study region. Next is a review of previous studies that examine small strike-slip faults, fault growth models, mechanics of fault process,

and three-dimensional structures related to strike-slip fault modeling. A terminology section for the fractures is included to clarify the terminology deployment, followed by a methodology section to explain the processes used to obtain and process the collected data.

The data are presented in the observation section, which is broken down into four subsections. First is the description of splay fractures in two planes, which is followed by the description of small single faults and groupings of small multiple faults. This is followed by observations of small fault populations and then an analysis of thin sections. A comparison between previous work and this study is given in the discussion section, which is then followed by the conclusions.

The overall objectives of my work are to:

- 1) investigate the procedures of getting the optimal three-dimensional faults and fractures information from field data,
- 2) compare my data with the mechanical model established by Martel and Boger (1998), and
- 3) aid in the stochastic model conditional coding established by Hesitr et al. (1997).

## GEOLOGIC SETTING

The study site is the Bear Creek drainage of the Sierra Nevada, which is within the John Muir Wilderness Area, California (Fig. 3). The faults studied are in the Lake Edison granodioritic pluton, a Cretaceous, fine- to medium-grained, homogeneous, equigranular biotite-hornblende granodiorite with subhedral mafic monzonite in which titanite is generally abundant (Lockwood and Lydon, 1975). The Lake Edison Granodiorite is elongated in a northwest-southeast direction and is a part of the John Muir Intrusive Suite. The pluton is roughly 50 km long and shaped like a dog bone—narrow in the middle with leucogranitic bulges at the ends (Bateman, 1992). The Lake Edison Granodiorite intrudes the Mount Givens and Lamarck Granodiorites of the John Muir Intrusive Suite, and an unassigned Graveyard Peak leucogranite (Bateman, 1992). The pluton was later intruded by the Round Valley Peak Granodiorite and the Mono Creek Granite of the John Muir Intrusive Suite (Bateman, 1992). The study site is in the narrow part of the pluton, and it is flanked by Mono Creek Granite to the east and Lamarck Granodiorite to the west. Bateman (1992) suggested that the Lake Edison Granodiorite was emplaced as a relatively low-temperature, viscous magma, and that it was rather mobile and emplaced during an episode of regional extension. In addition, it is thought that the southern bulge could be the result of a regional thrust that forced the eastward expansion of crystallizing viscous magma (Bateman, 1992).

This intrusive body has U-Pb zircon dates of 89.8 and 93.2 Ma (Stern et al., 1981), and  $88 \pm 1$  Ma (Tobisch et al., 1995). The K-Ar dates on the pluton's biotite has yielded 77 Ma and 82 Ma, and on hornblende of 85 Ma (Kistler et al., 1965; Evernden and Kistler, 1970; Stern et al., 1981). A  $^{40}\text{Ar}/^{39}\text{Ar}$  hornblende date yielded 86.8 Ma (Tobisch et al., 1995). It was discovered that weathered joints in the

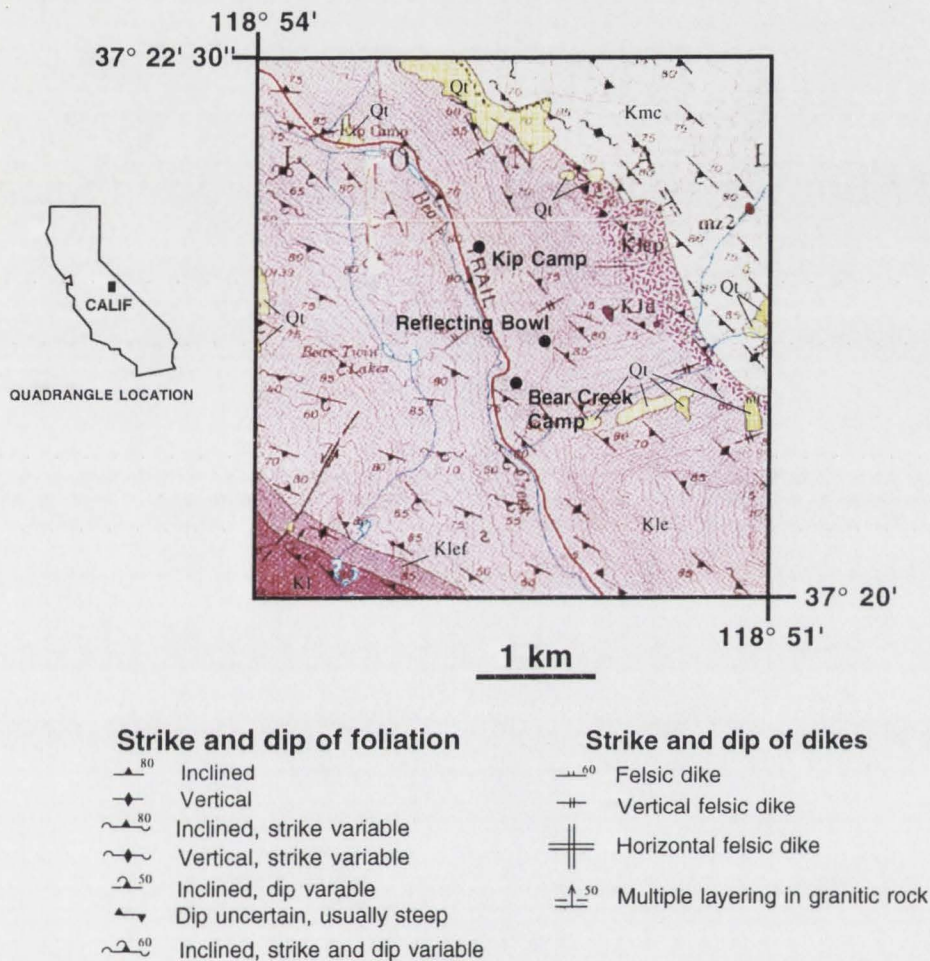


Figure 3. Geologic map showing the Bear Creek region of the Mount Abbot quadrangle and the study site locations. Kl – Lamarck Granodiorite, Kle – Lake Edison Granodiorite, Klef – Lake Edison Granodiorite fine-grained facies, Klep – Lake Edison Granodiorite porphyritic facies, Kmc – Mono Creek Granite, Kjd – Undifferentiated mafic rocks, mz2 – areas of extensive quartz-epidote-chlorite mineralization, Qt – Talus, Qal – Alluvium. Map taken from Lockwood and Lydon (1975).

northern Sierra Nevada that extended into unaltered rock were filled with Eocene auriferous gravels, indicating the joints were at least as old as Eocene in age (Bateman and Wahrhaftig, 1966; Bateman, 1992). Bateman (1992) suggested that the joints probably formed during the Late Cretaceous as the Sierra Nevada was being uplifted, eroded, and cooled.  $^{40}\text{Ar}/^{39}\text{Ar}$  radiometric dating of muscovite grains found

in faults indicated the faults occurred about 72 Ma and 75–79 Ma, suggesting that faulting occurred after the pluton was emplaced (Segall et al., 1990).

Although there were no direct geobarometric and thermometric measurements on the Lake Edison Granodiorite, emplacement depths and pressures have been estimated for several surrounding plutons. Noyes et al. (1983) estimated the nearby Eagle Peak and Red Lake plutons of the John Muir Intrusive Suite were emplaced at a pressure of about 100 MPa and at a temperature of about 300 °C. The neighboring Mount Givens pluton (87–90 Ma) was estimated to have been emplaced under a pressure of 330–350 MPa and at a temperature of 300–700 °C (Renne et al., 1993; Tobisch et al., 1993). Thermometry and geobarometry data from the Lamarck Granodiorite yielded a temperature 650 °C and pressures of 320 MPa (Reed and Hathaway, 1994).

From the above geobarometric studies, the pressures during emplacement are in the general range of 100–400 MPa, equivalent to the weight of 4–15 km of rock (Bateman, 1992). The emplacement temperature was probably around 300–700 °C. Segall and Pollard (1983b) believed the joints in the Mt Givens Granodiorite postdate the pluton intrusion and probably formed at depths shallower than the emplacement depth. Given the close proximity, similar ages, and compositions of these plutons, we can assume that the Lake Edison Granodiorite has approximately the same values.

The study sites have well-exposed faults due to glaciation and sparse vegetation, and they are located on the west-aspect of the glaciated Bear Creek drainage with slopes of 5°–35°. Lockwood and Lydon (1975) first recognized the pervasive system of northeast-trending joints developed in the Lake Edison Granodiorite that influence prominent erosional features such as linear stream channels, long deep trenches, or parallel lines of trees and shrubs (Fig. 4). The present Sierra Nevada glaciated topography has changed very little since the Ice Age

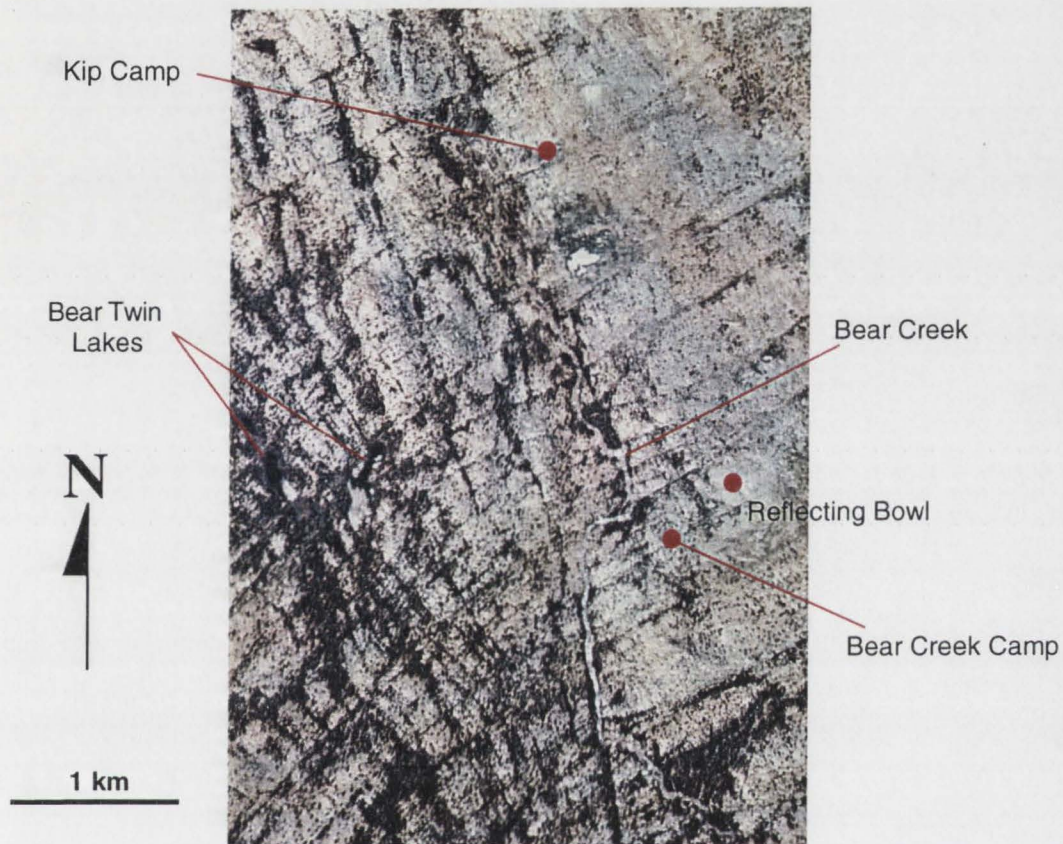


**Figure 4.** Aerial photograph of the Bear Creek study area. It shows WSW-striking lineaments marked by vegetation and small channels that follow strike-slip fault zones developed along previously formed joints in the area. USDA air photo, project no. S1-11, flight no. 06019-11-76, taken on 7-2-76.

(Lockwood and Lydon, 1975). Additionally, the study area has not been disturbed by any mining or excavation activities.

The faults (reactivated joints) in this area are small-scale (tens of meters) to intermediate-scale (hundreds of meters) (Segall and Pollard, 1983a; Martel, 1990). The faults are steeply dipping, left-lateral strike-slip faults in the Cretaceous pluton. They have widths of 0.1–10 mm and relative strike-slip displacements of up to 2 m, and apparently have not encountered any significant subsequent deformation (Segall and Pollard, 1983a; Martel et al., 1988). Linked echelon faults could be several hundred meters in length and could have accommodated left-lateral displacements of



several meters (Martel et al., 1988). The granodiorite has quartz and felsic dikes that, along with the slip vectors on many of the faults, provide constraints on the amount of slip. However, not all joints accommodated shear displacement and some of these unslipped joints are parallel to the reactivated joints and fault zones (Segall and Pollard, 1983a; Segall et al., 1990).

The joints are mineralized with epidote, chlorite, biotite  $\pm$  sphene  $\pm$  calcite  $\pm$  zeolites (Segall and Pollard, 1983a; Segall et al., 1990). Segall et al. (1990) found textural evidence that the zeolites were deposited after the other fracture-filling minerals. The faults and their secondary fractures have the same minerals plus quartz (Segall and Pollard, 1983a; Segall et al., 1990). Some joints and faults have alteration halos and the granodiorite in the faults and fault zones is highly altered (Segall and Pollard, 1983a; Segall et al., 1990). Hornblende is replaced by chlorite, epidote, and sphene, and biotite is replaced by chlorite, whereas feldspars are altered to epidote and mica (Segall et al., 1990). The mineralization in the area indicates there was a connected paleohydrologic flow system.

## PREVIOUS WORK

Previous studies of strike-slip faults have been conducted in the study area and various mechanical models for strike-slip fault initiation have been proposed on the basis of these studies. They are briefly highlighted and summarized below. The implications of the previous investigations in light of the results presented here will be discussed in a later section of this thesis.

Segall and Pollard (1983a) provided the first detailed study of the left-lateral strike-slip faults and related structures of the Mount Abbot quadrangle. Through microstructural analysis, they concluded that the left-lateral faults nucleated and grew from cooling joints formed in the pluton, not from initial shear fracturing, and fault-fill minerals showed both brittle and ductile deformation. The boundaries of the faults are usually very sharp, and the granodiorite outside the fault appeared undeformed by the stress (Segall and Pollard, 1983a). Splay cracks trending  $25^\circ \pm 10^\circ$  counterclockwise to the fault plane were interpreted to have propagated out from near the ends of the fault plane in the direction of maximum compressive stress (Segall and Pollard, 1983a). The splay fracture probably formed in the dilational quadrant at the fault tip, and there is no evidence of dilational fractures on the clockwise side (compressive quadrant) of the fault plane (Segall and Pollard, 1983a). In fact, in the compressive quadrant, there is foliated, ductilely deformed granodiorite (Bürgmann and Pollard, 1994). Additional microstructural analysis showed the splay fractures formed as dilational fractures (Segall and Pollard, 1983a). The investigators proposed that the faults propagated through the linking of secondary fractures and resulted in larger faults. Segall and Pollard (1983a) and Davies and Pollard (1986) showed that the strike-slip faults and joints are locally deflected into monoclinical kink bands and are interpreted as conjugate to the left-lateral displacement across the

faults and fault zones, which is consistent with the northeast-oriented maximum compression inferred for left-lateral slip on these small faults. Another mechanism that could be responsible for the kink bands is the Rosy Finch shear zone that extends through the neighboring Mono Creek Granite. Tikoff and Saint Blanquat (1997) suggested that there was active dextral shearing in the Rosy Finch shear zone during Mono Creek Granite (possibly Lake Edison Granodiorite) emplacement.

In a related study, Segall and Pollard (1983b) looked at joint formation in nearby granitic rocks, and through field and microscopic observations they concluded an extensional origin for the joints. The spacing between joints was not uniform and was not controlled by variations in joint geometry or rock type with depth (Segall and Pollard, 1983b). Field measurements of extensional strain accommodated by joint dilation, joint length, and the spatial density of joints were used to estimate initial driving stress and fracture toughness (Segall and Pollard, 1983b). The driving stress (the sum of remote stress and internal fluid pressure) and fracture toughness estimates are 1–40 MPa and  $0.04\text{--}4 \text{ MPa}\cdot\text{m}^{1/2}$ , respectively, and are compatible with existing laboratory fracture data (Segall and Pollard, 1983b). Segall and Pollard (1983b) suggested the abundance of short joints relative to longer joints was probably the result of elastic interaction between adjacent joints and shorter joints were prevented from further propagation by their long siblings, which consumed most of the strain energy in the rocks. Segall and Pollard (1983b) suggested that the use of a power law distribution on joint-length data provided a good fit.

Building on the previous two Segall and Pollard studies (1983a, 1983b), Martel et al. (1988) sought to explain fault zones that are in the midst of reactivated joints. These simple fault zones are typically 0.5–3 m wide, hundreds of meters long, and laterally displace dikes up to ~10 m (Martel et al., 1988). The simple fault zone is characterized by two subparallel faults that bound a tabular volume of fractured

rock inside the zone, and outside the bounded zone the rock is relatively unfractured (Martel et al., 1988). The boundary faults are where most of the displacement occurred, and the faults are characterized by cataclastic textures and brittlely deformed quartz (Martel et al., 1988). Martel et al. (1988) postulated that the simple fault zones developed as abundant oblique fractures linked small faults side-to-side. They found that the fault zones consist of non-coplanar segments a few tens of meters long that join at steps or bends, indicating that the fault zones grew in length as non-coplanar faults linked end-to-end (Fig. 5). The simple fault zones have prominent straight fracture traces that strike  $20^{\circ}$ – $60^{\circ}$  counterclockwise from the boundaries, but near the bends they have gentle S-shaped traces that are almost orthogonal to the boundaries (Martel et al., 1988).

Martel (1990) provided refined terms for fracture features, which are utilized in my terminology section, and argued against the use of the Riedel shear classification for the fault zones in the Mount Abbot quadrangle. Martel et al. (1988) and Martel (1990) have determined that the oblique-striking splay fractures within the faults formed after the parallel faults. The timing of parallel fractures (*y*-shears) generated in simple shear experiments came late in the fracture genesis [see Figures 8 and 9 in Martel (1990)]. The splay fractures were also determined to have originated as dilatant fractures and not as shear fractures. In addition, the spatial organization of fault zone fractures does not fit the Riedel classification well.

From the above, the faults in the Bear Creek area probably started as cooling joints and a change in the stress orientation caused the nucleation, linkage, and propagation of small faults (Segall and Pollard, 1983a; Martel et al., 1988; Martel and Pollard, 1989; Martel, 1990). Three stages of deformation have been proposed (Martel et al., 1988) (Fig. 5). East-northeast striking, subparallel, steeply dipping dilatant joints first developed from pluton cooling, and contained undeformed epidote

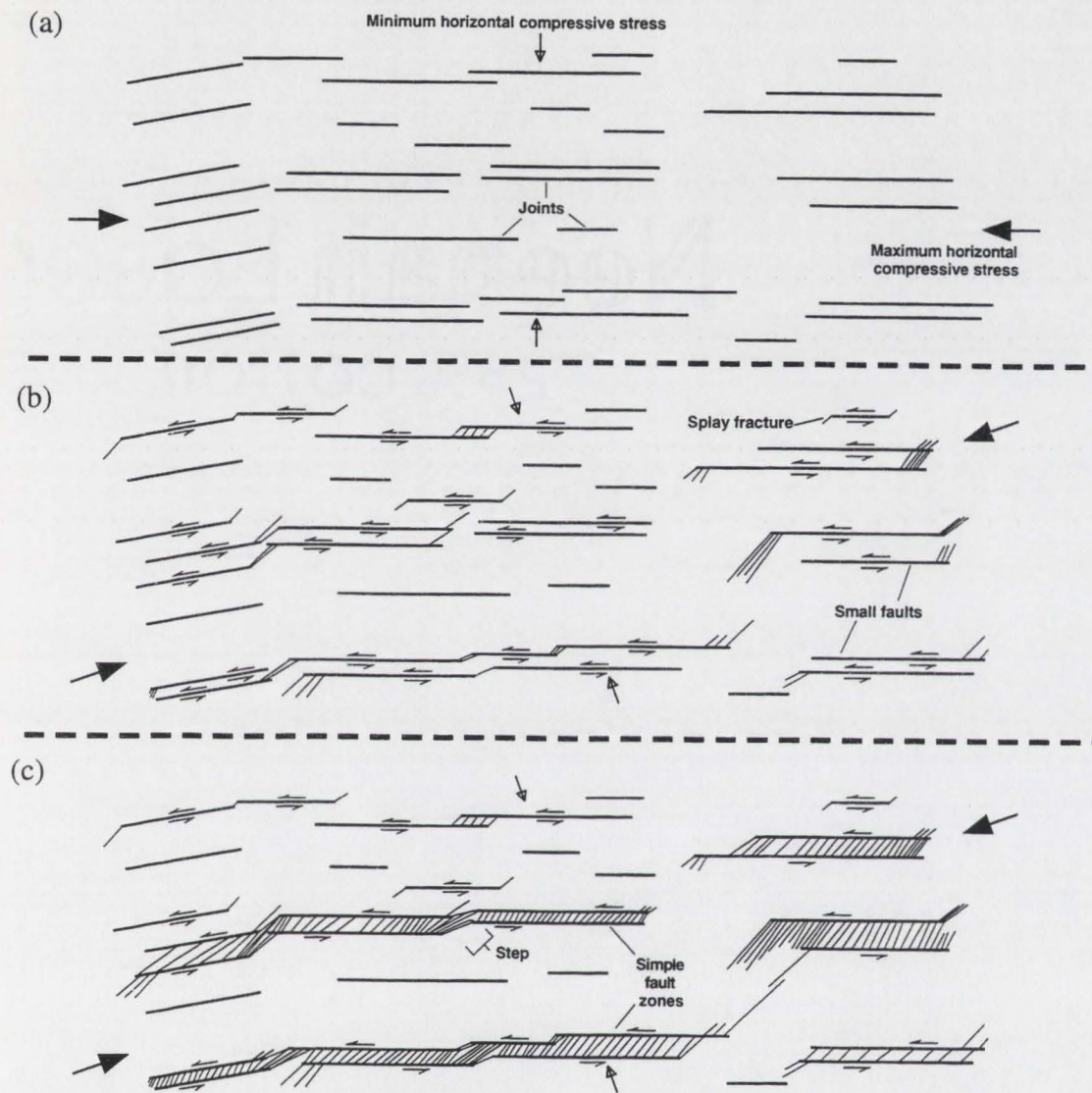


**Figure 5. The three stages of faulting in the Bear Creek area as described in Martel et al. (1988). (a) Opening of joints. (b) Development of small left-lateral faults. (c) Development of simple fault zones. Modified from Martel (1990).**

and chlorite (Segall and Pollard, 1983a). A subsequent change in the stress field is proposed to have resulted in joints slipping as strike-slip faults (Segall and Pollard, 1983a). Left-lateral strike-slip motion on the cooling joints resulted in dilatant fractures (splay cracks) growing from near the ends of each fault counterclockwise from the trace of the fault (Segall and Pollard, 1983a). Splay cracks and faults,

which strike northeast, appear to have grown from the ends of faults at this stage, and were filled with epidote, chlorite, and quartz (Segall and Pollard, 1983a). The faulted joints did not propagate into intact granite, but were linked by the splay cracks (Segall and Pollard, 1983a). The final stage of deformation was the simple fault zone, and it is characterized by two nearly parallel faults (boundary faults) containing fractured rocks within and relatively unfractured rocks outside the boundary faults (Martel et al., 1988). The left-stepping echelon faults are linked by splay cracks and right-stepping echelon faults are linked by ductile deformation (Martel et al., 1988). This process is otherwise known as the fracture-linked model (Robeson, 1998).

Although Segall and Pollard (1983a) and Martel (1990) have convincingly shown that fault initiation in the study area is the result of joint reactivation, we must examine other fault-growth models in examining three-dimensional fault structures to determine if other models might help explain structures not seen in two dimensions. Beside the earlier mentioned models (Adams and Sines, 1978; Martel, 1990; Scholz, 1990; Germanovich et al., 1994; Martel and Boger, 1998), the other major fault growth model is the process-zone model (Cox and Scholz, 1988; Scholz, 1990; Vermilye and Scholz, 1998) (Fig. 6), which has been demonstrated in laboratory experiments (Reches and Lockner, 1994). Reches and Lockner (1994) based their experiment on triaxial compression tests on homogeneous Westerly Granite, and used the acoustic emission from stress-induced microcrack growth to "observe" fault nucleation and growth. It is assumed that under the preloading condition, microcracks within the homogeneous rock are sparse and random. Under triaxial loading conditions, tensile microcracks nucleate randomly, and the local stress of an opening crack helps trigger the dilatation of a neighboring crack and creates a region of closely spaced cracks; this is the process zone (Reches and Lockner, 1994). At sufficient stress, microcracks begin to interact and propagate in an unstable and

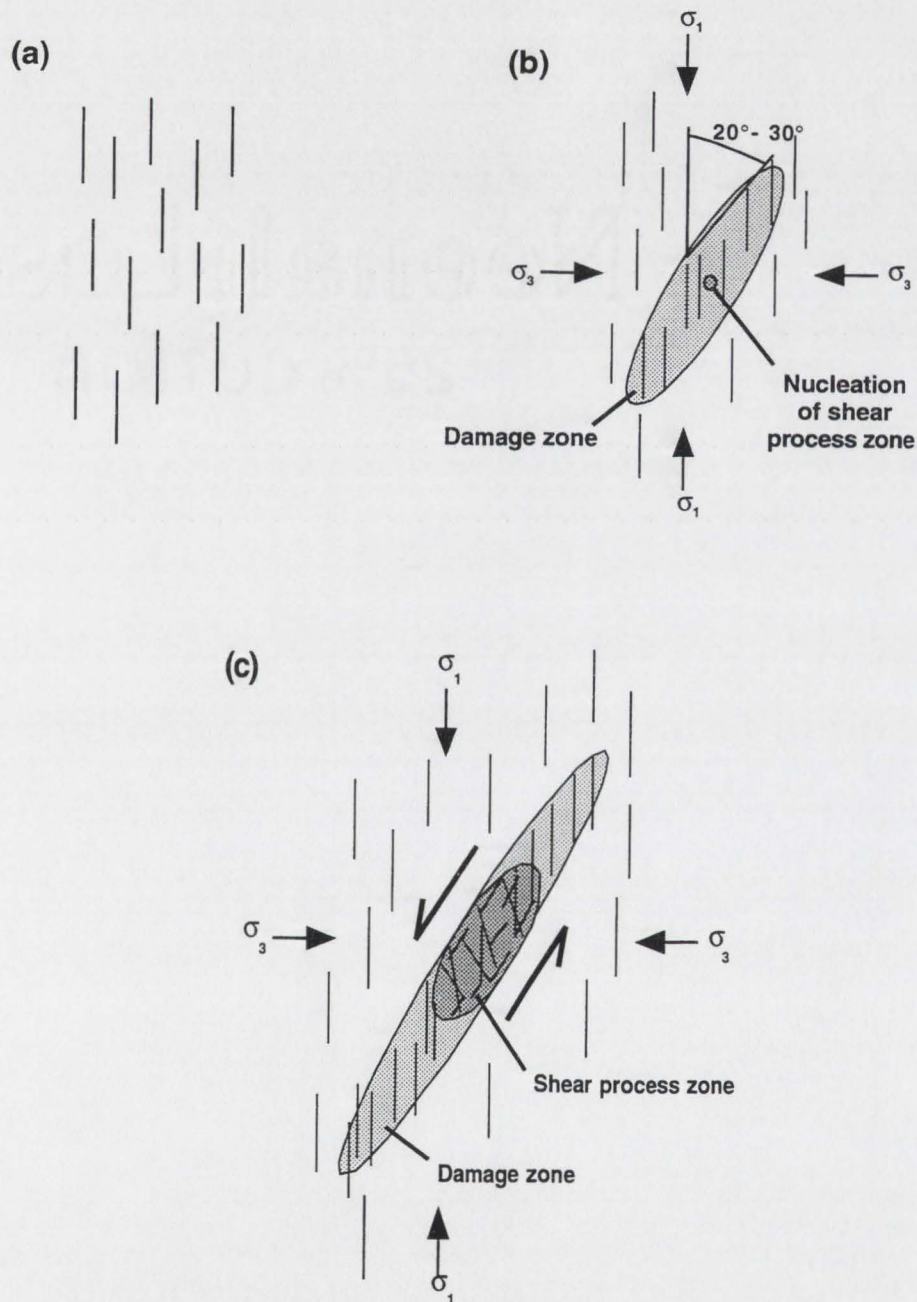


Figure 6. The ideal model for process-zone faulting. (a) Preloading: sites of randomly distributed potential microcracks. (b) At substantial loading: nucleation and local increase of crack density lead to the development of a damage zone by dilating cracks and inducing opening of neighboring cracks. (c) Shear process-zone: the weakened tail of the damage zone yields by crushing, buckling, and rotation of microblocks. Modified from Reches and Lockner (1994).

recursive geometry into the intact rock (Reches and Lockner, 1994). Shearing causes the interacting cracks to coalesce, forming a fault nucleus in the center of the already lengthening process zone where there is crushing, buckling, and microblock rotation, and the fault propagates in the wake of the process zone (Cowie and Scholz, 1992; Reches and Lockner, 1994; Moore and Lockner, 1995). As displacement along the fault accumulates, the shear along the fault enhances microcrack interaction in the process zone and continued frictional wearing smooths out the irregular edges of the microcracks along the fault wall, forming fault gouge (Cowie and Scholz, 1992; Reches and Lockner, 1994).

Before any three-dimensional studies of fault shape can take place, the shape of the starter crack in the three-dimensional model has to be reviewed. It could influence and dictate the initial crack shape used in experimental and theoretical modeling of fault propagation. A review of several fracture mechanics texts (Break, 1986; Lawn, 1993) on the initial shape of a starter crack proved futile. The texts simply assumed the initial shape of the crack to be circular (penny-shaped) or elliptical. A scanning-electron microscope study on polymer crack initiation revealed the starting shape to be circular or slightly elliptical (Engel et al., 1981). Kulander et al. (1990) examined both naturally and artificially induced fracture cores, and the photographs showed that the initial crack shape was circular or slightly elliptical. Nicol et al. (1996) suggested that a Mode I fracture with uniform energy absorption around the tip-line is likely to be circular in shape. After the genesis of a starter crack, the subsequent growth processes of the fracture will influence the final fracture shape. Lockner et al. (1991) conducted experiments in homogeneous granitic rock, and showed that the tip-lines advanced more rapidly in the shear direction and that the resulting fracture elongates parallel to the slip direction. The result is consistent with the notion that the dislocation loop surrounding the glide



plane of a crystal is elongated in the slip direction and that it absorbs more energy than in the screw dislocation direction (Nicol et al., 1996). It has been documented that natural fault and joint surfaces are likely to be elliptical in shape and in the case of a free and unrestricted fault, the major axis dimension is about twice the minor axis dimension (Barnett et al., 1987; Pollard and Aydin, 1988; Nicol et al., 1996; Willemse, 1997). The Nicol et al. (1996) data demonstrate that in a low-density immature fault system, regularly shaped smooth-edged ellipses are rare, and in linked faults interacting faults have very different aspect ratios before and after their linkage. The changing shape of fractures is likely to be the result of the interaction between fractures that interfered with the elastic strain fields that extend beyond the fracture tip line (Nicol et al., 1996). The final shape of a fracture could be irregular, as during fracture growth, or it could be perturbed by intersection with, or close proximity to, either the free surface or to substantial layers or bodies of incompetent rock or to other fractures (Barnett et al., 1987; Nicol et al., 1996; Willemse, 1997). Nicol et al. (1996) schematically illustrated fault shapes under different restrictions (Fig. 7).

The presence and geometry of secondary fracturing along the fault trace underscores the importance of secondary fracturing in fault development. Different models make different predictions with regards to secondary fracture geometry. Thus understanding the secondary fracturing is crucial in testing the applicability of different models. In addition, the secondary fractures are important in the development of hydrologically connected faults or fractures.

Mechanical models for secondary fracturing have been based on either linear elastic fracture mechanics (LEFM) or cohesive zone theory (CZT). The LEFM has been the most commonly used theoretical basis for fracture growth prediction (e.g., Segall and Pollard, 1987; Aydin and Schultz, 1990), but LEFM has largely been

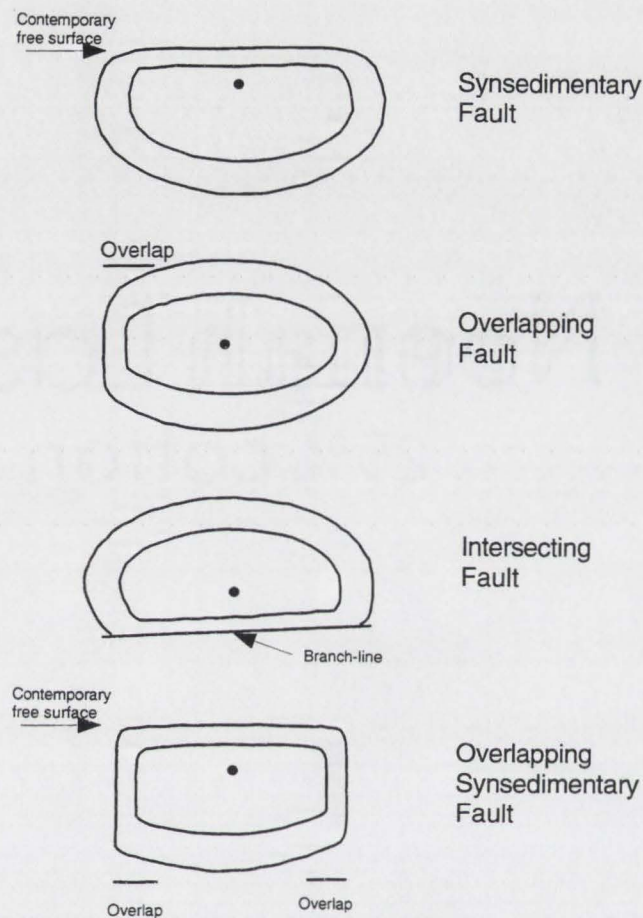


**Figure 7. Diagram illustrating variations of fault surface shape. The diversity in fault surface shapes, displacement contour patterns, and points of maximum displacement (filled dots) are due to restriction by free surfaces (a and d) and/or by adjacent faults (b, c, and d). The view is normal to the fault surface. Modified from Nicol et al. (1996).**

abandoned due to discrepancies between field observations and theory. The LEFM assumes that the material around the fracture tip is elastic but the zone in which new fracture surface is created during growth is inelastic and exceedingly small (Cowie and Scholz, 1990). This gives rise to unrealistic singular (infinite) stress concentration at the fracture edge, which no real materials can support (Martel, 1997). The near-tip stress concentration has a characteristic form that, along with the relative motion of the fracture walls, has been used to predict the fracture

propagation path (Martel and Boger, 1998). Beside the problem of singular stress, LEFM neither predicts well the orientations of secondary fractures nor does it predict well the number of secondary fractures (Martel, 1997; Martel and Boger, 1998).

Cohesive zone theory (CZT) (Dugdale, 1960; Barenblatt, 1962; Rudnicki 1980; Martel, 1997; Martel and Boger, 1998; Willemsse and Pollard, 1998) is generally able to account for the observed secondary fracture locations, number and orientations, and eliminates the problem of stress singularity. The CZT suggests that elevated stresses occur in a "cohesive zone" just behind the fracture tip that resists the opening and sliding of the fracture walls (Martel, 1997). The material outside the cohesive zone behaves as a linear elastic material, whereas the material inside the cohesive zone need not be elastic (Martel, 1997). The CZT allows secondary fractures to form behind the fault tip, but no secondary fractures can form if there is insufficient tensile stress, and under large tensile stress multiple secondary fractures can form (Martel, 1997). Cooke (1997) refined CZT and postulated that spatial variations in frictional properties along the fault may influence fracture localization. Splay fractures develop at locations with abrupt friction changes or at the fault tips when the fracture-tip friction coefficient is less than a critical value, and multiple splay fractures develop within broad zones near the tips with a linearly increasing friction coefficient towards the fault tip (Cooke, 1997). An implication of Cooke's (1997) and Martel's (1997) work is that splays would not always form at a propagating tip but could emerge off behind the tip.

The objectives of this project are to incorporate fault mechanics, fault and fracture geometries, and mineralization patterns to develop growth models, which can then be used to develop three-dimensional, mechanically based hydrologic flow systems. This would require the close examination of joints and small faults, which includes detailed mapping and documenting fault slip, fault and splay-fracture

geometries, mineralization sizes and locations, topography, and fault population data.

## TERMINOLOGY

Brittle deformation produces distinctive structures that are described in Scholz's (1990) brittle fracture mechanics text. A survey of geological literature has found that there is a broad nomenclature used by various researchers to describe the geometry and mechanical processes of joints, faults, and fractures. However, the terms are inconsistently applied, usually incomplete, or not well defined. In order to establish consistency in terminology with the strike-slip fault companion study by Robeson (1998) and in this work, definitions and descriptions of brittle structures are provided below. The terminology provided is consistent with the usage of fracture mechanics terminology as applied by Segall and Pollard (1983a; 1987), Martel et al. (1988), Martel and Pollard (1989), and Martel (1990; 1997).

Descriptive terms are used to describe the outcrop-scale fracture geometry of fractures, faults, and joints. *Fracture* is a term used to describe a discontinuity along a rock surface where there is inconclusive evidence for displacement. *Joint* is used to describe a fracture in which there is displacement normal to its surface (Pollard and Aydin, 1988), whereas for a *fault*, there is outcrop-scale evidence of shear displacement across its surface (Martel, 1990). Altered rock along the fractures, offset indicators, mineral precipitation, and rock surface textures are field evidence used to distinguish joints and faults (Segall and Pollard, 1983a; Pollard and Aydin, 1988).

Mechanical terms for fractures that describe the relative displacement motion of a fracture trace are generic and they are categorized into three modes (Fig. 8). Mode I is the tensile, or opening, mode in which the displacement is normal to the fracture trace. Mode II is in-plane shear, in which the displacement motion is in the fracture plane and perpendicular to the fracture edge. Mode III is anti-plane shear, in

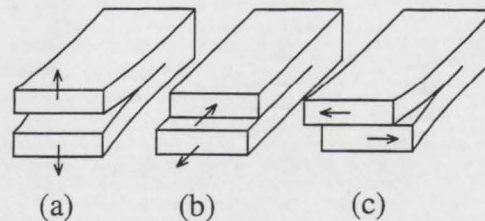


**Figure 8. Major types of fractures based on the relative displacement of the material on opposite sides of the fracture. (a) Extension, or Mode I, fracture. The relative displacement is perpendicular to the fracture. (b) Shear fracture, Mode II. Relative displacement is parallel to the fracture and perpendicular to the edge of the fracture. (c) Shear fracture, Mode III. Relative displacement is parallel to the fracture and parallel to the edge of the fracture. Modified from Twiss and Moores (1992).**

which the displacement motion is in the plane of the fracture and parallel to the fracture edge. Fractures with a Mode I + II, Mode II + III, or Mode I + III combination are known as mixed-mode fractures (Twiss and Moores, 1992). Pollard and Aydin (1988) have pointed out that displacement could vary along a fracture that incorporates various fracture modes.

In this study, only the geometric description is used to describe the fracture geometry of field observations and mechanical terms are used to describe the development of fractures. Both geometric and mechanical terms will be used to compare the theoretical models to field observations. Figure 9 illustrates the refined terminology provided below.

Individual fracture planes are not indefinite in extent. A fracture that has not broken the Earth's surface is completely surrounded by its *tip line*, which represents the limited extent of a fracture under the Earth's surface (Twiss and Moore, 1992). A *trace* is formed when a fracture intersects with the Earth's surface. A *tip* is formed when the fracture trace ends on the Earth's surface and fracture traces terminate in various ways (Twiss and Moores, 1992). A fracture could simply be terminated by

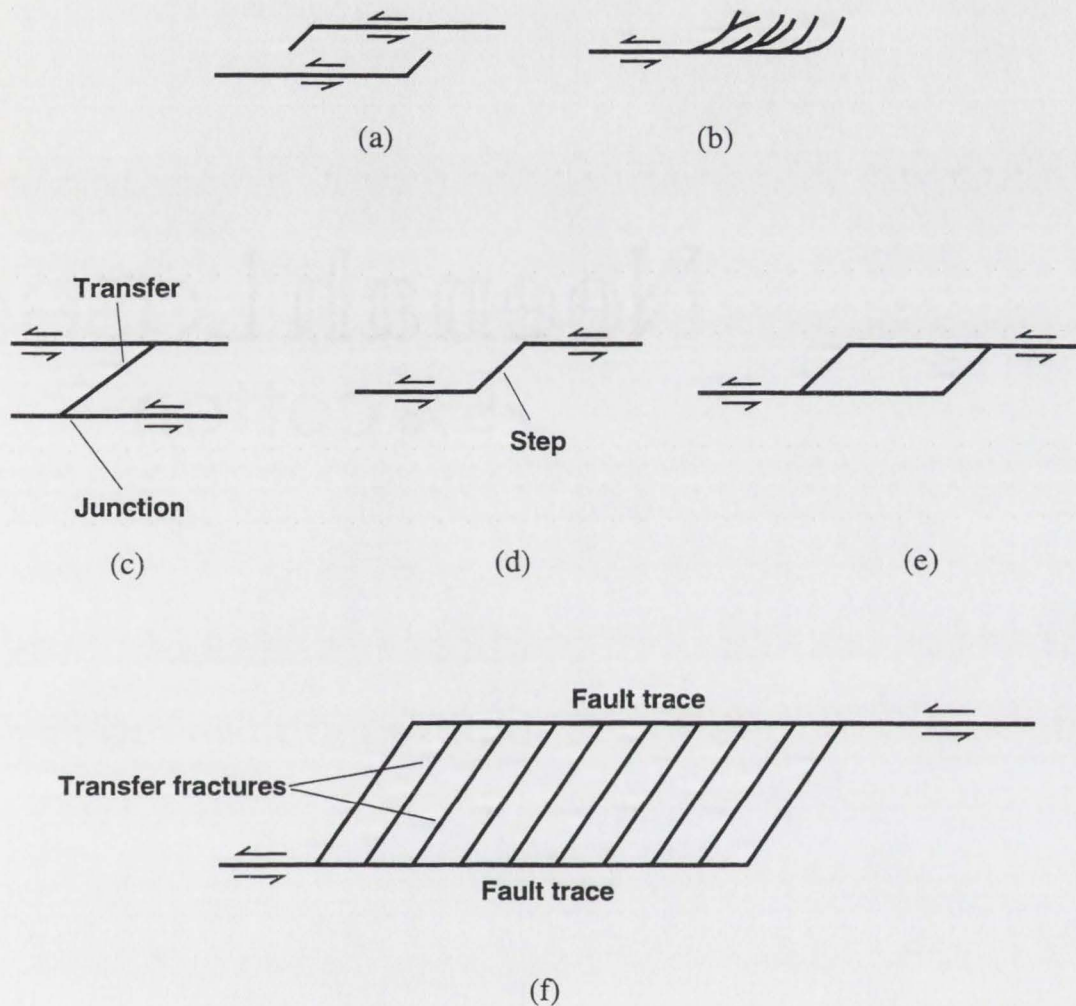


**Figure 9. Diagram illustrating types of fractures discussed in this study. (a) Splay fractures. (b) Splay fractures with diverging ends. (c) Transfer structure and its junctions. (d) Step. (e) Stepirover. (f) Fault step complex. Modified from Robeson (1998).**

intersecting with another fracture trace. *Splay fractures*, small subsidiary fracture traces branching off the main fault, may die out at their tips or intersect with another fracture trace. A splay structure may exist in an acute angle between the two diverging fracture traces. If the splays show shearing, they are classified as *splay faults*. Please note that *splay* and *splay fracture* are used interchangeably. Joints do not terminate in splay structure. They could curve or terminate at the intersection

with another joint (Pollard and Aydin, 1988). A conceptual three-dimensional geometry of a left-lateral strike-slip fault (Martel and Boger, 1998) (Fig. 2) is depicted to help with the visualization of a fault and its secondary fractures in three-dimensional space. The fractures in planes A and D are known as *zipper crack bands* and they occur only at the 12 and 6 o'clock positions of the penny. Planes B and C are the fault and its splay fractures.

A fracture that connects two parallel or subparallel, non-coplanar fractures is a *transfer structure*. The intersection of fractures is called a *fracture junction*. If the fracture traces intersect each other and continue on, this is termed as a *crossover*.

We refined the Martel (1990) definition of a *step* by stating that it is a continuous fracture trace created by two parallel to subparallel, non-coplanar fracture traces joined by a short fracture oriented obliquely from the tips of the non-coplanar fractures. In some cases, where there is an overlapping of non-planar fault traces with small splay fractures extending from the fault tips and intersecting the faults in a rhomb-shaped structure, this is classified as a *stepover*. The stepover can have numerous curvilinear, parallel to subparallel transfer structures and this feature is termed a *fault step complex*. The steps, stepovers, and fault step complexes are described as either left or right (i.e., left-step) depending on whether the step is to the left or to the right as one progresses along the fracture trace (Twiss and Moores, 1992). This description is independent of the sense of shear on the fault.

Lastly, the *simple fault zone*, which is not the focus of but is related to this study, is characterized by two near-parallel faults (boundary faults) with tabular fractured rocks between the faults (fault zone) and relatively unfractured rock outside the zone (Martel et al., 1988) (Fig. 5c).



## METHODOLOGY

### Surveying Procedures

The field investigation involved mapping the two- and three-dimensional location of each fault in detail at scales of 1:200 to 1:100, and up to 1:10 for finer details. Mapping was done with a tape and compass, a Brunton compass on a tripod, and a small handheld electronic distance meter (EDM). All measurements were made in metric units and fault attitudes given using right-hand rule convention. A detailed study of the density and orientation of fracture sets, fault tip structures, and faults were conducted to help establish the history and geometry of fault growth and fluid flow. Complete and systematic sampling of fault zone rocks was performed for later microstructural and geochemical analysis. A photographic record of possibly significant areas was made to help future laboratory study. Based on preliminary field data (Evans et al., 1996; Martel and Evans, 1996), some faults were modeled by Yang Junming and Kevin Hestir of the Utah State University Mathematics and Statistics Department. It was shown that it is important to find faults on steep slopes and in places where steps in topography occur, in order to aid computer modeling of the fault plane. Offset indicators on the faults are also highly desirable, as they would provide displacement profiles that give additional constraining parameters for fault modeling.

A labeled fault prefix was created to help indicate which study area the fault was from, such as K for Kip Camp, B for Bear Creek Camp, R for Reflecting Bowl and SF stands for secondary fractures. The alphanumeric following the fault prefix was assigned in the order which fault was mapped or inserted as a new fault was recognized.

Once a fault with the abovementioned desirable attributes had been located,

an arbitrary starting point was marked with an oil-based marker and a general fault trend direction was read and recorded. A measuring tape was stretched along the fault in its trend direction, until the fault terminated or became untraceable due to ground cover. Using the tape as the x-distance reference, fault features were chalk marked, mapped on metric graphing paper, and recorded for their locations, mineralization patterns, and other pertinent information. Any ground distance off the reference tape (y-distance) was measured with a 3-m tape measure or ruler. Every effort was made to ensure that the reading for a point on the ground was orthogonal to the referencing tape so that the feature would not be skewed on the map. The ground surface along the reference tape was divided into sections of consistent slope angle and they were measured and recorded. The slope angles were used for z-direction calculation. The y-direction slope angles for single fault mapping were usually flat in that direction and they were not a factor in three-dimensional data calculation. The described single reference line method was used on these faults: SF-1, SF-2, KJ-4, and KJ-5.

In this study, a scanline (*scan-a*) was laid out 10–20 cm away from and parallel to the fault traces to include those splay fractures that are not in contact with the fault. A second scanline (*scan-b*) was laid out at a greater distance (30–50 cm) away from and parallel to the fault trace to gather and compare splay-fracture spacing distributions. Splay tracelength was also measured to determine if there was any length variation along the normalized fault trace distance.

If there was more than one fault mapped in the area (Reflecting Bowl fault population, Kip Camp fault population, Kip Camp fault groups, Bear Camp fault groups), additional reference tapes were laid parallel and 3 m apart from the x-index reference tape. A similar process was done in the y-direction by establishing a y-index reference tape, thus creating a x-y grid mapping system. Slope angles were

measured along every reference tape and they were used to digitally generate the slope surface.

Fault attitudes and rakes of slickenlines (if exposed) were recorded and noted on the field map. Fault characteristics, including unmineralized fractures, mineralization halos, quartz mineralization, and the ubiquitous epidote/chlorite mineralization, were noted. The long and short axes of quartz mineralized cavities with widths larger than 3 mm were measured and marked on the map. Some of the described features were photographed and rock samples of various fault features were then collected, attitudes marked, recorded, and bagged.

### **Three-Dimensional Data Calculation**

Certain faults were mapped over several pieces of graph paper and were redrawn, re-scaled, and pieced together to create a complete unbroken picture in the laboratory. In turn, these maps were used to extract field coordinates for three-dimensional data conversion. The three-dimensional data were organized into an input format that allowed computerized three-dimensional structure depictions to be produced.

In order to calculate the three-dimension coordinates, the field coordinates or unprimed coordinate system ( $x$  and  $y$ ) have to be corrected for slope angle to arrive at the three-dimensional or primed coordinate system ( $x'$ ,  $y'$ , and  $z'$ ) which represents the three-dimensional coordinate system of vertical and horizontal axes. To expedite the three-dimensional data calculation, a spreadsheet file named *xyzcal.xls* was created in Microsoft Excel. I explain the computation by working out an example; the details are given in Appendix A. Be aware that this method is only feasible for a single reference line.

For three-dimensional data over a large surface area with multiple reference

lines, the above method is incapable of producing the correct z-direction values. The reference line field coordinates were converted to the primed system and the x and y coordinates of the mapped features were corrected to  $x'$  and  $y'$  with a weighted slope angle. The weighted slope angle uses the distances to two closest reference lines as a ratio and a new slope angle is obtained from the two reference lines' slope angles, i.e., closer a point is to a reference line, the greater that reference line slope angle influences the slope angle at that point. With the help of Golden Software's Surfer for Windows (v. 6), the reference line field coordinates were utilized in generating a digital surface map. I used the Kriging gridding method to generate the best fitting surface map for the field area. In turn, the mapped feature's coordinates were digitized and overlaid on the surface map, and z values were obtained from the map.

To maximize time and resources, the Segall and Pollard (1983a) Kip Camp map was selected to augment the fault population study. Using the map as a base, an initial control point was established arbitrarily, and a Brunton compass on a tripod was set up and the location and station height recorded. Map points were marked on slope breaks and at irregularly spaced intervals so that the full expression of the topography could be captured. Subsequent control points were established so that most of the map area could be covered. An EDM target was placed over the map point with the EDM receiver height above ground level noted, and the distance from the control point was read from the EDM receiver. The map point azimuth direction was read from the compass on the tripod, and the point's dip angle was read from a handheld Brunton compass. The surveyed data were computed, using common surveying calculations found in a surveying text, for digital surface map generation. The Kip Camp base map was later digitized and overlaid on the digital surface map for three-dimensional data compilation.

### **Thin-Section Preparation**

Analysis of the alteration and distribution of microstructures within fault-related rocks could help estimate the fault zone moduli (Anders and Wiltschko, 1994). Martel (1996, personal commun.) had done some modeling which suggests that some aspects of the overall geometry, such as splay crack angle, could yield information on moduli. Cooke (1997) suggested the lithologic variations, nearby structure interactions, irregular fault geometries, fluid presence, and other factors create spatially varying friction along faults that promote splay crack localization. In addition, microstructural data could help trace the history of fault zone fluid flow and fault behavior. Oriented samples were collected in the field and the samples were reoriented in a sandbox. The samples were cut based on the best available information/feature that could be obtained. Twenty-seven cut samples were shipped for thin-section preparation and returned for analysis. Photo negatives of the thin-sections were taken for the initial microstructure analysis and to give an overall sense of the sample "picture" (e.g., fabric, fracture intensity, brecciation). Photomicrographs of fracture features were shot for closeup analysis.

### **Three-Dimensional Data and Visualization**

A customized software (zview) was used to generate "*ribbon diagrams*" that depicted structures in three dimensions. The calculated three-dimensional data of a fault will plot only as a line in space; with the addition of the fault attitude, the line will transform into a plane and the fault will then be recognizable. Since the fault geometry at depth is uncertain, the rendered fault plane would only be projected shallowly into the subsurface, and hence the term "*ribbon diagram*" was coined. The ribbon diagrams are color-coded, such that splay cracks are pink and covered fault traces are green, so that different parts of the fault could be identified. The color

code is provided in Appendix B.

There were a few customized software limitations that affect the ribbon diagrams. The software only accepts the three-dimensional data and color coding inputs. The ribbon diagram only depicts vertical fracture planes since there is no input for fracture attitude. Since the joints and faults in the study area are steeply dipping ( $76^\circ$  to  $90^\circ$ ), the arbitrary fracture plane attitude depiction is acceptable, but splay fracture attitudes have moderate to steep dips. All of the depicted fractures have a fixed uniform width (which is almost infinitely thin) so mineralization data are not depicted. In addition, the lack of user input zoom-in scaling has limited the number of useful close-up visualization. The ribbon diagram does not resolve any questions related to the fracture connectivity or orientation at depth; the diagram only shows what possibilities exist for the given set of data. Despite the software limitations, any user should be able to manipulate the three-dimensional diagram at any angle to observe the structures from different perspectives. The software (zview) for depiction of three-dimensional fault structures was developed by Zheng Jinsong and further revised by Yang Junming (Zheng, 1995).

Geologic data were organized in a convenient format for mathematicians to model fault growth and to examine fault connectivity in three dimensions. Using sound geologic reasoning and statistical methods to fit data to surfaces, a best probable fault surface would then be rendered. Part of the data from this project will aid in the eventual development of hydrogeological and mathematical models that are currently being actively pursued by the Utah State University Mathematics and Statistics Department and Geology Department.

## OBSERVATIONS

In the following description of the field observations, the maps and accompanying text and ribbon diagrams depict the surface expression of the fractures and faults in the study area. The description and its diagrams do not try to dictate or direct any type, orientation, or kind of subsurface expression that the fracture may have but rather they are a goal that the three-dimensional model should try to match or emulate. From previous mapping experience, faults on steep slopes and in places where steps in topography occur were targeted to aid computer modeling of the fault plane and later comparisons of field data and fault models (Evans et al., 1996). Mapping splay fracture outcrop that has more than one plane of exposure will help enhance the understanding of the three-dimensional structure at fault ends.

This section will first focus on the splay structures that are exposed in two different planes. This will lead to observations of several small faults and small fault groups and will be followed by the description of two fault populations. Finally, this section will describe the microstructural analysis and conclude with a summary.

### Small Splay Structures

#### End View of Splay Structure

To determine the geometry of splays near a fault tip, an end-view splay structure (SF-2) was mapped in a Kip Camp outcrop (Fig. 10). Fault SF-2 was unique because it provided an opportunity to view the splay structure from the fault end towards the fault center (Fig. 11a).

SF-2 is an end view splay structure outcrop which measures 71.57 cm in height and its trace length is 1.45 m long. The main fault plane has an attitude of  $061^{\circ}/81^{\circ}\text{S}$ . The fault trace emerges from ground cover and rises 46.99 cm in height

**Figure. 10. End view of fault SF-2 splay structure. The shaded region is a vertical surface and the unshaded region is a horizontal surface. The trace has been folded out to a common view. The dashed line shows the extent of splay fracture damage on the horizontal surface. Top left of the photo is north.**



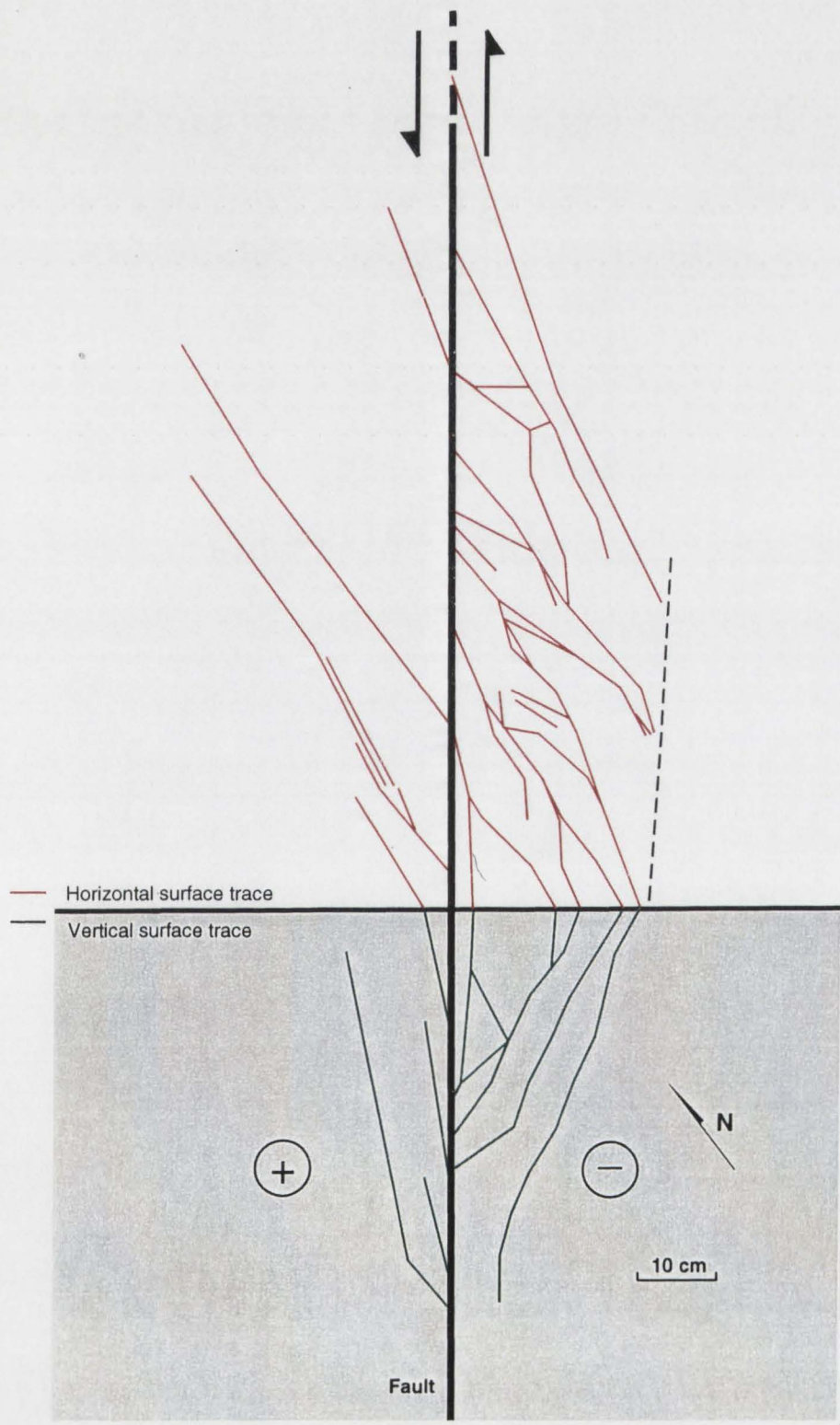




**Figure 11. Photographs of fault SF-2 splay structure. (a) Thick splay fracture veins on the vertical face. (b) Splay fracture with hairline to 1-cm thick veins on the horizontal surface. Bottom left corner of the photo is north.**

on a west-facing near vertical surface with an attitude of  $158^{\circ}/70^{\circ}\text{W}$  and it continues east in a straight line on a near horizontal surface with an attitude of  $149^{\circ}/15^{\circ}\text{W}$ . The fault is planar and less than 3 mm thick. Attitudes of  $213^{\circ}/68^{\circ}\text{N}$ ,  $202^{\circ}/64^{\circ}\text{N}$ , and  $206^{\circ}/71^{\circ}\text{N}$  were measured from the three prominent splay fractures seen in Figure 11a, and the dihedral angles between the fault and splays are  $41^{\circ}$ ,  $51^{\circ}$ , and  $44^{\circ}$ , respectively. The splay fractures are on the south block of SF-2, and the average splay angle from nine fractures on the near horizontal surface is  $36^{\circ} \pm 16^{\circ}$  counterclockwise from the trace of the fault.

The splay tracelength varies from 7 to 65 cm along the fault distance with a mean and standard deviation of  $31.1 \pm 16$  cm (Fig. 12). The splay fracture damage zone does not extend beyond 25 cm orthogonal to the fault (Fig. 10). The damage zone width appears to narrow towards the end of fault. For fault SF-2, the distance for scanlines parallel to the fault trace for *scan-a* was 10 cm and *scan-b* was 35 cm. The fault-parallel *scan-a* near fault SF-2 has a distribution of splay-fracture spacing

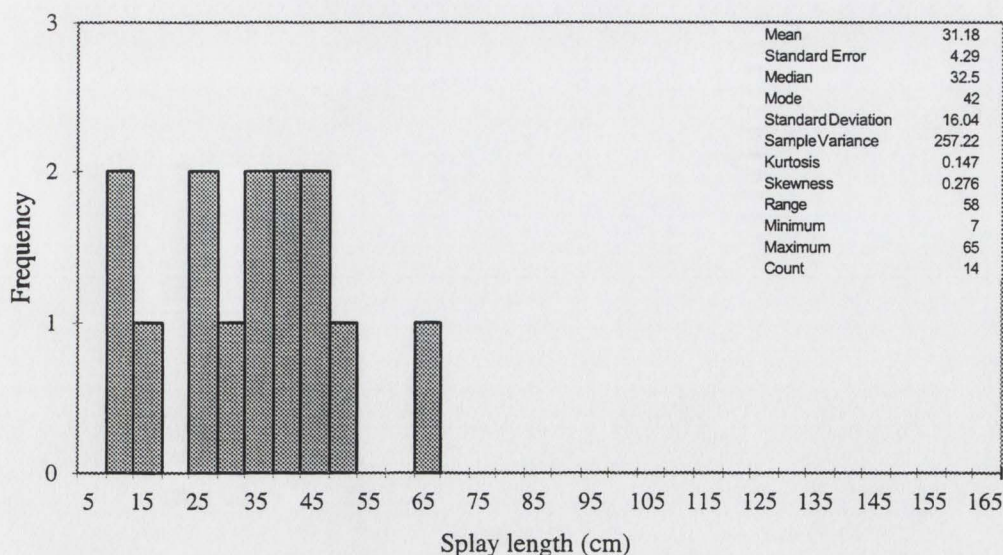


**Figure 12. Histogram of fault SF-2 splay tracelength. The chart shows an even splay tracelength distribution and the statistics of the distribution are given in the top right corner.**

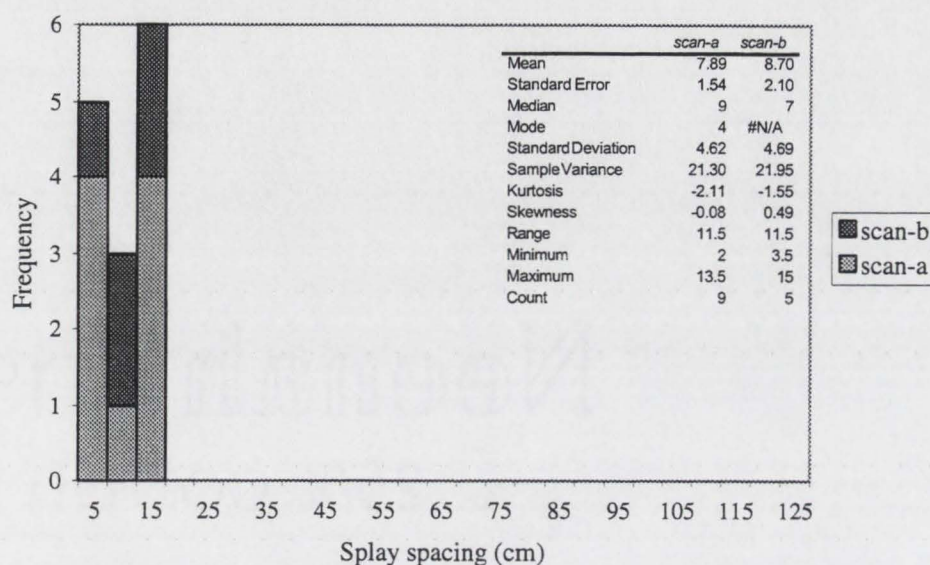


**Figure 13. Histogram of fault SF-2 *scan-a* and *scan-b* splay-fracture spacing. Scan-a scanline is placed at a distance of 10 cm away from and parallel to the fault and scan-b scanline is placed at 35 cm away from and parallel to the fault. The statistics of both scan-a and scan-b distributions are given in the top right corner.**

of 2 to 13.5 cm apart and on *scan-b*, which is farther away from fault, there is an increase in the splay-fracture spacing (from a mean of 7.9 cm to 8.7 cm) and fewer splay fractures (from 9 to 5) in the *scan-b* distribution as compared with the *scan-a* splay-fracture spacing distribution (Fig. 13). The splay fracture width is not uniform and at times much wider than the fault itself (Fig. 11b). From Figure 11a, the splay fracture plane seems to have hints of curvature with respect to depth. The fractures on the north block of SF-2 probably resulted from a kink band, as SF-2 was less than 4 m from a kink band to the east (Segall and Pollard, 1983a; Davies and Pollard, 1986). Figures 14a and 14b show the SF-2 end-view structure in three dimensions, with green ribbons representing fractures on the vertical surface and red ribbons representing fractures on the near horizontal surface.

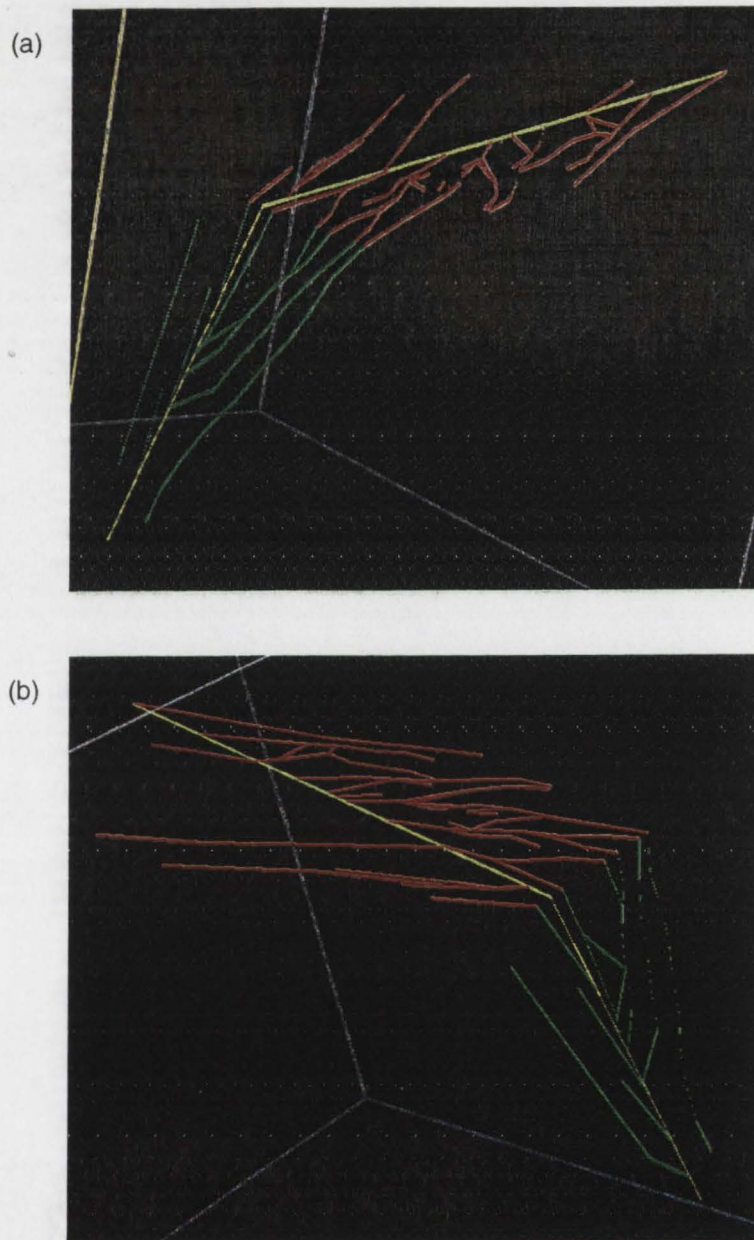


**Figure 14.** Three-dimensional visualization of fault SF-2 end-view splay structure. (a) Oblique view looking down from right top. (b) Oblique view looking down from left top.

### Elevation View of Splay Structure

An elevation view of a splay structure (SF-1) (Fig. 15a) was also mapped in the Kip Camp area. The southern block of a fault was eroded down to an average of 20 cm below the north block, exposing splay fractures in contact with the fault wall at depth in the north fault block (Fig. 15b). The near vertical surface of the north fault block is almost orthogonal to its glaciated (horizontal) companion surface. A straight scan line, with a trend and plunge with  $240^{\circ}/23^{\circ}\text{W}$  and a length of 3.85 m was set on the edge of the north fault block, parallel to the fault. The elevation-view splay structure is 3.53 m long and has an overall height of 1.58 m. The fault has an attitude of  $062^{\circ}/81^{\circ}\text{S}$  and slickenlines have a rake of  $18^{\circ}\text{E}$ . The fault surface is mineralized with epidote-chlorite. Most splay fractures have epidote-chlorite mineralization and a few splay fractures display mixed quartz and epidote-chlorite mineralization with a fracture width no greater than 3 mm. The splay fractures do not link up to other structures. The splay fracture traces are linear and a few splay fractures seem to consist of en-echelon segments. Splay tracelength on both surfaces varied throughout the length of fault.

From the horizontal surface, the splay tracelength ranged from 8 to 108 cm, with a mean of 39.8 cm and standard deviation of 24.4 cm (Fig. 16). Figure 17 was plotted to show the relationship of splay tracelength to distance along the fault trace. To accomplish this, the distance along the main fault was normalized from one end of the fault trace to an assumed location for the other end of the fault trace. The position of each splay tracelength along the normalized distance was noted, and splay tracelength and splay angle were measured. The majority of the splay lengths are below 60 cm for the first 225 cm of the normalized fault distance (Fig. 17a). After removing the splay fractures that are not in contact with the fault, Figure 17b has a result similar to Figure 17a. Both Figures 17a and 17b showed a general trend of

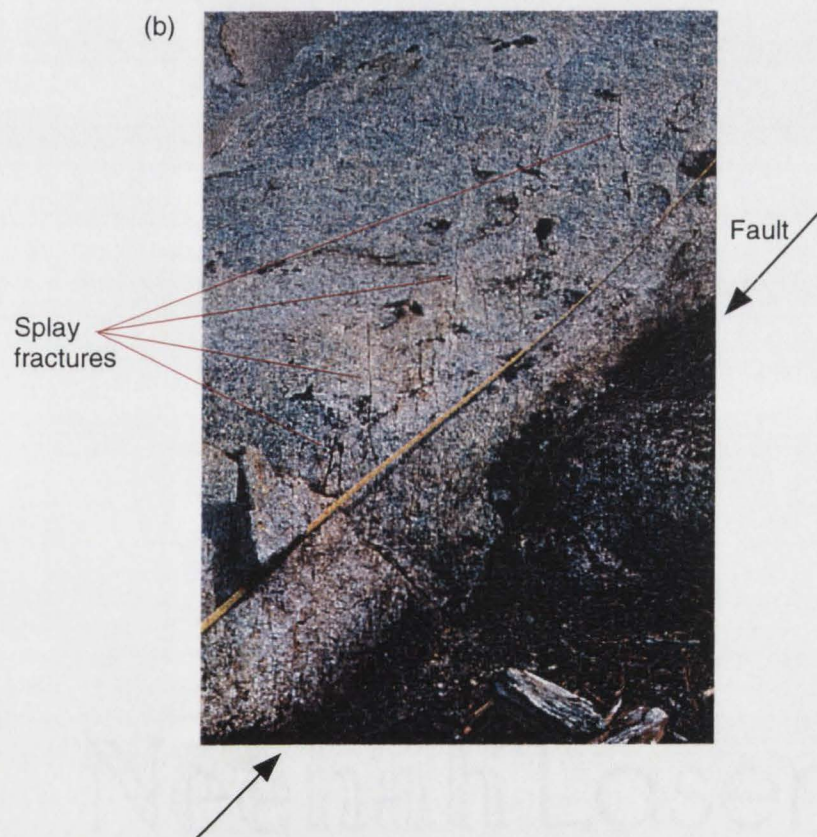
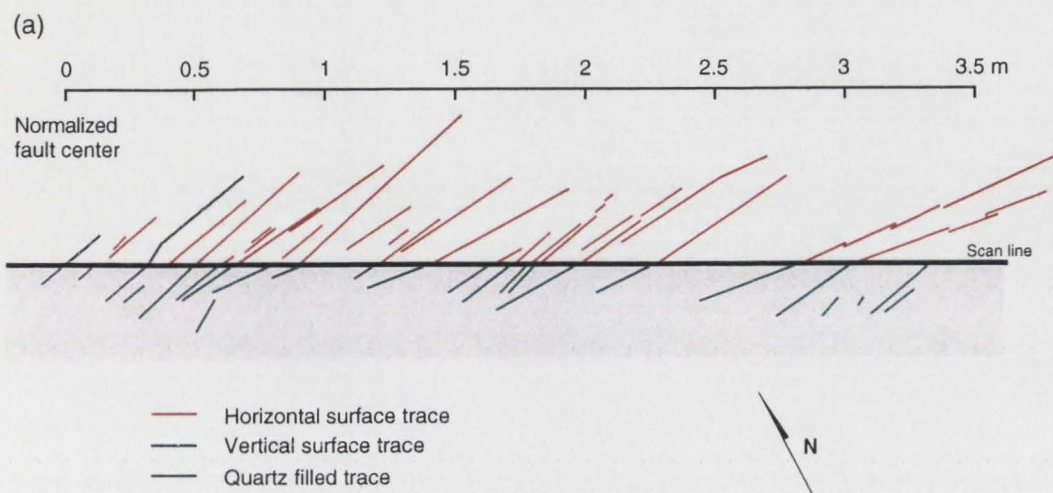


**Figure 15. Elevation view of fault SF-1 splay structure. (a) The splay fractures are exposed at a 20-cm depth on the north wall of the fault. The trace has been folded out to a common plane view and the trend and plunge of the scanline is  $240^{\circ}/23^{\circ}W$ . (b) Photo of elevation view of a splay structure.**

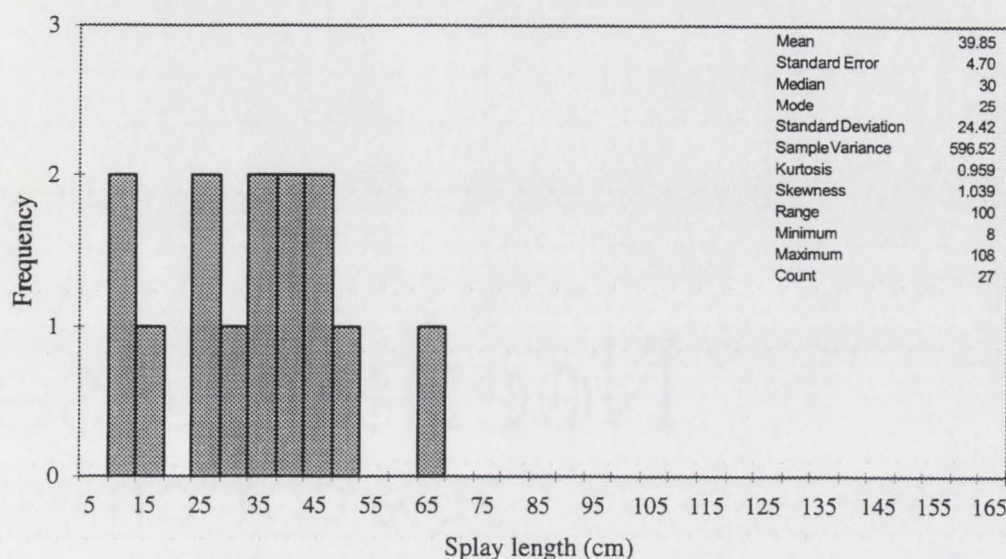


**Figure 16. Histogram of fault SF-1 splay tracelength. The chart shows a bulk of “short” splay tracelengths before the distribution tapers off for the longer tracelength. The statistics of the distribution are given in the top right corner.**

increasing splay tracelength with increasing fault distance. The splay-fracture damage zone generally widens towards the fault end (Fig. 18). Note the perpendicular distance to the fault of the damage zone is maximized in the middle of the zone.

Two scanlines were placed in the splay fractures; *scan-a* was placed 10 cm away from and parallel to the fault, and *scan-b* was placed 30 cm away from and parallel to the fault. Both splay-fracture spacing distributions have variable spacing with a mean and standard deviation of  $12.5 \pm 13.5$  cm and  $41 \pm 29$  cm, respectively (Fig. 19). The *scan-a* distribution has most of its fractures in the 5–15 cm spacing, whereas the *scan-b* distribution is more dispersed (Fig. 19). There is an increase in the splay-fracture spacing (from a mean of 12 cm to 41 cm) and fewer splay fractures (from 23 to 7) in the *scan-b* distribution as compared with the *scan-a* splay-fracture spacing distribution (Fig. 19).

The average surface splay angle is  $37^\circ \pm 7^\circ$  counterclockwise from the fault



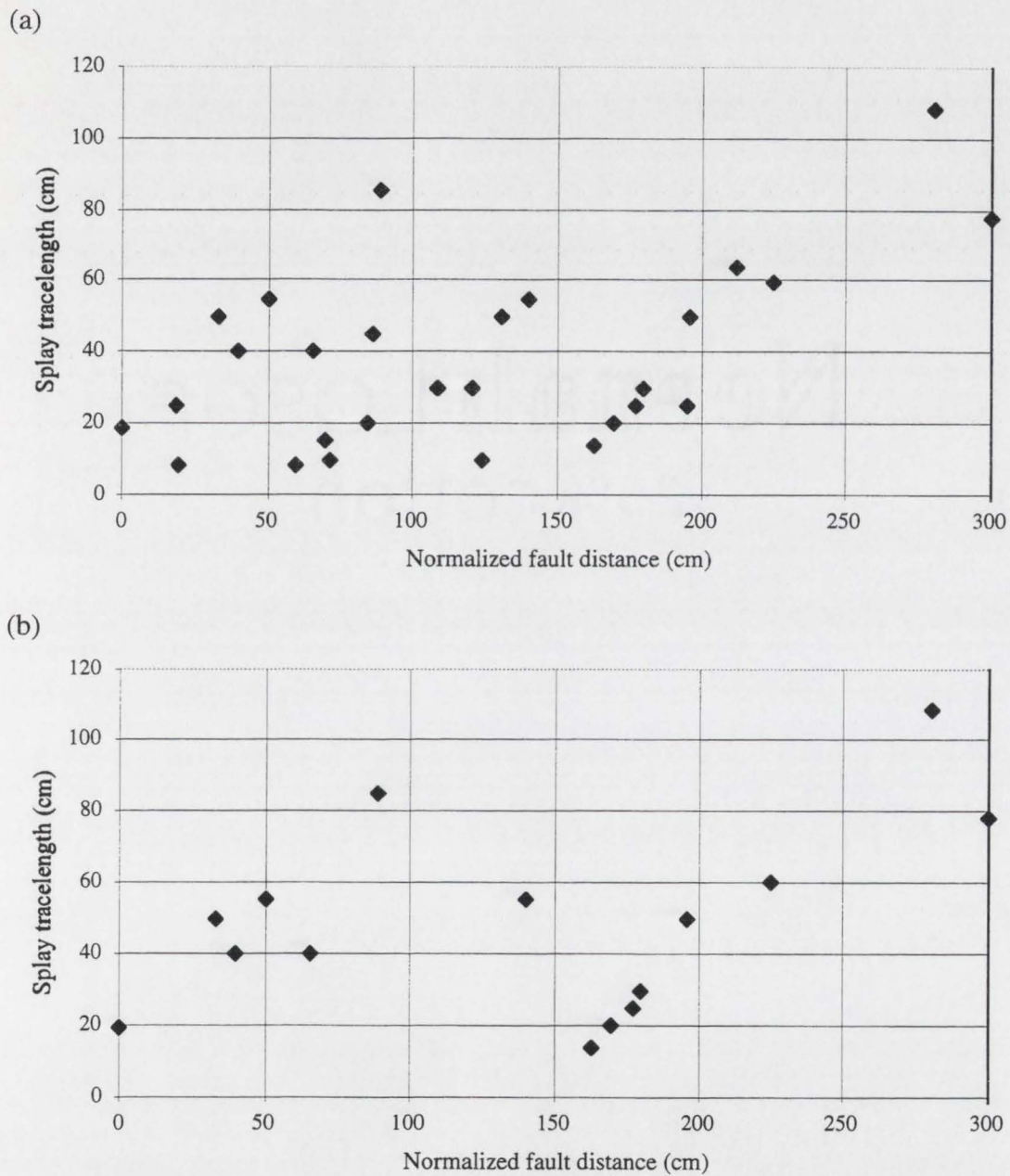


**Figure 17. Plots of splay length vs normalized fault distance along fault SF-1. (a) The plot shows most of the splay length do not exceeding 60 cm for the first 2.3 m of the fault before lengthening slightly at the end. (b) This plot contains only splay fractures that have contacts with fault trace and the result is similar to (a).**

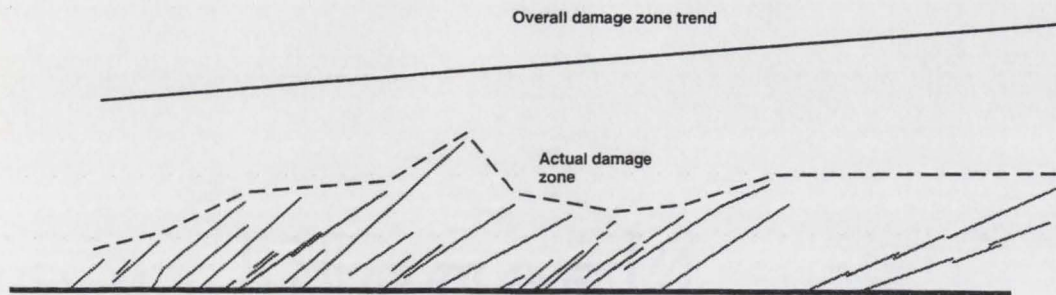


Figure 18. The extent of splay-fracture damage on the horizontal surface of fault SF-1. The straight line connecting the first splay fracture and the last splay fracture shows a widening splay-fracture damage zone. The dashed line marks the actual extent of the damage zone.

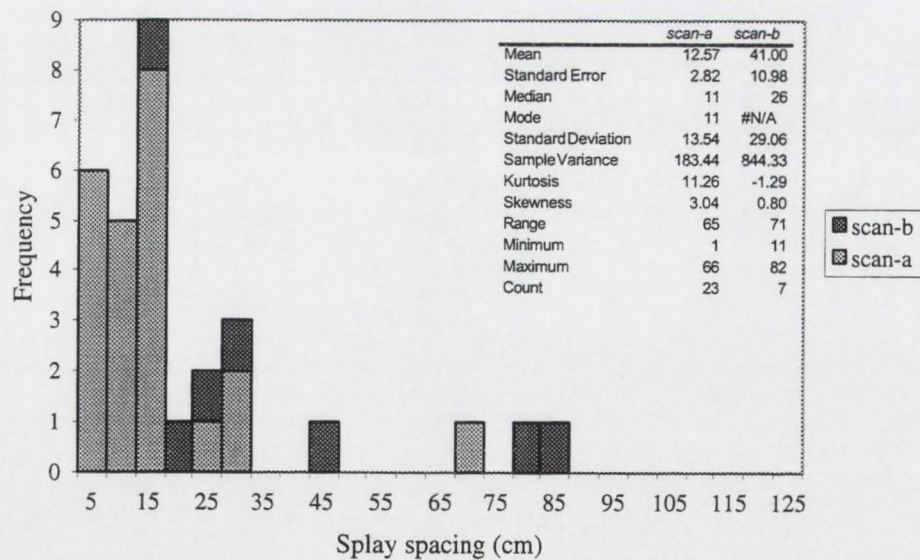
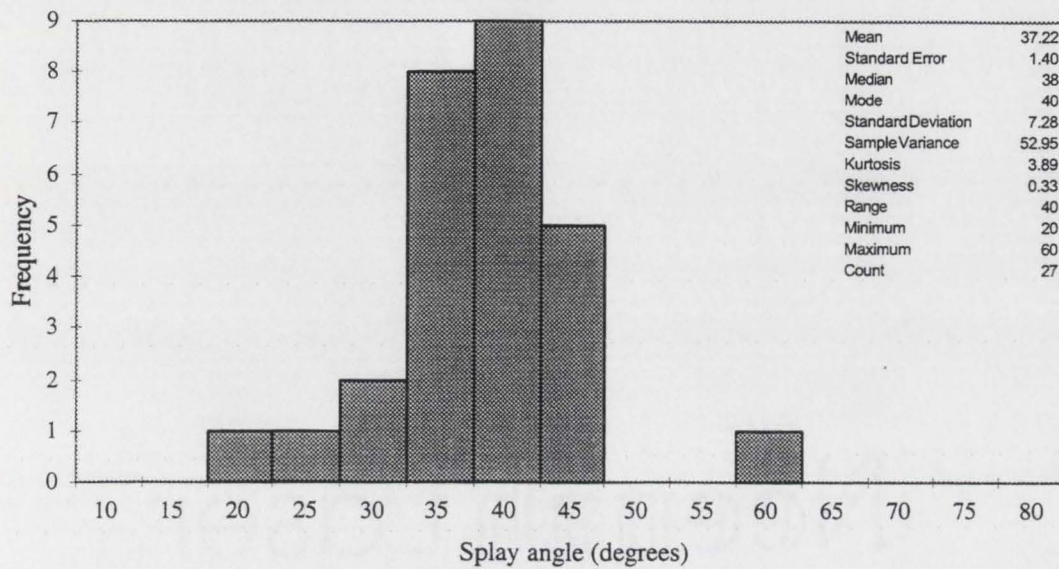
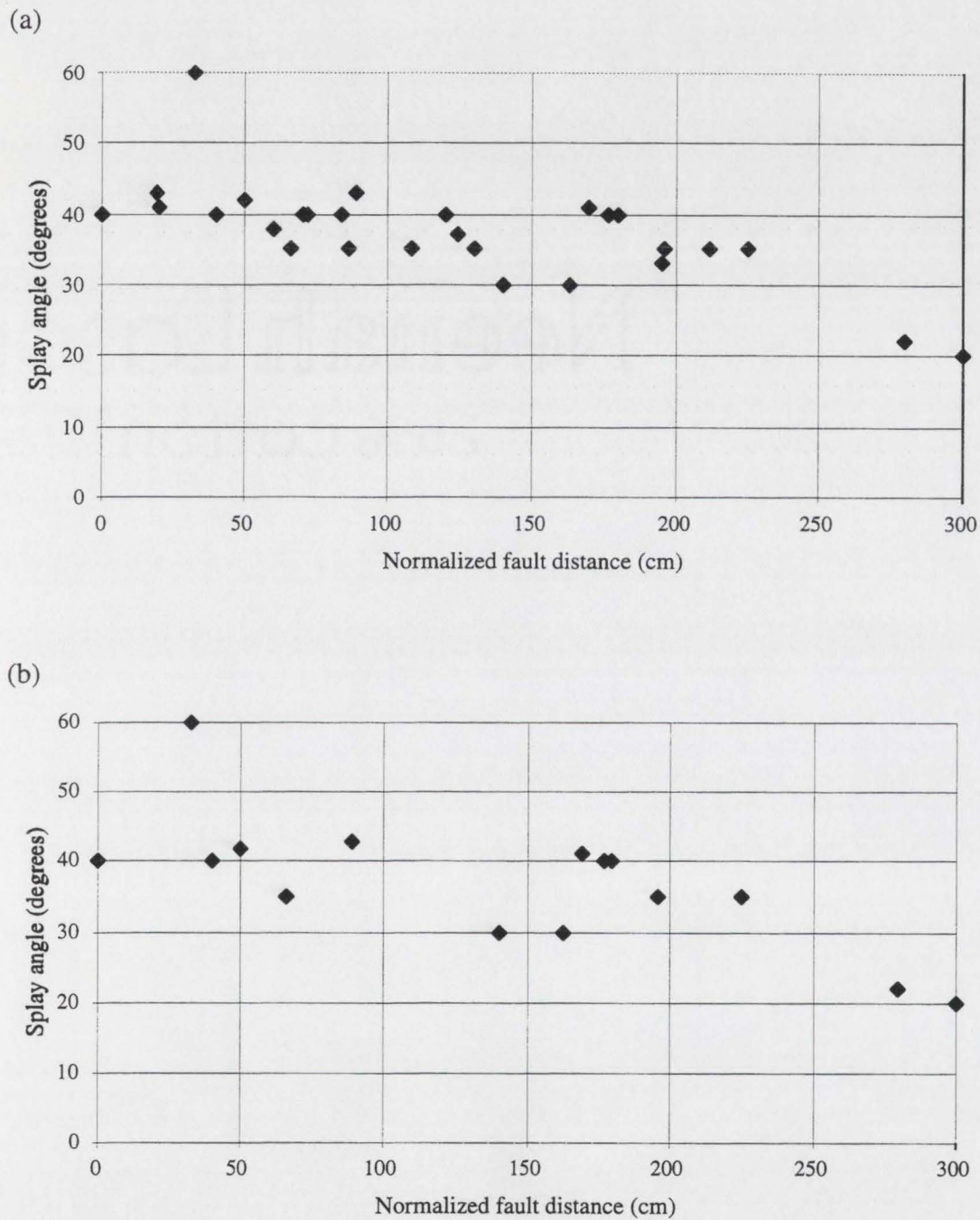


Figure 19. Histogram of fault SF-1 *scan-a* and *scan-b* splay-fracture spacing. The chart shows a high number of fractures in 5–15 cm spacing in *scan-a* distribution and varying spacing for *scan-b* distribution. The statistics of the distribution are given in the top right corner.



**Figure 20. Distribution of fault SF-1 horizontal surface splay angle. The chart shows dominant splay angle making up the single peak. The statistics of the distribution are given in the top right corner.**

trace (Fig. 20). Figure 21a shows the splay angle clustering around 30°–43° for the first 225 cm of normalized fault distance before dropping to 20°–22° beyond 225 cm. Not surprisingly, Figure 21b has similar result as Figure 21a even after those splay fractures that not in contact with the fault are censored. Both Figures 21a and 21b show a trend of decreasing splay angle as fault distance increases. Splay-fracture traces on the vertical surface plunge westerly and seem to form an acute angle counterclockwise from the plunging scan line and these vertical-wall splay-fracture traces coincide with the dip of splay-fracture surface. The mean dip of the splay fractures is 36° with a standard deviation of 9° (Fig. 22). Figures 23a and 23b show the elevation-view structure in three dimensions, with green ribbons representing fractures on the vertical surface and red ribbons representing fractures on the horizontal surface. It appears the splay-fracture surfaces are dipping in a northwesterly direction.



**Figure 21. Plots of splay angle vs normalized fault distance for fault SF-1. (a) The plot shows most of the splay angles are within the 30°–43° range for the first 2.3 m of the fault before dropping to a lower angle. (b) This plot contains only splay fractures that have contacts with fault trace and the result is similar to (a).**

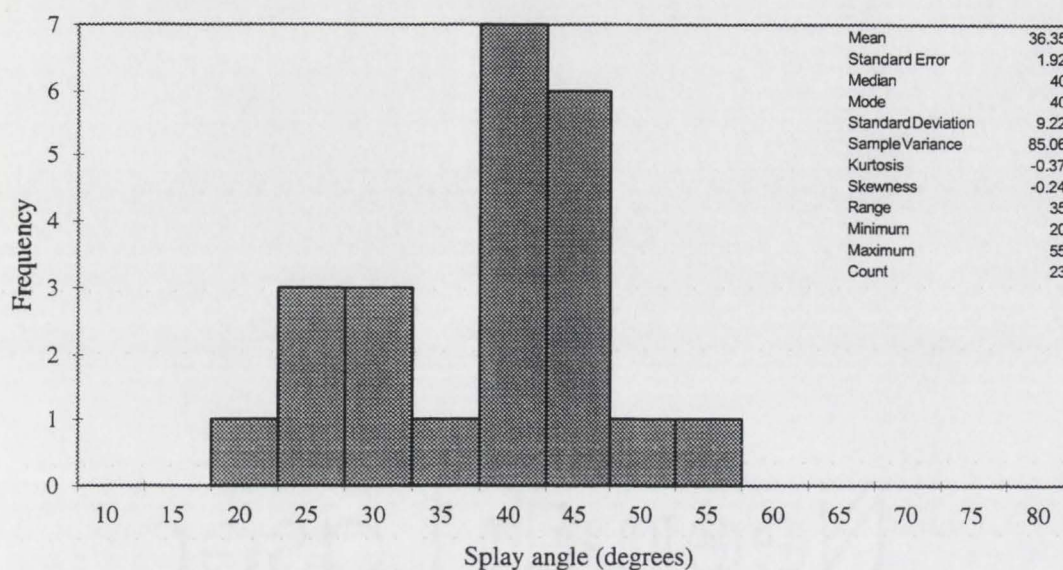


**Figure 22. Distribution of fault SF-1 vertical surface splay angle (splay plane dip). The chart shows a bimodal distribution of dips. The statistics of the distribution are given in the top right corner.**

#### Summary for Small Splay Structures

Fault SF-2 and other end-view structures are from isolated faults that do not link up with other faults. The splay cracks are mostly linear structures on both horizontal and vertical surfaces with little or no curvature and have epidote-chlorite mineralization. The compilation of all mapped splay-fracture attitudes and their associated fault attitudes yields dihedral angles of 20°–65° (Table 1).

Fault SF-1 is the only elevation-view structure seen in the field and it does not link with other structures. Splay-fracture traces on both horizontal and vertical surfaces are linear and are mostly mineralized by epidote and chlorite. The vertical-wall splay fracture provides a mean splay-fracture plane dip of  $36^\circ \pm 9^\circ$ . Both fault SF-1 and fault SF-2 have decreasing splay angles with increasing distance from fault center. Fault SF-2 has increasing splay tracelength with increasing distance from fault center. The horizontal surface splay-fracture traces reveal a widening damage zone from the middle portion of the fault to the fault end. Both SF-1 and SF-2

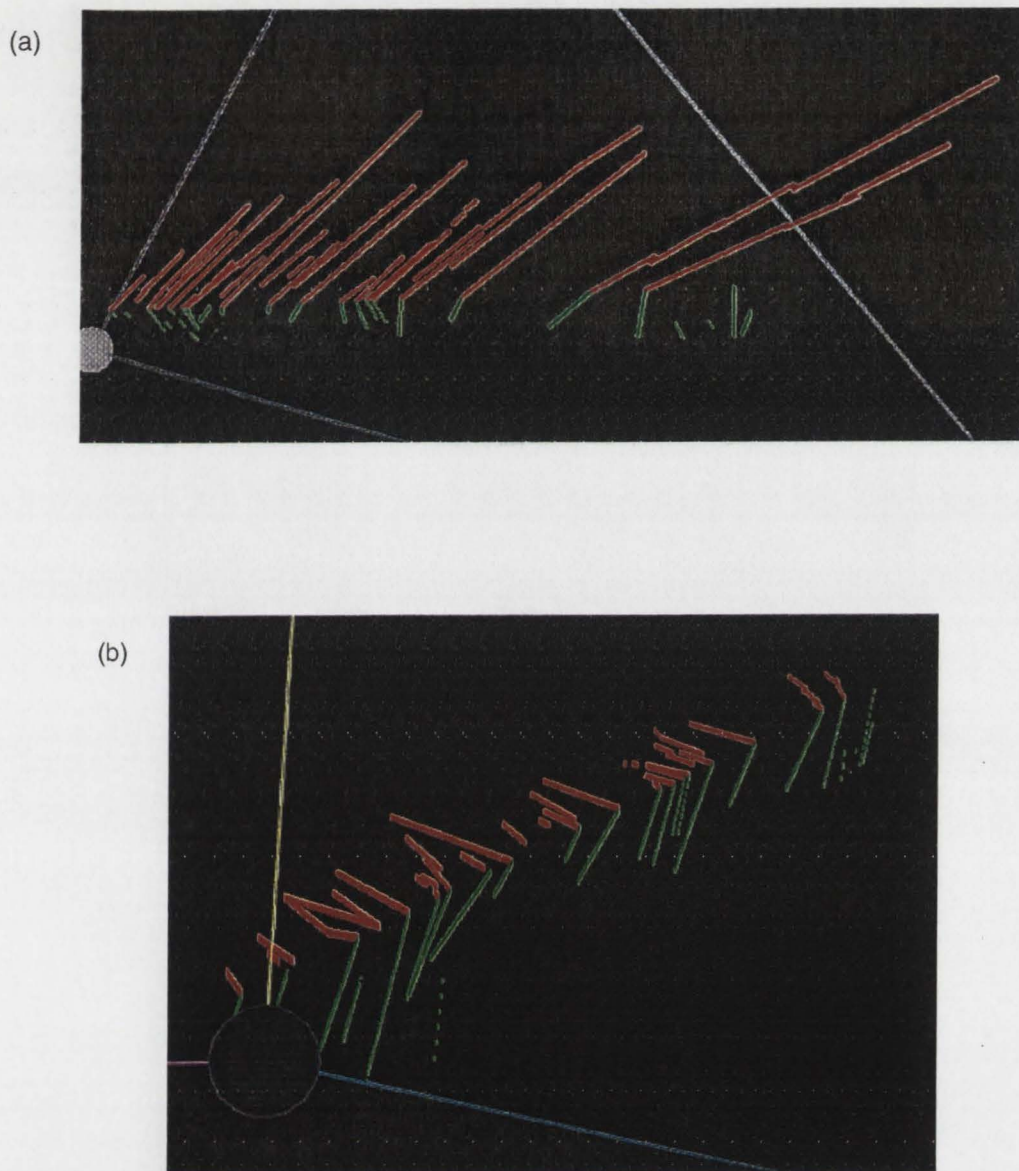


**Figure 23. Three-dimensional visualization of fault SF-1 elevation view splay structure. (a) Oblique view looking down from top left. (b) Oblique view looking up from bottom left.**

TABLE 1. THE DIHEDRAL ANGLES BETWEEN FAULT PLANES AND  
SPLAY-FRACTURE PLANES

Fault	Fault attitude	Splay attitude	Angle between two planes
Bear Creek fault group	074°/84°	203°/90°	51.2°
	075°/80°	205°/74°N	52.7°
	084°/80°	209°/81°N	61.5°
		204°/86°N	53.2°
		201°/81°N	55.9°
		210°/89°N	63.9°
			47.3°
			49.6°
			57.9°
			50.9°
			52.7°
			61.4°
			54.9°
			57.0°
		65.5°	
		44.5°	
		46.1°	
		54.8°	
KJ-4	057°/81°S	025°/74°S	32.0°
		026°/76°S	30.7°
SF-2	061°/81°S	206°/71°N	44.4°
		202°/64°N	51.6°
		213°/68°N	41.4°
KJ-1	065°/88°S	045°/86°S	20.1°
		048°/74°S	21.8°
		214°/86°N	31.5°
		211°/69°N	40.4°
		215°/85°N	30.8°

Note: The fault and splay attitudes are in right-hand rule notation.

displayed an increase in splay-fracture spacing and lower splay-fracture density with increasing distance away from the fault.

### **Small Faults, Fault Groups, and Fault Populations**

The small fault descriptions will be presented in the manner the faults were mapped: single faults will be discussed first; single faults with significant splay fractures within the fault groups (Kip Camp and Bear Creek fault groups); and general fault descriptions of the Reflecting Bowl faults and the Segall and Pollard (1983a) Kip Camp map.

The maps of single faults show examples of two end-members of secondary fractures: a heavily splay-fractured fault (KJ-4) and a right-laterally-linked fault with few splay fractures (BJ-B). The map of fault group KJ-5 shows an interconnecting fault step complex in the middle of two faults. The map of the Bear Creek fault group displays both dilatant and compressive secondary fractures on a single fault and on other faults in the area. The last fault group is the Kip Camp fault group, which has a few rhombochasms and also includes other faults in the area. In the fault populations, both the smaller areal Reflecting Bowl fault population and the larger areal Kip Camp fault population are described.

#### **Single Fault: KJ-4**

A fault in Kip Camp named KJ-4 has a trace length of about 17 m and an elevation difference of 4.88 m from west to east (Figs. 24 and 25). Fault KJ-4 is an almost textbook case of a single strike-slip fault with dilational ends as envisioned by Martel (1997), with the eastern end exhibiting more splays than the western end. A straight scan line with trend of  $065^\circ$  was set up along the fault and an attitude of  $057^\circ/81^\circ\text{W}$  was measured on the fault at its western end.



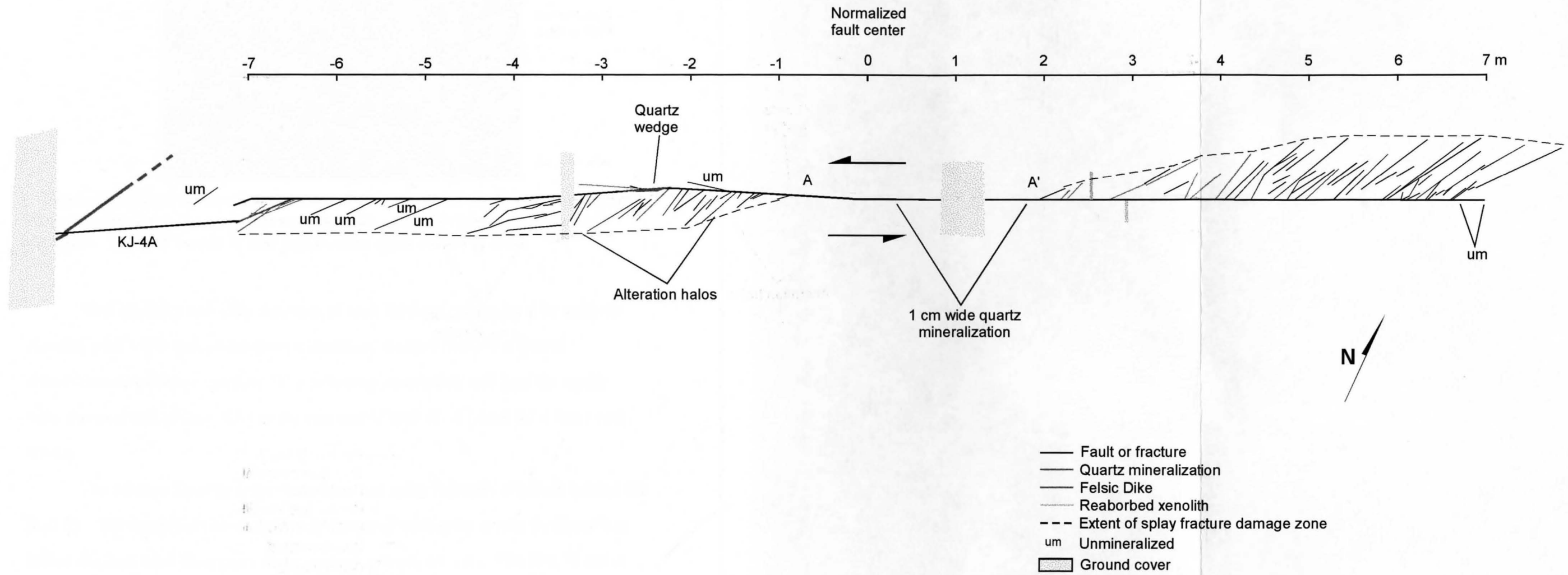
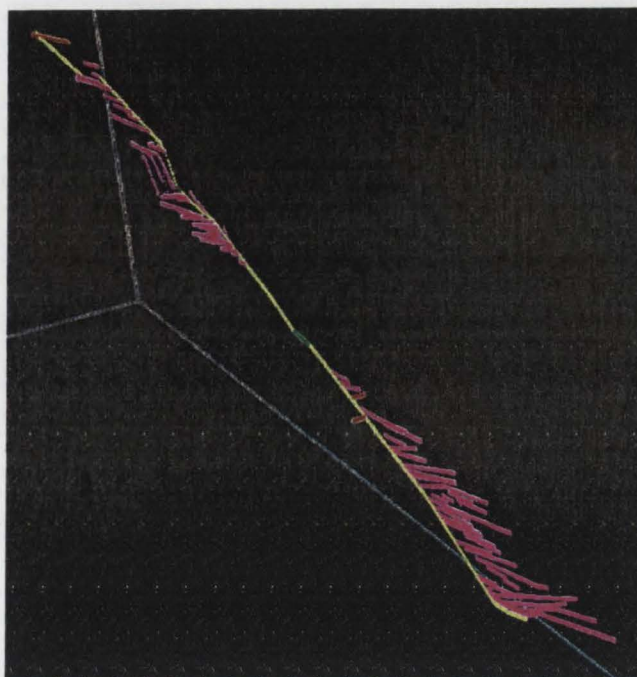


Figure 24. Map of fault KJ-4 showing fracture geometry, mineralization, and offsets. This fault exhibits numerous splay fractures and it offsets a reabsorbed xenolith. Quartz mineralized fractures and unmineralized fractures are in the minority of the splay fracture population. Fault KJ-4 is linked with fault KJ-4A through a series of splay fractures.



**Figure 25. Three-dimensional visualization of fault KJ-4. It has an oblique view looking down from top left and the fault gains elevation in the easterly direction. Top left corner is east and bottom right corner is west.**

Both the fault and splay fractures of fault KJ-4 are mineralized by epidote-chlorite, with a few exceptions (non-mineralized fractures), and the quartz mineralization pattern is random. The following description will lead the reader from the west end of fault KJ-4 to the east end of fault KJ-4 where KJ-4 links with KJ-4A.

The western fault tip is unmineralized and splay fractures originate behind the fault tip. The south fault block is heavily fractured with splay cracks for about 6 m before the fault trace disappears under ground cover to the east. The first 75 cm of the west fault end are in a north-south trending trough and two splay-fracture attitudes were obtained:  $025^{\circ}/74^{\circ}\text{S}$ ,  $026^{\circ}/76^{\circ}\text{S}$ . The dihedral angles between the two splay-fracture attitudes and the fault surface are  $32^{\circ}$  and  $31^{\circ}$ . West of the ground cover, there are four quartz mineralization cavities, several quartz-filled splay

fractures, and a reabsorbed xenolith is offset by 50 cm. One seemingly continuous 10-mm wide quartz cavity lens in the fault is interrupted by the ground cover and emerges from the other side of the ground cover for another 50 cm. In the mid-region of KJ-4, the base of a splay has a quartz wedge 3 cm wide by 8 cm long and, immediately next to it, a quartz lens 2 cm wide by 72 cm long. The mid-region of KJ-4 also displays splay fracturing on the north fault block, and a group of mid-region splay fractures displays a 1-cm wide zone of alteration halos. At the east end of fault KJ-4, a transfer structure forms behind the KJ-4 east-end tip and links up with the tip of KJ-4A. A vein in the transfer structure has abundant quartz. The eastern end of KJ-4 terminates at a splay crack at its tip. Fault KJ-4A offsets a 1-cm thick dike by 4 cm and continues east under bushes. A few unmineralized branch fractures are observed between the KJ-4 mid-region and its west end.

The overall splay-fracture traces of fault KJ-4 are linear and there are a few splay fractures on the south block that branched out and kinked. Fault-parallel fracture-spacing scanlines were placed 20 cm away from fault for *scan-a* and 50 cm away for *scan-b*. The splay-fracture spacing for the *scan-a* distribution (mean and standard deviation of  $13 \pm 9$  cm) shows most of the fractures have spacings in the 10 cm to 20 cm range, and the *scan-b* distribution (mean and standard deviation of  $26 \pm 16$  cm) has fewer fractures which are more widely dispersed (Fig. 26). There is an increase in the splay-fracture spacing (from a mean of 13 to 26 cm) and fewer splay fractures (from 41 to 18) in the *scan-b* distribution as compared with the *scan-a* splay-fracture spacing distribution (Fig. 26).

The splay tracelength of KJ-4 has a mean and standard deviation of  $39.8 \pm 26.7$  cm (Fig. 27). The splay tracelength varied from the fault center to the fault ends on Figure 28a as do Figure 28b. However, it appears both Figures 28a and 28b have a trend of increasing splay tracelength towards the fault ends. The north-block splay-

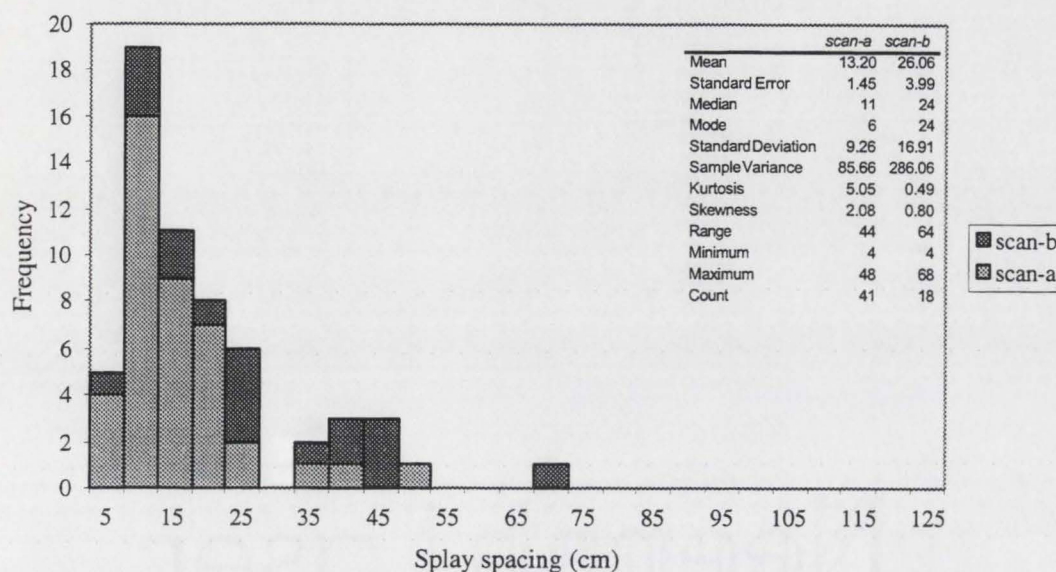


**Figure 26. Histogram of fault KJ-4 scan-a and scan-b splay-fracture spacing. High concentration of fractures with 10 – 20 cm spacing for the scan-a distribution and varying spacing for scan-b distribution. The statistics of the distribution are given in the top right corner.**

fracture damage zone does not exceed 40 cm orthogonal to the fault trace (Fig. 24). There are more splay fractures on the south fault block than the north fault block, and the south fault-block splay-fracture damage zone did not exceed 70 cm orthogonal to the fault trace (Fig. 24). The difference in the distance from the fault between the fault blocks should translate into a higher average splay-fracture tracelength for the south block than the north block (Table 2). This raises an interesting observation that as fault KJ-4 trace rises from west to east, could the asymmetry between the north and south blocks be the result of different stress conditions or mechanical properties at each fault ends. It should be noted that the splay-fracture damage zone near the center of the fault has a shorter perpendicular distance to the fault, and the splay-fracture damage zone distance perpendicular to the fault increases to its maximum before the end of fault and narrows at the end of fault (Figs. 24, 28a, and 28b).

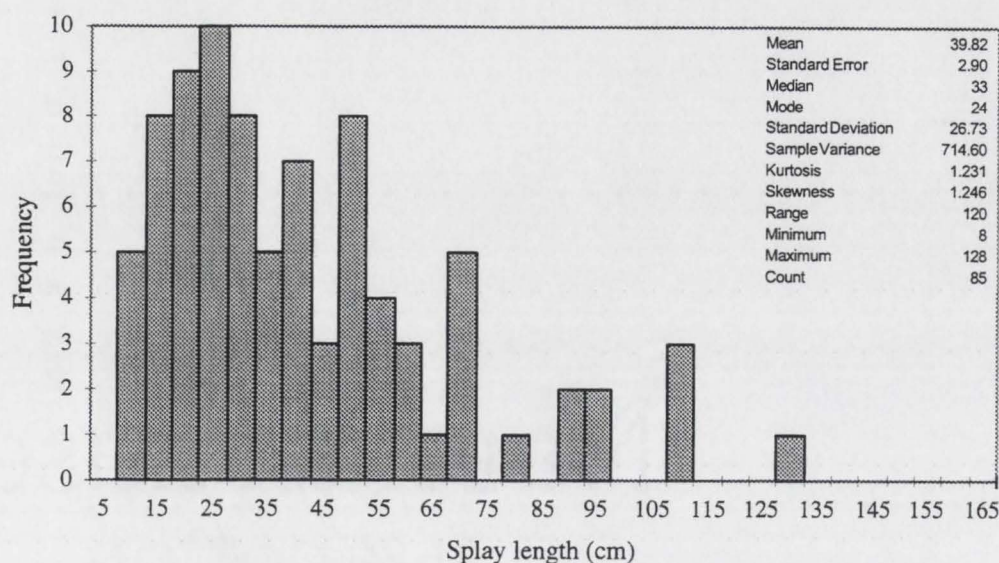


**Figure 27. Histogram of fault KJ-4 splay tracelength. The chart shows a bulk of "short" splay tracelength before the distribution tapers off for the longer tracelength. The statistics of the distribution are given in the top right corner.**

From the splay-angle histogram, the mean and standard deviation splay-fracture angle is  $39^\circ \pm 12^\circ$  counterclockwise from the fault trace (Fig. 29). In the scatter-plot of splay angle and normalized fault distance, one could argue that as the normalized fault distance increases towards its ends, the splay angle showed a decreasing trend from its peak near the middle of the fault (Figs. 30a and 30b). It appears the lowering of splay angle towards fault ends has kept the splay-fracture damage zone from widening even though the splay tracelength increases towards fault ends.

It is postulated that the area between A-A' (Fig. 24), which occupies only 19.9% of entire fault trace, could be the original penny. It is also hypothesized that (under the influence of CZT):

- 1) the current population of splay cracks was formed in a single event after the fault had grown to its present maximum length;
- 2) the fault has experienced multiple episodes of splay cracking, thus the

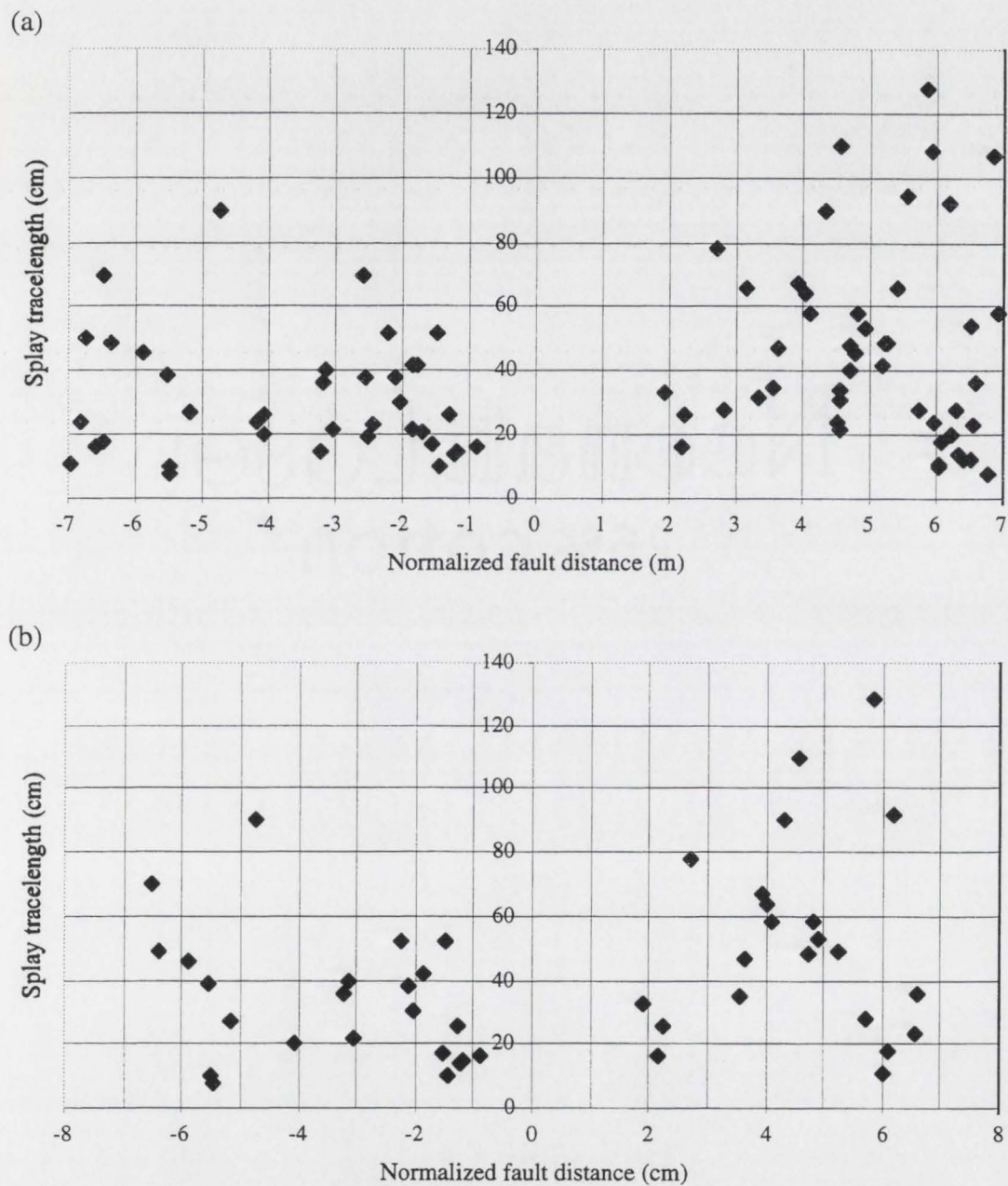


**Figure 28. Plots of splay tracelength vs normalized fault distance for fault KJ-4. (a) The plot shows a general lengthening of splay tracelength as the fault distances from the center. (b) This plot contains only splay fractures that have contacts with fault trace and the result is similar to (a).**

TABLE 2. STATISTICS OF FAULT KJ-4  
NORTH AND SOUTH BLOCK SPLAY  
TRACELONGTHS

Statistics	North block	South block
Mean	30.805	46.745
Standard Error	2.901	4.407
Median	24	40
Mode	16	58
Standard Deviation	18.574	30.211
Sample Variance	345.011	912.716
Kurtosis	1.449	0.211
Skewness	1.206	0.939
Range	82	120
Minimum	8	8
Maximum	90	128
Count	41	47

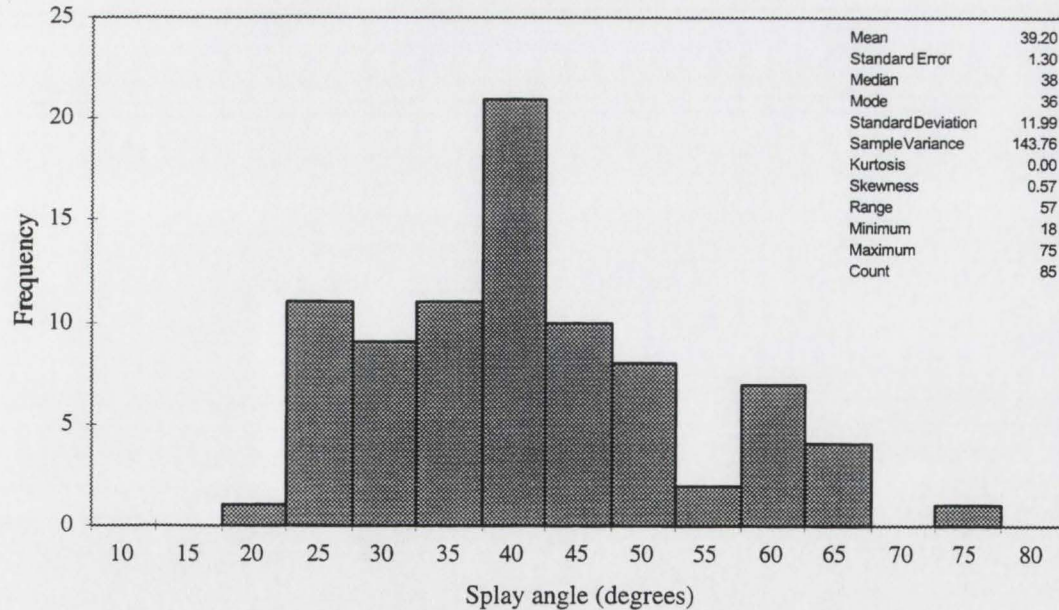
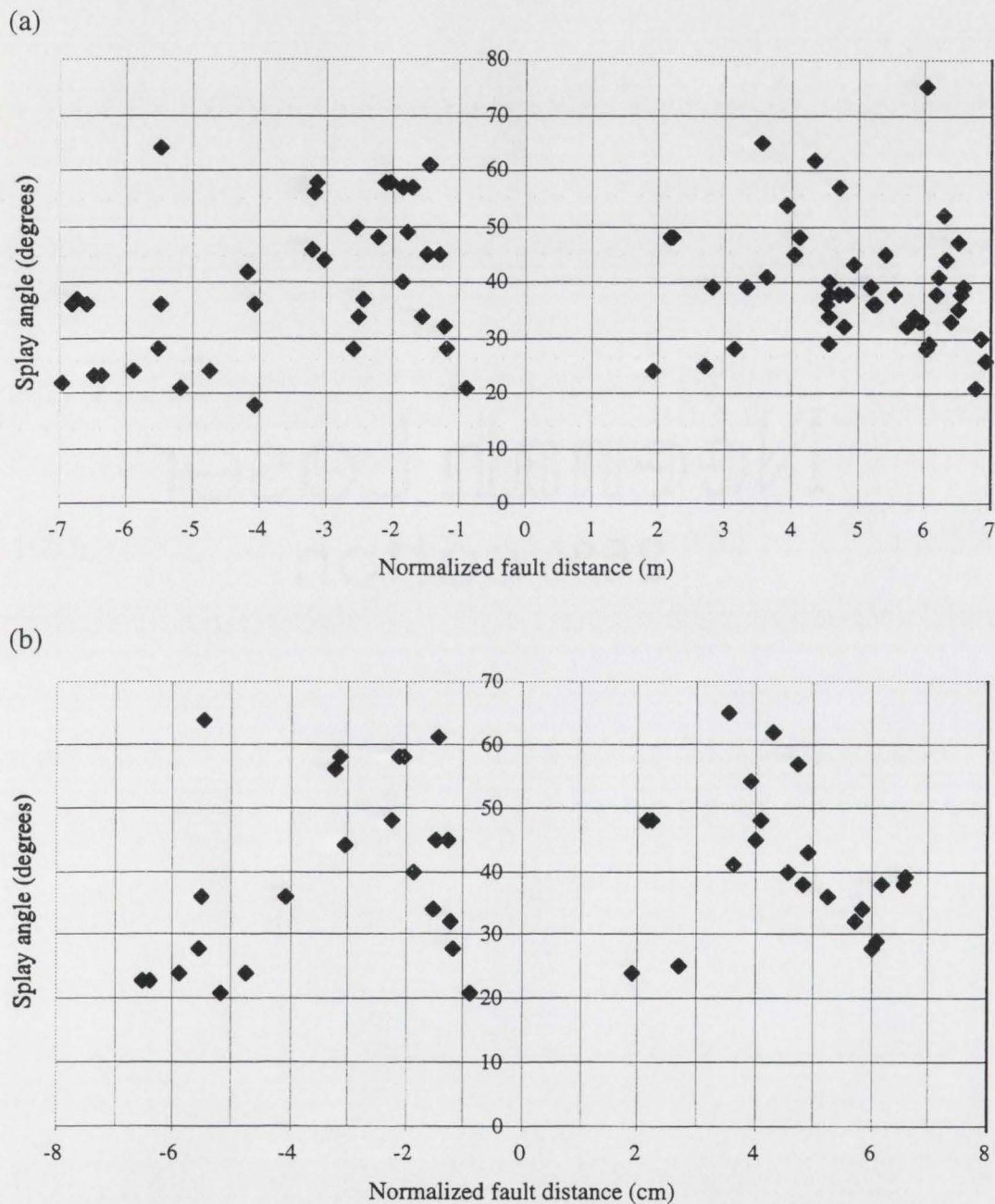


Figure 29. Distribution of fault KJ-4 splay angle. The chart shows a prominent spike of 40° for the angle between splay fracture trace and fault trace. The statistics of the distribution are given in the top right corner.



**Figure 30. Plots of splay angle vs normalized fault distance for fault KJ-4. (a) The plot shows an increasing splay angle as fault distances from the center and splay angle falls sharper near the fault ends. (b) This plot contains only splay fractures that have contacts with fault trace and the result is similar to (a).**



population of splay cracks represents the numerous cohesive zones which would have formed.

Coincidentally, the widest (10 mm) and most continuous (1.5 m) quartz-filled fracture lies within A-A'.

#### Single Fault: BJ-B

Near the Bear Creek fault group is a fault designated as BJ-B. It has a trace length of approximately 27 m and a height of 3.74 m (Fig. 31a). This fault, in contrast to KJ-4, has few splays and it is linked by several right-lateral steps. The right-lateral step is usually accompanied by foliated granodiorite to the right of the step (Fig. 32). In places, foliated granodiorite developed at both sides of a right-lateral step. While the left-lateral step has a distinct sharp angle, the right-lateral step is rounded, making angle measurement challenging. A scan line trending  $070^\circ$  was laid to assist mapping. With the scan line starting from the west end, the first 4.5 m of the fault is mineralized by 3- to 15-mm wide pinch-and-swell quartz mineralization followed by a large quartz wedge, Wedge A (10 cm wide, 140 cm long), and a quartz cavity (2 cm wide, 57 cm long). It appears that Wedge A widens from west to east and that the displacement motion offset Dike A by 1.55 m (Fig. 31b). The same displacement motion probably spawned a smaller quartz wedge, Wedge B (8.5 wide cm, 66 cm long), at the distance of 8.5 m from west end of the fault BJ-B (Fig. 31c). Regrettably, there is no offset marker to indicate its slip amount. At a distance of 1 m from west end of the fault BJ-B, there is a 50-cm long right-lateral step with a 20-cm right step, maintaining about the same  $070^\circ$  trend, and its mineralization is obscured by dark lichen cover. At Wedge A, the fault trace changes its trend to  $075^\circ$ . A stretch of foliated granodiorite is observed along the fault beyond wedge B before it disappears under cover zone A. A short interval of

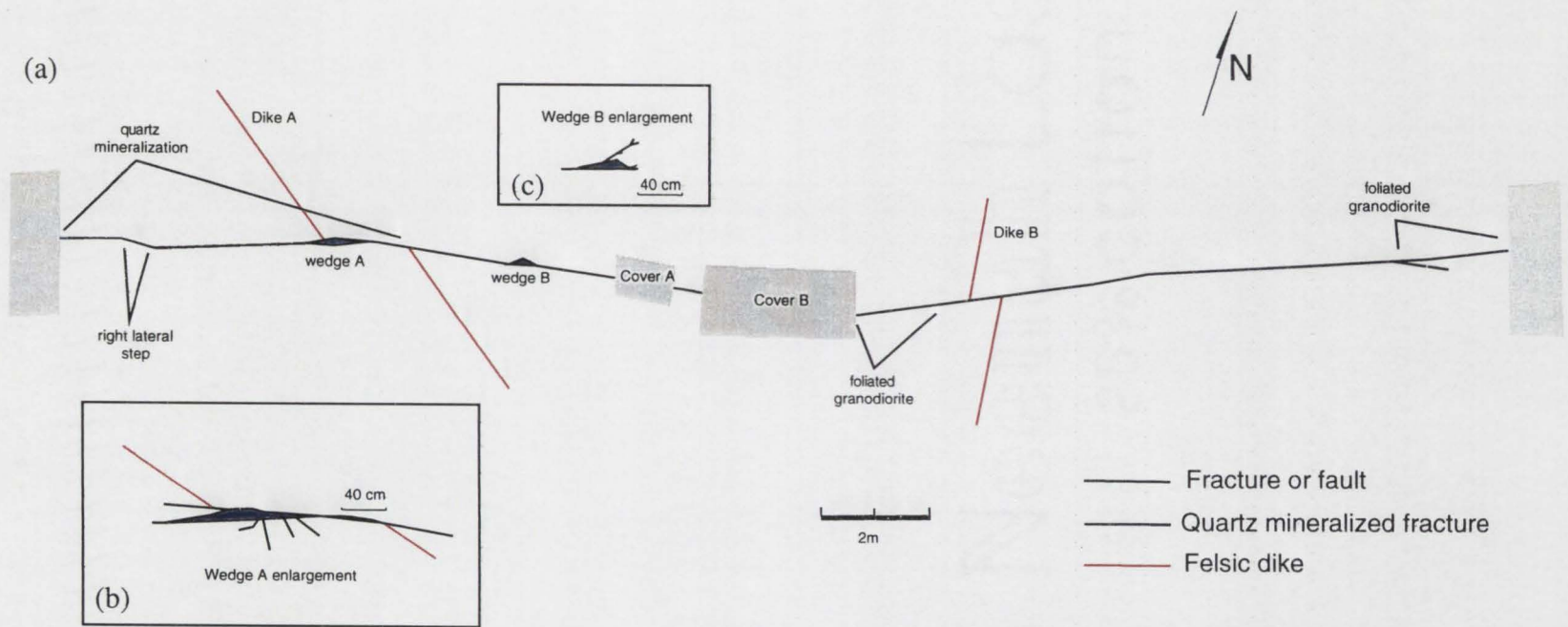


Figure 31. Map of fault BJ-B. Right-lateral steps and large quartz wedges are the prominent features of this fault.



**Figure 32. Photo of a right-lateral step within fault BJ-B with foliated granodiorite on its right side.**

fault BJ-B between cover zone A and cover zone B appears normal with neither foliated granodiorite nor quartz mineralization. The fault trace emerges from cover zone B and continues over a raised surface along a new trend of  $065^{\circ}$ . The fault trace encounters an 80-cm span of foliated granodiorite before it offsets Dike B by 60 cm. The trace continues east with little or no deformation and no visible quartz mineralization until it splits. From the split junction, foliated granodiorite is evident on the main fault until it enters ground cover.

Overall the BJ-B fault structure has few splay fractures and, based on the right-lateral steps, mineralized wedges, and the radical change in fault-trace orientation, it is possible that fault BJ-B consists of a minimum of five connected joints which did not connect by splay fractures.

Fault Group: KJ-5

The KJ-5 fault group consists of four closely spaced faults (KJ-5, KJ-5A, KJ-5B, and KJ-5C) offsetting a dike, and two of the faults have created a mineralized fault step complex (Fig. 33). These faults show the detailed relationship of

interacting or connecting faults where slip can be determined. The mapped structures are east of the Kip Camp fault population area and they have an overall elevation difference of 4.4 m. A scan line, trending  $070^\circ$ , was set up along KJ-5 for only 9 m to confine the mapping area. Fault KJ-5 has an attitude of  $080^\circ/77^\circ\text{S}$  with slickenlines raking  $22^\circ\text{E}$ , and its trace runs along the scan line from west to east and from lower to higher elevation. It has offset the dike by 31.25 cm with a net slip of 35 cm and has no visible evidence of quartz mineralization. A quartz-filled unnamed fracture with an attitude of  $060^\circ/74^\circ\text{S}$  intersects the middle part of KJ-5. To the south of KJ-5, KJ-5A appears briefly from beneath the ground cover. Fault KJ-5A does not seem to displace the dike and is untouched by quartz mineralization. It connects with KJ-5B to the south of KJ-5A through several steps. The few connecting steps between KJ-5A and KJ-5B are mineralized by quartz or are epidote-chlorite filled. The KJ-5B trace below the dike, in elevation, is altered by quartz mineralization and is almost parallel to the scan line. From the dike, which KJ-5B offsets by 5 cm, the KJ-5B trace changes trend to  $060^\circ$  for 3.57 m before it becomes parallel to the scan line again. In the same stretch, KJ-5B shows a pattern of epidote-chlorite mineralization that diminishes to none and then some hints of quartz mineralization before the trace ends with three branch fractures that link KJ-5 and KJ-5B. The interesting feature of this fault group is the fault step complex between KJ-5 and KJ-5B. The north side of fault KJ-5B, in a zone from the dike to the easternmost strand of the fault step complex, is dominated by a series of epidote-chlorite filled fractures that have these features:

- 1) a generalized spacing interval of 1–2 cm between each other,
- 2) no connections with KJ-5 and KJ-5B,
- 3) splay angles of  $35^\circ$ – $45^\circ$  counterclockwise to the fault trace, and
- 4) short splay lengths (10–25 cm).

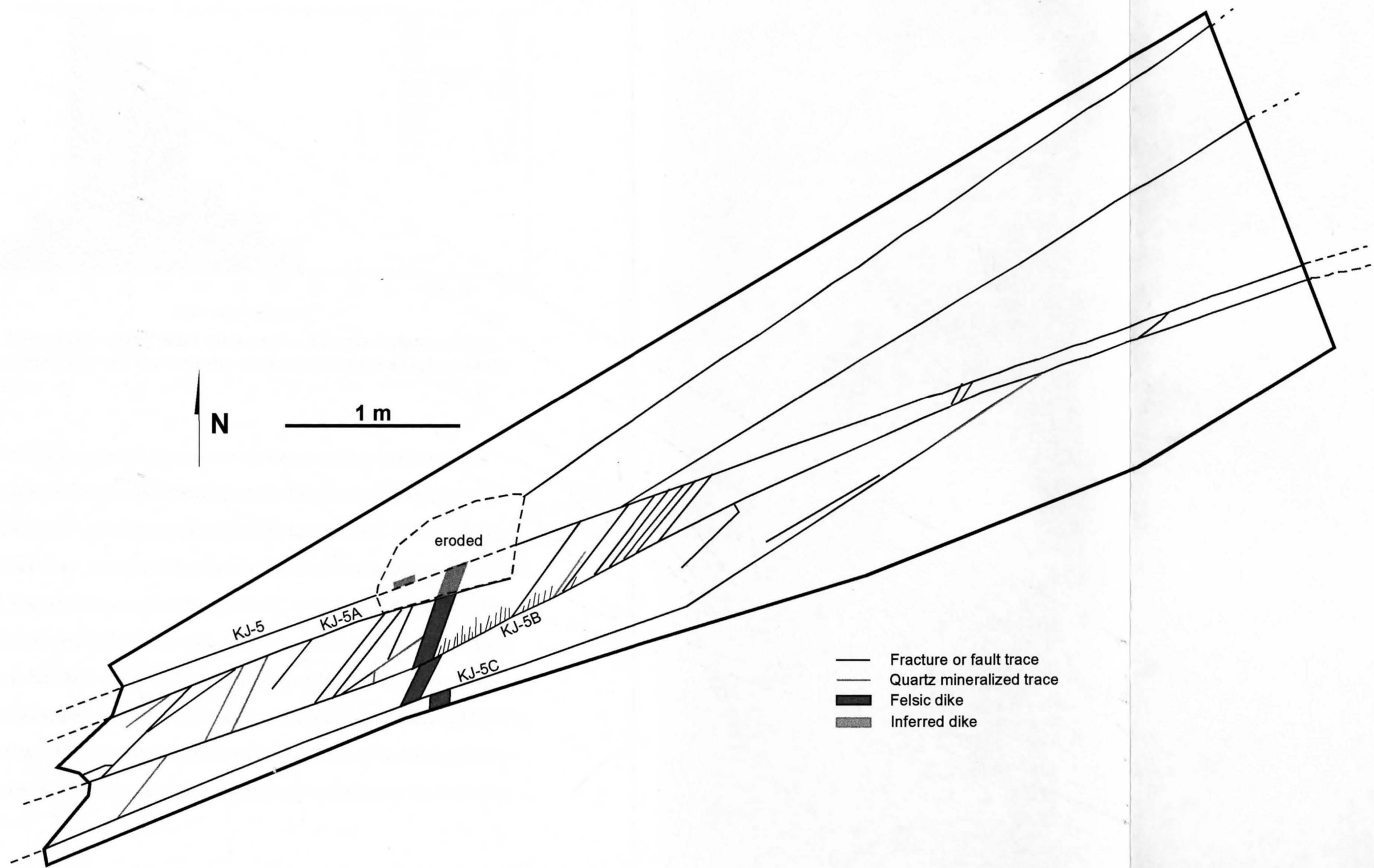
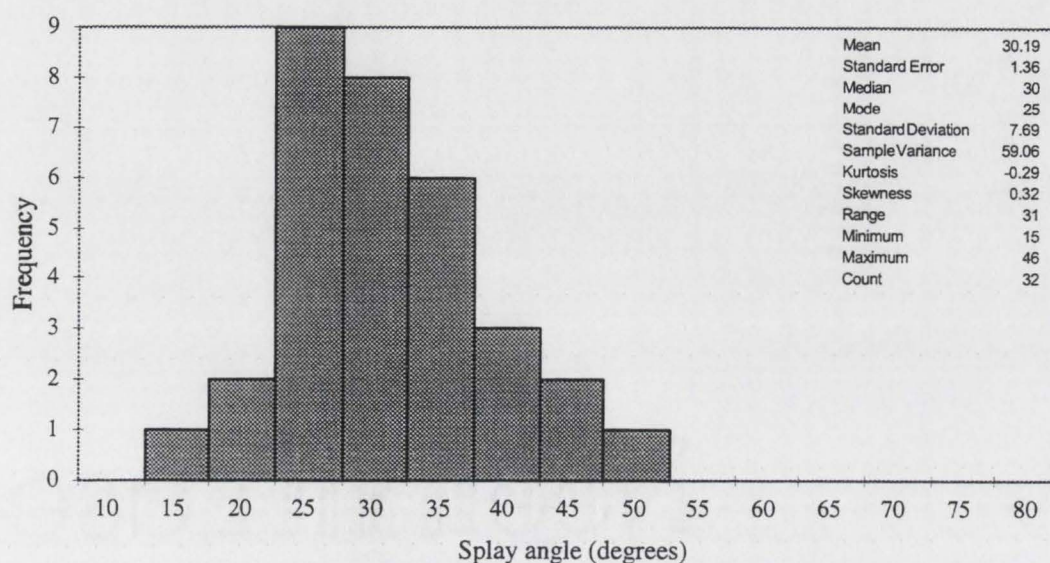


Figure 33. Map of fault KJ-5 showing interconnecting fractures between faults.



**Figure 34. Histogram of fault KJ-5 splay angle. The chart shows a tight range of dominant angle and the statistics of the distribution are given in the top right corner.**

In the fault step complex, there are seven longer epidote-chlorite-filled connecting steps with a short nonconnecting quartz-filled vein with splay angles ranging from  $24^{\circ}$  to  $30^{\circ}$  and without consistent spacing intervals. All the angles of the splay fractures were plotted and they have a mean and standard deviation of  $30^{\circ} \pm 7^{\circ}$  (Fig. 34). The southernmost fault trace, KJ-5C, is almost parallel to the scan line and it offset the dike by 17.5 cm with a net slip of 22.5 cm before it kinks left and terminates at KJ-5B. Fault KJ-5C has an attitude of  $071^{\circ}/77^{\circ}\text{S}$  with a slickenline rake of  $7^{\circ}\text{E}$  while running parallel to the scan line, and a similar attitude ( $072^{\circ}/78^{\circ}\text{S}$ , slickenlines raking  $10^{\circ}\text{E}$ ) was obtained before it kinks. Prior to the kink, epidote-chlorite dominates KJ-5C, whereas quartz mineralization dominates the fault after the kink.

#### Kip Camp Fault Groups

The Kip Camp fault groups are located at the northeast corner of Segall and

Pollard's (1983a) Kip Camp map. The previously mapped faults were mapped at a smaller scale (1:100) and were comprised of three fault groups (KJ-1, KJ-2, and KJ-3), with KJ-1 being the southernmost group and KJ-3 the northernmost group (Fig. 35). These faults encounter a single continuous dike with variable offset and there are a few rhombochasms among the faults, providing more outcomes that a model or fracture mechanics would have to account for.

The mapped faults emerge from the larger kinked faults shown on the Kip Camp map of Segall and Pollard (1983a) and trend  $060^\circ$ . The topography rises by 9.77 m progressively to the east and there are three dikes in the area. This area is dominated by brittle fractures with no sign of right-lateral steps. Most of the fractures in the area have some degree of quartz mineralization and certain fractures have been heavily weathered, making it hard to detect some of the mineralization in the fractures. However, the fractures near or at the fault kink have a greater presence of quartz mineralization and this has been attributed to the local widening of the faults and joints between the granodiorite slabs for kink strain accommodation (Segall and Pollard, 1983a; Davies and Pollard, 1986). The origin of the KJ-1 group and the other fault groups' fractures' origin are uncertain as they could either be the result of fault shearing on preexisting joints or fault kinking as it buckled, or combined actions. Davies and Pollard (1986) believed the short, filled cracks along the outer arcs of the folded layer opened dilatantly to accommodate strain. The known splay fracture and outer arc fracture angles were both compiled and they have a mean and standard deviation of  $37^\circ \pm 12^\circ$  (Fig. 36). Segall and Pollard (1983a) and Davies and Pollard (1986) suggested that kinking was essentially contemporaneous with slip on the small faults and that the right-lateral deformation accommodated by the kink band was compatible with left-lateral slips on small faults.

Of the three dikes in the area, Dike A, trending  $336^\circ$  with an attitude of

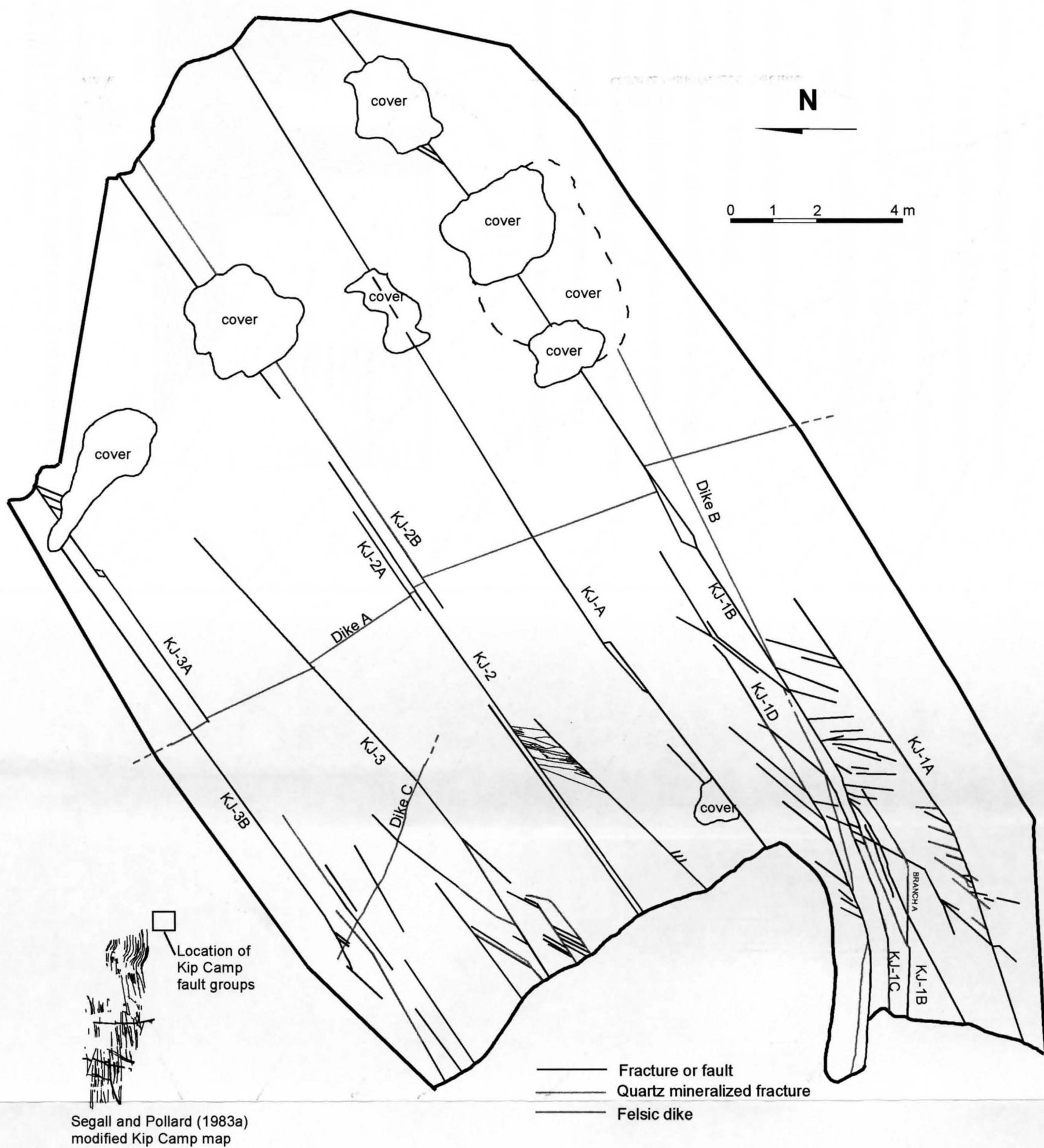


**Figure 35. Map of Kip Camp fault groups. Located at the most northeastern corner of Segall and Pollard (1983a) Kip Camp map, the detailed map of Kip Camp fault group shows kink band cracks, faults and its secondary fractures, rhombochasms, left-laterally offset dikes, and several fault step complexes.**



350°/68° E, is cut and offset by all the faults. Dike B trends in a more northeasterly direction and is visibly offset 1.25 m by KJ-1D only. Dike B is not offset by KJ-1C and fades out between KJ-1B and KJ-1C. The projected Dike B trend and path seem to line up with Dike B where it reappears on the south side of KJ-1B. Dike C is a smaller dike with a similar trend as Dike B and it has no visible offset when it crosses the KJ-3 group.

The entire area of faults will be individually described starting from the southernmost KJ-1A and ending with KJ-3B in the north.

The KJ-1 group is the only one with an exposed fault kink in the mapped area, whereas the rest of the fault groups had their west ends beneath ground cover. Quartz mineralization cavities appear intermittently along fault KJ-1A and the splay-like fractures in the inside arc of KJ-1A have both quartz and chlorite-epidote mineralization. Fault KJ-1B and its branch A show abundant quartz mineralization

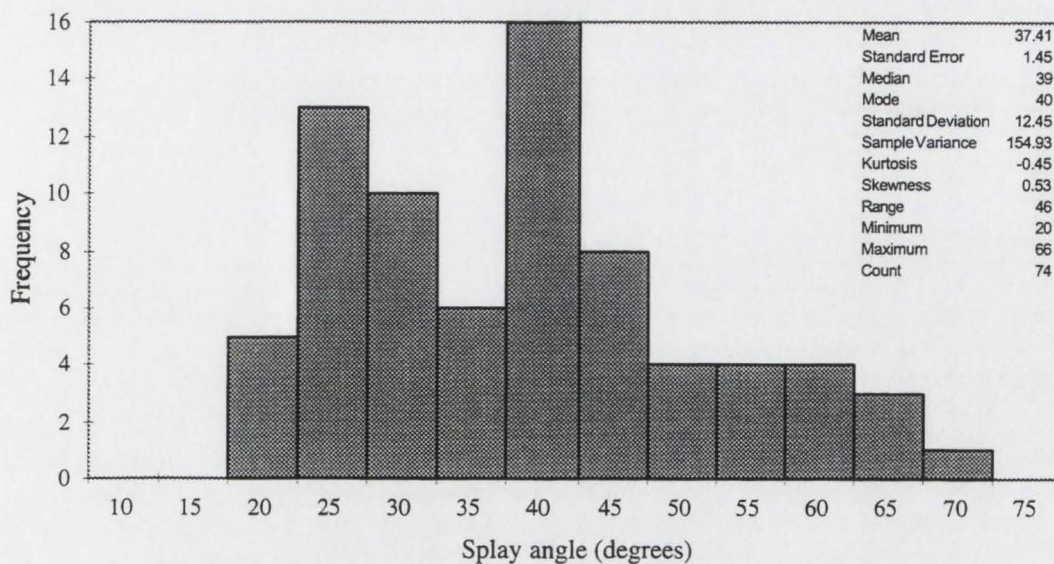


**Figure 36. Distribution of Kip Camp splay angles. The chart shows a wide range of splay angles with two prominent splay angle peaks. The statistics of the distribution are given in the top right corner.**

along the arc of the kink, as did KJ-1C. Fault KJ-1B has complex connections with several small subparallel fractures, and there are epidote-chlorite-filled south-dipping splay-like fractures ( $011^{\circ}/90^{\circ}$ ,  $003^{\circ}/80^{\circ}$ S,  $346^{\circ}/76^{\circ}$ S) on its outer arc. In the middle portion of KJ-1B, there are short north-dipping fractures ( $214^{\circ}/86^{\circ}$ N,  $215^{\circ}/85^{\circ}$ N,  $211^{\circ}/69^{\circ}$ N) just west of a shallow rhombochasm and Dike A is offset 60 cm with a net slip of 65 cm. Faint epidote-chlorite traces surround the rhombochasm. The trace of fault KJ-1B continues eastward before it is lost under ground cover. After the KJ-1B trace is lost, it has an end view exposure along which a fault attitude of  $065^{\circ}/88^{\circ}$ S with a slickenline rake of  $20^{\circ}$ E was taken. Along with the fault attitude, two splay-fracture attitudes on the northeast quadrant of KJ-1B were taken:  $048^{\circ}/74^{\circ}$ S and  $045^{\circ}/86^{\circ}$ S. The dihedral angles between the splay fractures and the fault plane worked out to be  $20^{\circ}$  and  $22^{\circ}$ .

Fault KJ-1C has an inside arc splay-like fracture that offsets Dike B right-laterally by 2 cm, and the fault itself crosses Dike B without any apparent offset and terminates into KJ-1D. An attitude of  $095^{\circ}/84^{\circ}$ S with a slickenline rake of  $8^{\circ}$ E was obtained along the arc of KJ-1D, which offsets Dike B by 1.25 m. Fault KJ-1D has a number of inside arc splay-like fractures and terminates at a point without additional fractures. However, KJ-1D might continue further east after a 25-cm hiatus and then terminate again in a similar fashion before briefly encountering a branch fracture from KJ-1B. The trace of fault KJ-A extends from ground cover to ground cover. Fault KJ-A is a rather nondescriptive fault with an attitude of  $059^{\circ}/87^{\circ}$ S taken just west of a weathered rhombochasm, and KJ-A offsets Dike A by 1 cm. Beside the weathered rhombochasm, weathering and exposure have also incised the trace of fault KJ-A.

Fault KJ-2 is flanked by two unnamed fractures on its west end and by fault KJ-2A and KJ-2B on its east end. The majority of the traces for fault group KJ-2

have experienced some degree of weathering, making it difficult to determine mineralization. Fault KJ-2 has a highly fractured fault step complex near its western-end (Fig. 35). All the fractures in the fault step complex are largely mineralized with chlorite-epidote and occasional quartz mineralization. The unnamed fracture on the north flank appears to line up with the trace of fault KJ-2B, and fault KJ-2B offsets Dike B by 5 cm. Fault KJ-2 offsets Dike B by 10 cm with 10.3 cm of net slip, and its trace terminates but seems to continue along a fracture trace to its east that has an attitude of  $068^{\circ}/82^{\circ}\text{S}$  with a slickenline rake of  $0^{\circ}$ . The trace of fault KJ-2A begins as a point and is lost under ground cover in the east. It offsets Dike B by 12 cm with 12 cm of net slip and has an attitude of  $060^{\circ}/78^{\circ}\text{S}$  with a slickenline rake of  $25^{\circ}\text{E}$ . In places along the trace that are uneroded, fault KJ-2A has quartz mineralization up to 6 mm wide within its fault aperture.

Fault KJ-3 emerges from ground cover on the west end with a few accompanying unnamed fractures that have both splay-like and branch fractures. It has an attitude of  $062^{\circ}/73^{\circ}\text{S}$  and it offsets Dike B by 10 cm with 10.5 cm of net slip, but there is no discernable offset of Dike C. There are several weathered fracture traces between KJ-3 and KJ-3B and they show no visible offset of Dike C either. Fault KJ-3A offsets Dike B by 5 cm and it has a chlorite-epidote filled rhomb-shaped fault-step that is unweathered. The trace of fault KJ-3A shows additional splay fractures on the southwest quadrant of KJ-3A before it is lost under ground cover. The trace of neighboring fault KJ-3B offsets Dike B by 10 cm and the trace is short.

#### Bear Creek Fault Group

The Bear Creek fault group is divided into 10 individual faults or fault subgroups (Fig. 37). The Bear Creek fault group was mapped earlier by Bürgmann and Pollard (1994) as location BA90 to understand the strain accommodation of

discontinuous strike-slip faults under brittle-to-ductile conditions. It was found that in order to accommodate slip transfer across contractional steps, rock was squeezed vertically out of the step by ductile flow and that the mechanism responsible for such accommodation was not diffuse mass transfer but the crystal-plastic flow of quartz enhanced by increased stress. Bürgmann and Pollard (1994) also observed in that localities closer to the Mono Creek Granite, fewer fractures exist and well-developed ductile fabrics formed at fault terminations. This site is 1.5 km west of the Mono Creek Granite. The observations were inferred to be the direct consequences of increased maximum shear stress at higher temperatures. The side-by-side occurrence of brittle and ductile structures was caused by the pressure-weakening effect under conditions close to the brittle-ductile transition (Bürgmann and Pollard, 1994).

The Bear Creek fault group (BJ area) encompasses a larger area, with relief data, than location BA90. Additional detailed sketches of small fracture were made and mineralization patterns were mapped. The east-west trending fracture traces have slip that averages from a few centimeters to more than a meter measured on the offsets of a NW-trending dike and a mafic xenolith. Dilatant splay fractures in the area have orientations of  $50^\circ \pm 7^\circ$  counterclockwise to the fault trace and the mean and standard deviation are dominated by the epidote-chlorite-filled extensional fractures (Fig. 38). Splay-fracture tracelengths did not reveal any observable trends (Fig. 39). Fault-parallel fracture spacing scanline *scan-a* was placed 10 cm away from the fault and *scan-b* was placed at the bisector of two fault traces. Figure 40 reveals a high concentration of fractures with 5–20 cm spacing and a mean and standard deviation of  $24.57 \pm 22.89$  cm for the *scan-a* distribution. The *scan-b* distribution for fracture spacing is more dispersed, with a slightly elevated mean and standard deviation of  $27.53 \pm 27.13$  cm (Fig. 40). There is a decrease in the number of fractures from 61 to 28 as the distance increases from fault (Fig. 40). The fault

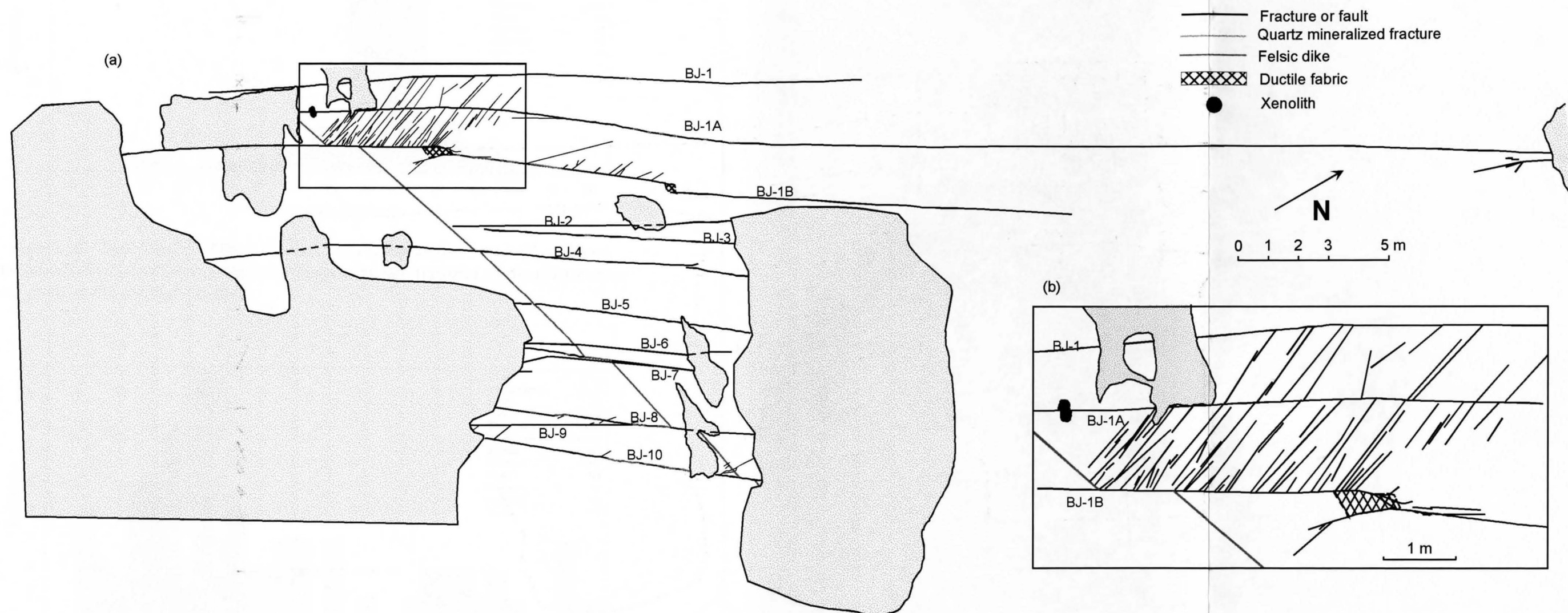
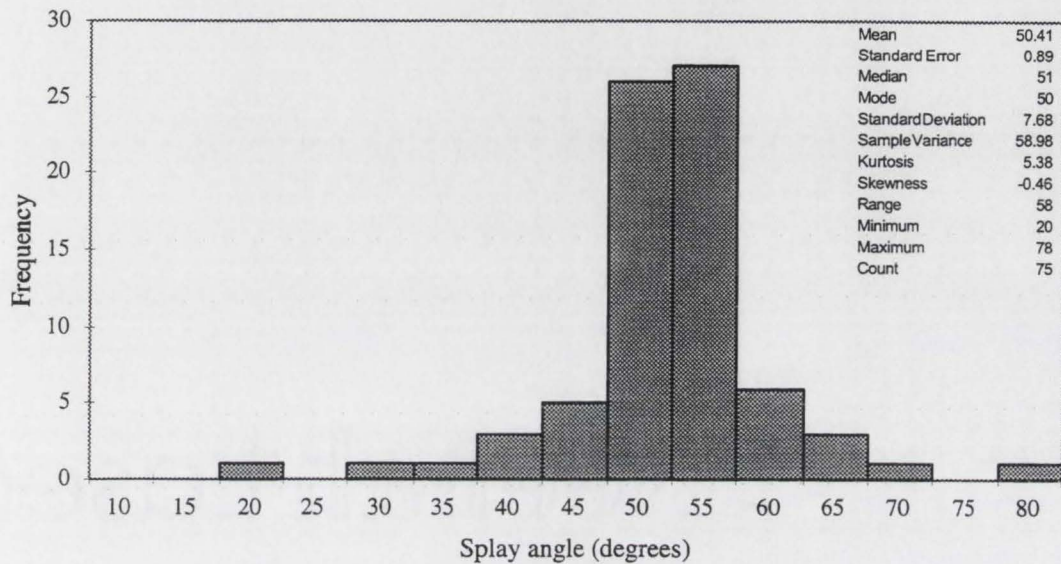
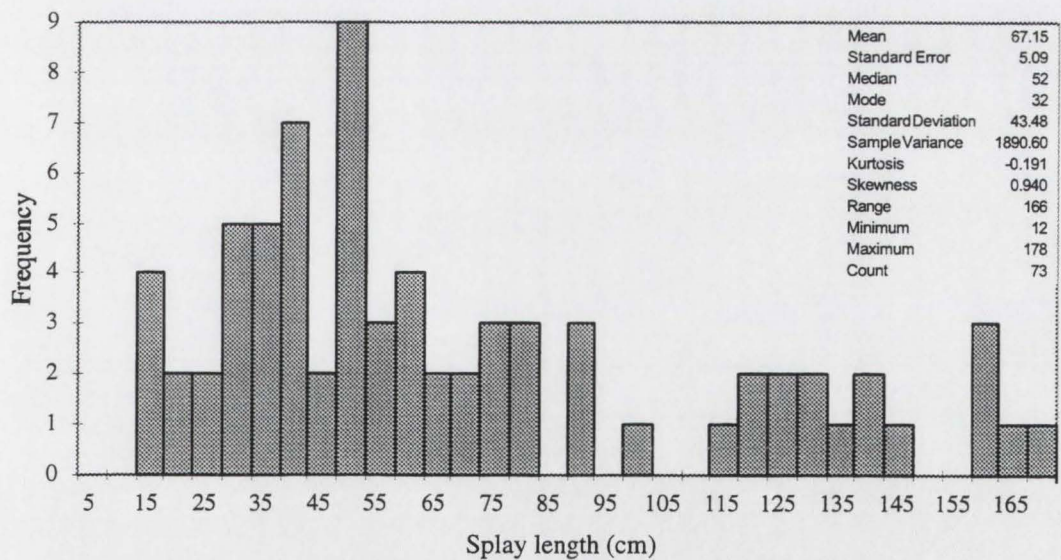


Figure 37. Bear Creek Camp fault group map. (a) Map of Bear Creek Camp fault group showing left-lateral offsets on some of the faults as indicated by a displaced dike and other fractures. (b) Detailed map of fault step complex and its associated right-lateral step. The matted region is the extent of foliated granodiorite.



**Figure 38. Distribution of Bear Creek Camp splay angles. The chart shows the domination of 50-55 degrees splay angles and the statistics of the distribution are given in the top right corner.**



**Figure 39. Histogram of Bear Creek Camp fault step complex splay tracelengths. It shows varying tracelength throughout the complex with a high concentration splay fractures in the range of 30-60 cm. The statistics of the distribution are given in the top right corner.**

step complex dominates all the reported data, as the rest of the faults in the area have very few splay fractures.

The side-by-side appearance of brittle and ductile structures, such as the prominent fault step complex and its associated contractional step, is the only example seen in this study. The rock outside the contractional step shows no significant ductile strain (Fig. 37b). The well-developed ductile fabric is restricted to the contractional steps along the faults and also in the faults in the southern part of the map, where they display mylonitic fault veins. Bürgmann and Pollard (1994) reported S-foliation orientation changes from 25°–35° near the fault to 40°–50° to the fault in the center of the fault stepover, with C-planes orientations up to 15° to the fault.

Fault BJ-1 has distinct terminations without any additional fractures. It has no offset indicators and has a linear and planar trace. Fault BJ-1 has several quartz

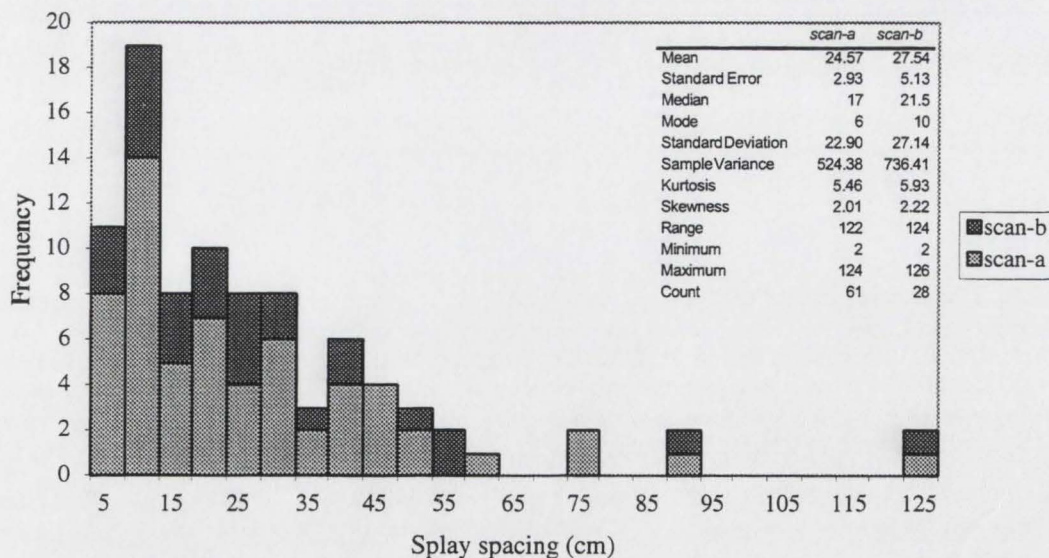


**Figure 40. Histogram of Bear Creek Camp fault step complex *scan-a* and *scan-b* splay fracture spacing. There is a high concentration of fractures with 5 – 30 cm spacing for the *scan-a* distribution and varying spacing for *scan-b* distribution. The statistics of the distributions are given in the top right corner.**

cavities along its trace and several splay fractures connecting it with BJ-1A. Fault BJ-1A has a continuous trace that emerges from beneath ground cover and loses its trace under ground cover. Fault BJ-1A is interrupted by a 4-cm left stepping of the trace followed by a 2-cm right-lateral step. Prior to the broken trace, BJ-1A has attitudes of  $074^{\circ}/84^{\circ}\text{S}$  and  $075^{\circ}/80^{\circ}\text{S}$ , and it offsets a xenolith by 3 cm. A number of quartz cavities with maximum dimensions up to 0.7 cm by 15 cm begin to appear along BJ-1A, and the trace has an attitude of  $256^{\circ}/83^{\circ}\text{N}$  after it resumes from the break. The trace of fault BJ-1B emerges from beneath ground cover and terminates at a point. It has an attitude of  $084^{\circ}/80^{\circ}\text{S}$  and it offsets a dike by 1.04 m with a net slip of 1.08 m. Fault BJ-1B has an intense area of splay fracturing on its northeast quadrant, and its trace experiences two right-lateral steps (22 cm and 40 cm) with several quartz cavities (maximum dimensions up to 1.4 cm by 80 cm). The splay fracturing between BJ-1A and BJ-1B occurs at a higher frequency than the splay fracturing between BJ-1 and BJ-1A, and the splays do not appear to continue from BJ-1B to BJ-1. Several splay fractures make contact with BJ-1A, and the dihedral angles have values from  $44^{\circ}$  to  $57^{\circ}$ .

Fracture BJ-2 and fault BJ-3 have no offset indicators and no secondary fractures but BJ-3 has a few quartz cavities (8 cm by 0.5 cm, 6 cm by 0.5 cm). Fault BJ-4 offsets the dike by 22 cm and it has a 5-cm right-lateral contractional step. Fault BJ-5 offsets the dike by 15 cm, whereas BJ-6 only offsets the dike by 3.5 cm. Fault BJ-7 offsets the dike by 81 cm and it has abundant quartz present in its trace. Fault BJ-8 has similar quartz present and it offsets the dike by 1 m. Fracture BJ-9 is rather free of quartz and it has no shear indicator. Fault BJ-10 has abundant quartz present and it offsets the dike by 59 cm. It has an attitude of  $086^{\circ}/86^{\circ}\text{S}$  and its accompanying splays have attitudes of  $048^{\circ}/78^{\circ}\text{S}$  and  $042^{\circ}/77^{\circ}\text{S}$  and appear to have sheared the dike by 0.5 cm each. The mapped faults and fractures from BJ-2 to BJ-



10 do not have expressive topographic steps and they are currently of little aid in individual fault modeling.

### **Fault Populations**

The Kip Camp (Fig. 41) and Reflecting Bowl (Fig. 42) outcrops were mapped to estimate the relationships between joint and fault lengths and fault sizes and their degree of mineralization, and populations of joints and faults. Fractures in these outcrops did not provide many examples of dilatant splay fracturing; however, the fault populations provide data on starting fracture trace lengths and locations, necessary for three-dimensional modeling of the development of faults from pre-existing fractures. This opportunity to examine what the true fracture and fault sizes are arises from a comparison of the Segall and Pollard (1983a) two-dimensional Kip Camp map with my two-and-half dimensions contoured map of Kip Camp. Kip Camp has a much larger mapped surface area outcrop (10800 m<sup>2</sup>) than Reflecting Bowl (1386 m<sup>2</sup>). Due to the smaller map resolution used in Kip Camp, it may have not captured as many of the smaller fractures as Reflecting Bowl. Both sites are about 1.2 km from the Mono Creek Granite.

A power-law distribution is expressed with the form of  $l^{-n}$ , where  $l$  is the fracture length and  $n$  is a real number, and it has been shown to provide a reasonable fit for a relationship of fracture frequency versus fracture length (Segall and Pollard, 1983b). Segall and Pollard (1983b) found the length frequency of joints in granitic rock follow a power-law distribution with a reported  $n$  value of 1.2 to 1.8 and the reported  $n$  value is used in this work as a benchmark for comparison. It is interesting to determine whether the fault distribution agrees with a power-law distribution and the implications of such a determination.

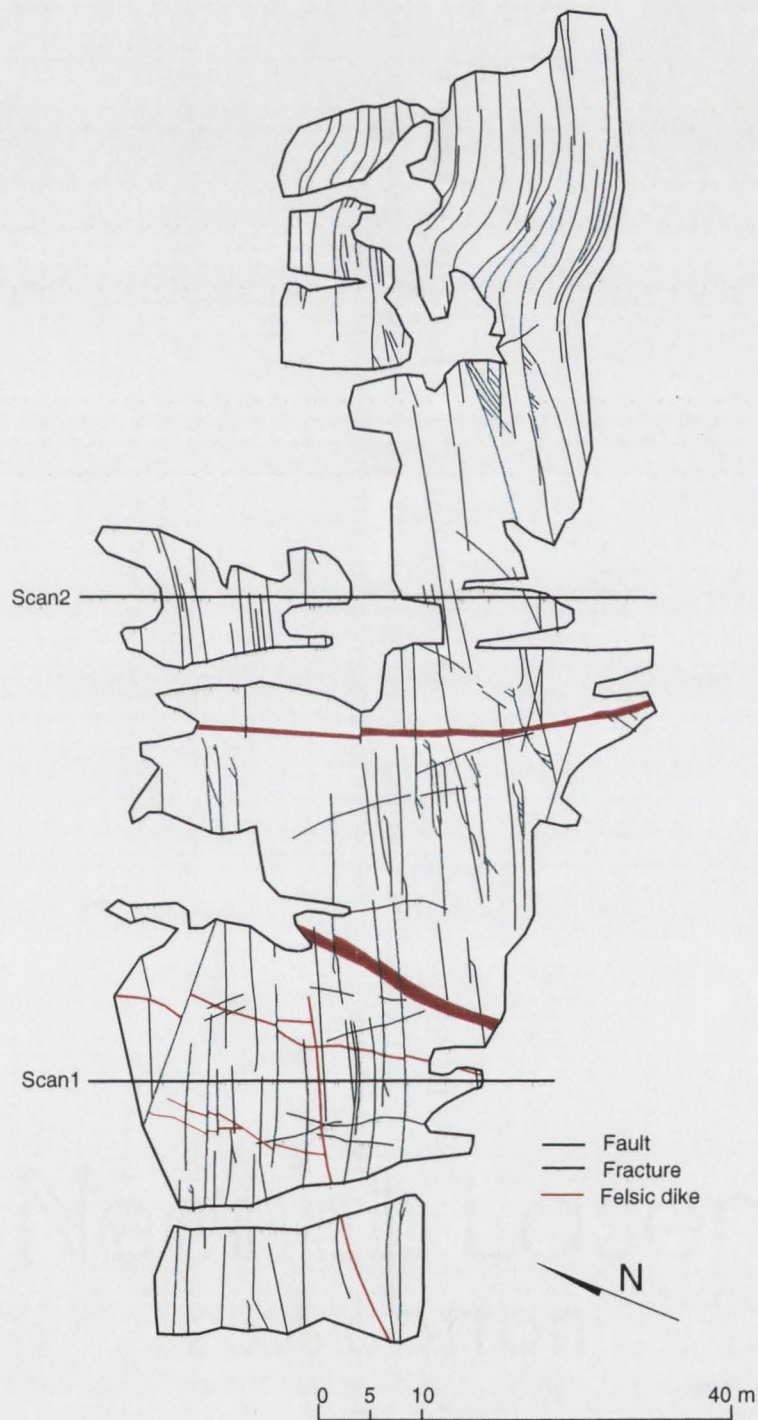
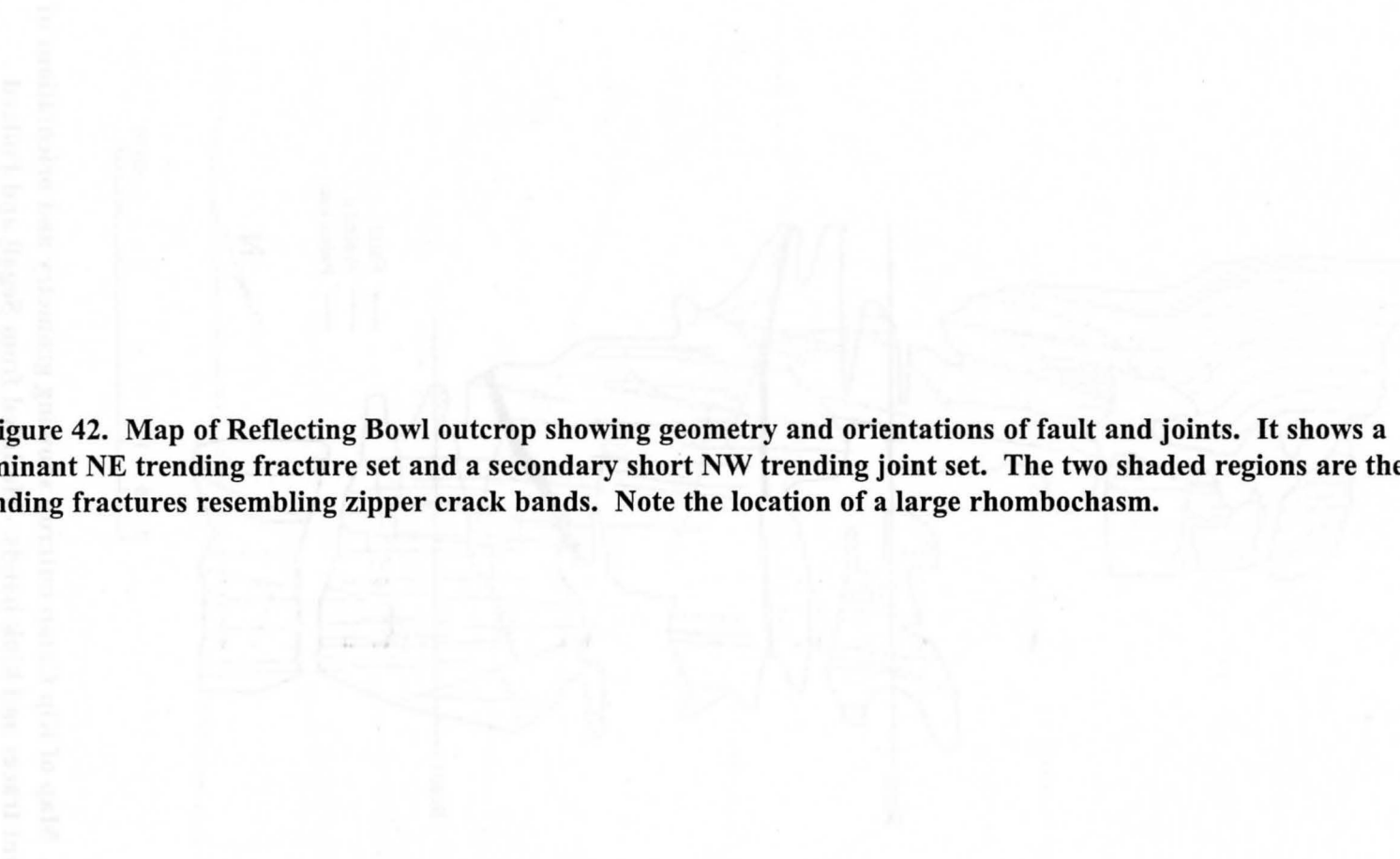
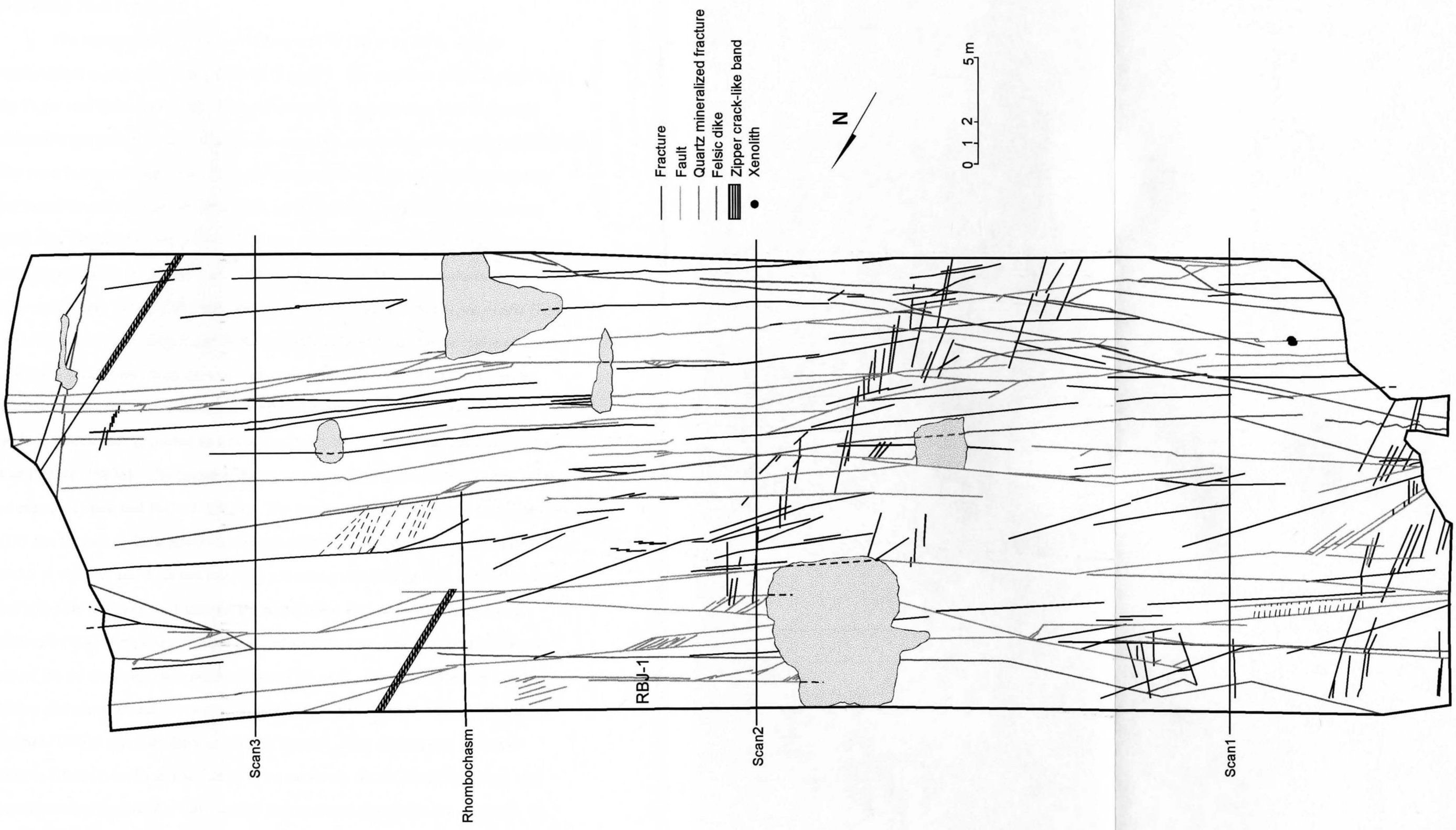


Figure 41. Map of Kip Camp outcrop showing geometry and orientations of fault and joint traces and kink bands. Modified from Segall and Pollard (1983a).



**Figure 42. Map of Reflecting Bowl outcrop showing geometry and orientations of fault and joints. It shows a dominant NE trending fracture set and a secondary short NW trending joint set. The two shaded regions are the NW trending fractures resembling zipper crack bands. Note the location of a large rhombochasm.**



### Kip Camp Fault Population

The topographic survey covered an area of 135 m by 80 m with an approximate topographic relief of 21 m (Fig. 41). The map was originally published by Segall and Pollard (1983a). With the evolution in computing power through hardware and software advances, greater demands are placed on the understanding of fractures in three dimensions. With the topographic survey, the original map was enhanced in order to provide better outcrop data for three-dimensional modeling (Fig. 43). Segall and Pollard's (1983a) Kip Camp fractures are subparallel fractures striking uniformly N50°–70°E and steeply dipping. Individual fractures range from 0.1 mm to 1 cm in width and they were filled with epidote, chlorite, or quartz (Segall and Pollard, 1983a). Segall and Pollard (1983a) observed that joint width (1 mm or less) was usually less than the width of the reactivated joint (less than 1 mm to greater than 1 cm). Some fractures exhibited zones of altered granodiorite 3 to 4 cm wide in which they appeared as lighter bands on either side of the fractures (Segall and Pollard, 1983a). The length of fractures range from a few meters to several tens of meters (Segall and Pollard, 1983a). The tracelength distribution of fault segment does not fit well under a power-law distribution ( $l^{-0.357}$ ), with a poor correlation factor  $r^2 = 0.145$  and does not have any promising trends (Fig. 44). Note that the  $n$  value for the fault segment tracelength distribution is at odds with Segall and Pollard's (1983b) reported  $n$  value for joint distribution. The longest fault segment out of the 40 fault segment traces measured 32.14 m. Most fractures are nearly planar and some broadly curved or kinked (Segall and Pollard, 1983a). Segall and Pollard (1983a) reported there is variable spacing, from centimeters to several meters, between faults at Kip Camp. Two randomly drawn scanlines (scan1 and scan2) were placed on the map, and 32 fractures and nine faults are captured. In Figure 45, there are more closely spaced fractures than widely spaced fractures. Due

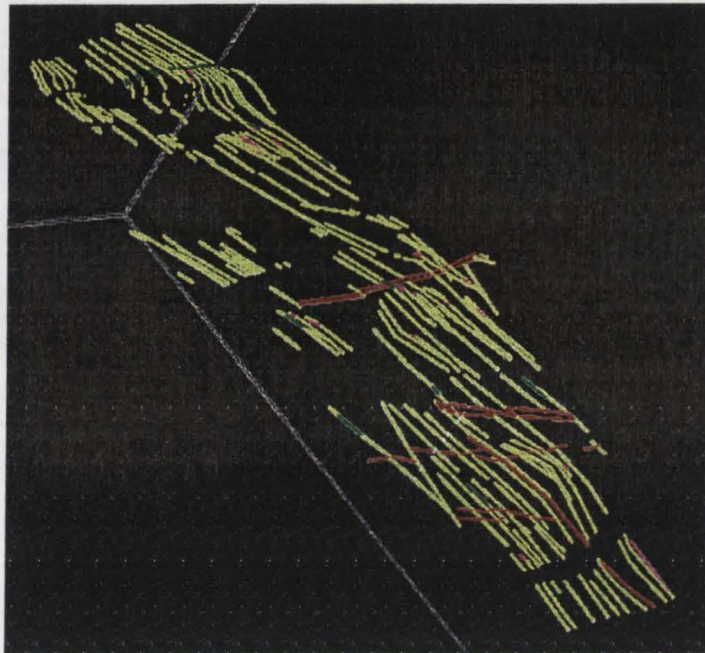


Figure 43. A top left view of a modified Segall and Pollard (1983a) Kip Camp map showing a gentle topographic rise in three-dimensional visualization.

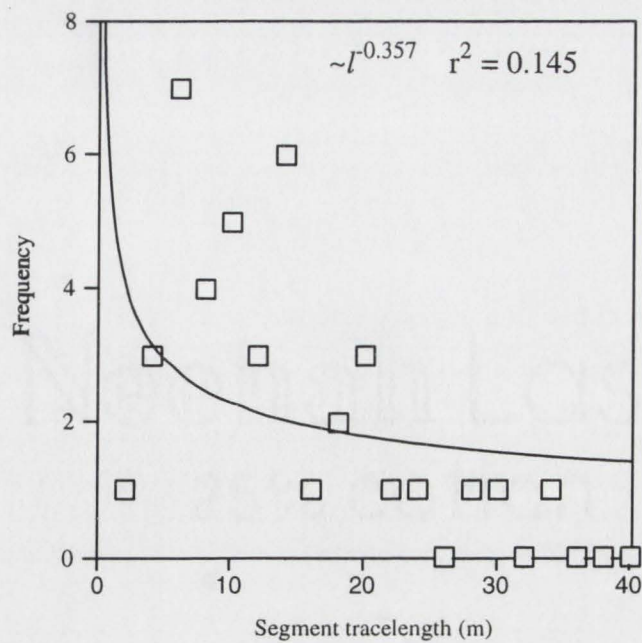
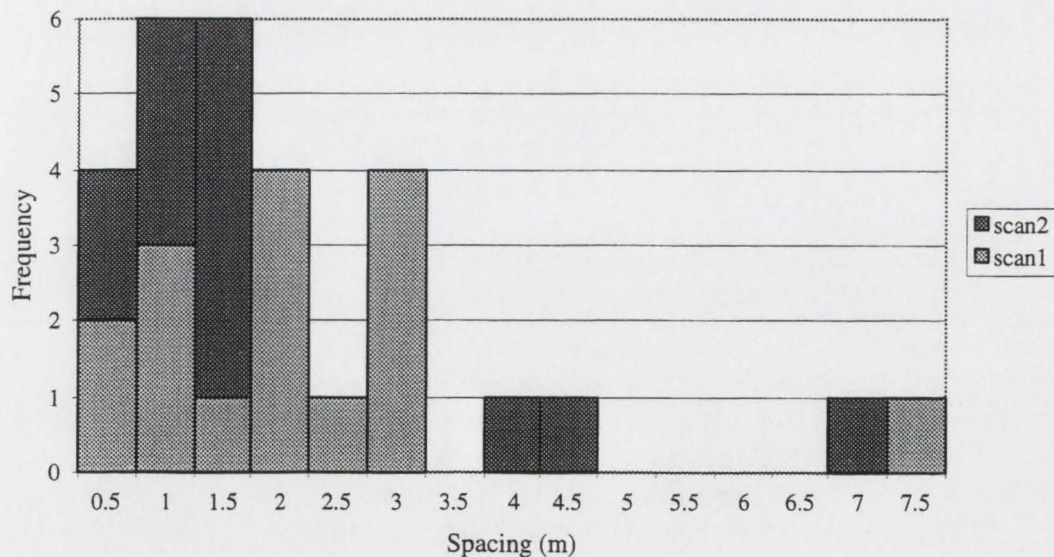


Figure 44. Plot of the frequency of Kip Camp fault segment tracelengths, with a power-law distribution.

to the lack of faults in scan2 region, scan1 reveals there is a wider spacing among faults in comparison to fractures (Fig. 46). By using the criteria for fracture, joint, and fault established in the earlier terminology section, 36 faults were identified and 97 fractures (excluding splays) were counted and the number of fault to fractures ratio is 27.1%. From the 36 faults, the number of faults showing splay fractures ratio is 38.8%. Only 14 faults in this population showed splay fracturing and no splay angle was measured from the splay faults.

#### Reflecting Bowl Fault Population

The topographic survey of the Reflecting Bowl covered an area of 66 m by 21 m with an approximate topographic relief of 25 m and was mapped in 1:100 scale (Fig. 42). The subparallel fractures generally trend in the direction of  $060^\circ$  and dip steeply to the south. The fracture lengths range from a few meters to several tens of meters. The tracelength distribution of fault segments is similar to Kip Camp, with



**Figure 45. Histogram of Kip Camp fracture spacing at two scanline locations. Both scanlines show a concentration of closely spaced fractures. The scanlines encounter a total of 32 fractures.**

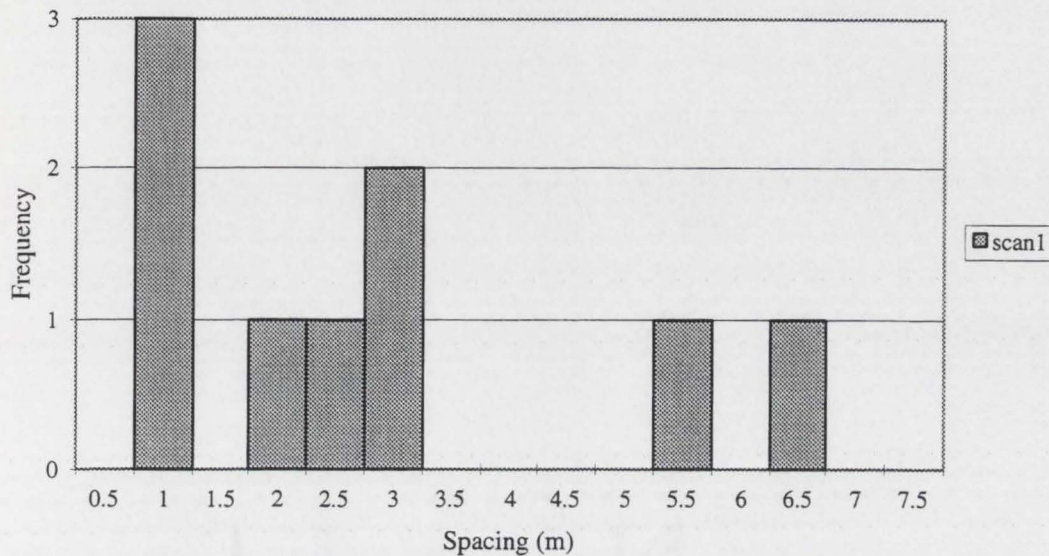


**Figure 46. Histogram of Kip Camp fault spacing at two scanline locations. Scan2 does not encounter any fault and where scan1 encounters fault, there is a concentration of closely spaced faults. The scanlines encounter a total of nine faults.**

no clear trend and a poor power-law distribution of  $l^{-0.233}$  with  $r^2 = 0.054$  (Fig. 47). Note that the  $n$  value for fault segment distribution is also at odds with Segall and Pollard's (1983b)  $n$  value for joint distribution. Out of the 60 fault segment traces, the longest measured is 20.2 m.

There is a second set of fractures that generally trend in a direction of  $330^\circ$  and are also steeply dipping. These NW-trending fractures are much shorter than the NE-trending fractures and the crosscutting between the two sets of fracture is unclear. Two groups of closely spaced NW-trending fractures have created a zipper crack-like feature in the direction of  $005^\circ$  (Fig. 48). The fractures are generally 35 cm to 1 m in length, with spacing intervals of 2 to 14 cm, and are epidote-chlorite rich. It is believed these fractures are due to very small bending, the same process responsible for the Kip Camp monoclinical kinks (James P. Evans, 1998, personal commun.).



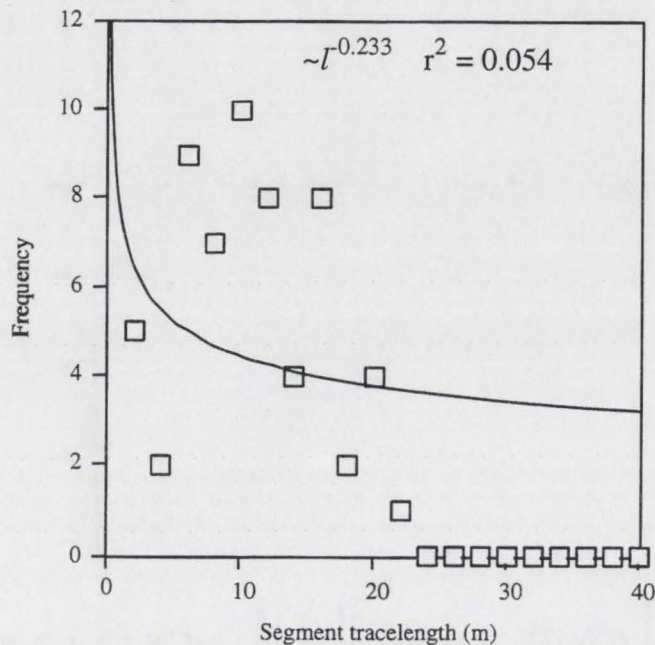


**Figure 47. Plot of the frequency of Reflecting Bowl fault segment tracelengths, with a power-law distribution.**

The dikes in this area trend in a similar direction as the NE-trending fractures and faults with very few crosscuts, rendering them almost useless for any slip determinations.

This area is dominated by brittle deformation with a few small right-lateral contractional deformations. Individual fractures range from less than 0.1 mm to greater than 1 cm in width. Three random scanlines (scan1, scan2, and scan3) were placed across the Reflecting Bowl, and the fault spacing and fracture spacing are plotted on Figures 49 and 50. The scanlines have captured a total of 56 fractures and 24 faults. From Figure 49, the scan1 shows a high concentration of fractures with spacing of 0.5 to 1 m and the scan2 reveals a similar trend as scan1 and it extends the spacing range from 0.5 to 1.5 m. The fracture spacing for scan3 has a high frequency of fractures at 0.5 m and 3.5 m (Fig. 49). As for the spacing between faults, all three scanlines show widely dispersed distributions except the 1-m fault

(a)



(b)

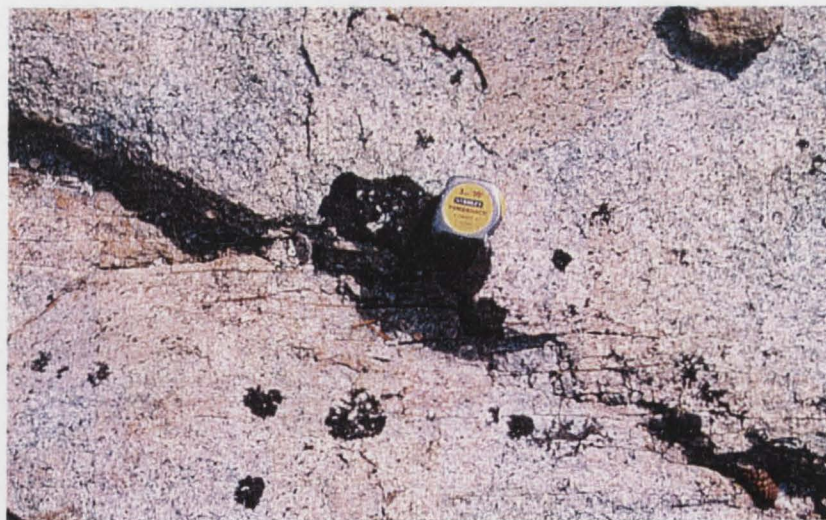


**Figure 48. Zipper crack-like band without a central fracture in Reflecting Bowl. (a) The eroded fractures caused a 005° trending channel. The white chalk in the foreground marks the beginning of the fractures and the yellow tape is 1-m long. (b) Closeup of the zipper crack-like band and its alteration halos.**

spacing frequency spike for the scan2 (Fig. 50). Many fractures in the area do not exhibit dilatant splay fracturing at their ends. Three fault step complexes were recorded and one of the complexes does not have well-expressed connecting fractures; instead it has highly visible alteration haloes.

There is a large rhombochasm in the middle of the study area that has epidote-chlorite-filled fracture traces surrounding the rhombochasm, and after removing dirt and debris from the rhombochasm, a thick epidote-chlorite fault vein could be traced out (Fig. 51). I postulate that there was a highly fractured fault step complex before it was weathered to produce a rhombochasm. The most interesting features in this area are the two faults in the north-central portion of the map area, which have been grouped together as RBJ-1. The two overlapping faults are a centimeter apart, with no deformation in the overlap region and multiple

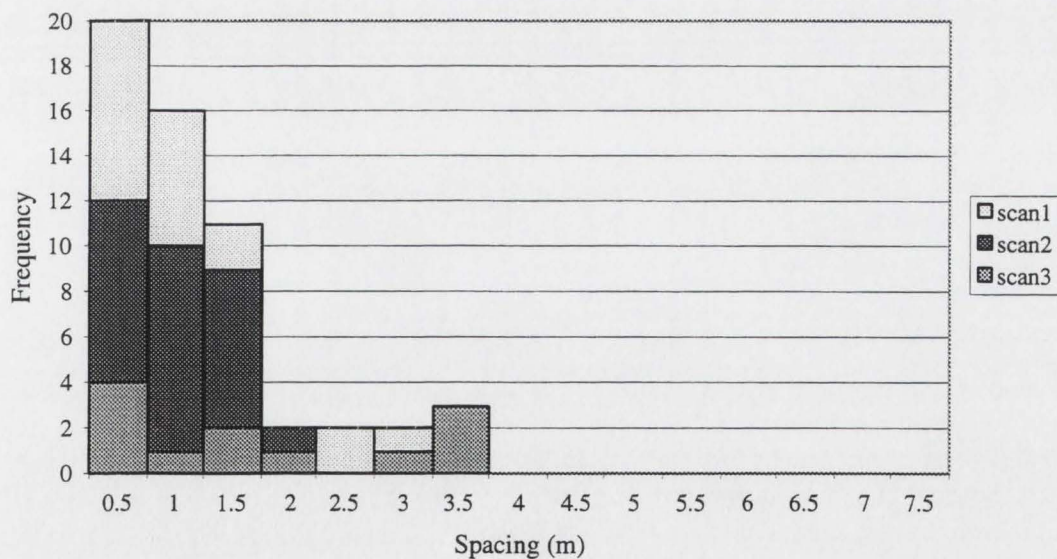


**Figure 49. Histogram of Reflecting Bowl fracture spacing at three scanline locations. The scan2 has high frequency of fractures at the 0.5 m to 1.5 m spacing while scan1 has high fracture count from 0.5 m to 1 m spacing. The scan3 has a more varying fracture spacing than scan1 and scan2. The scanlines encounter a total of 56 fractures.**

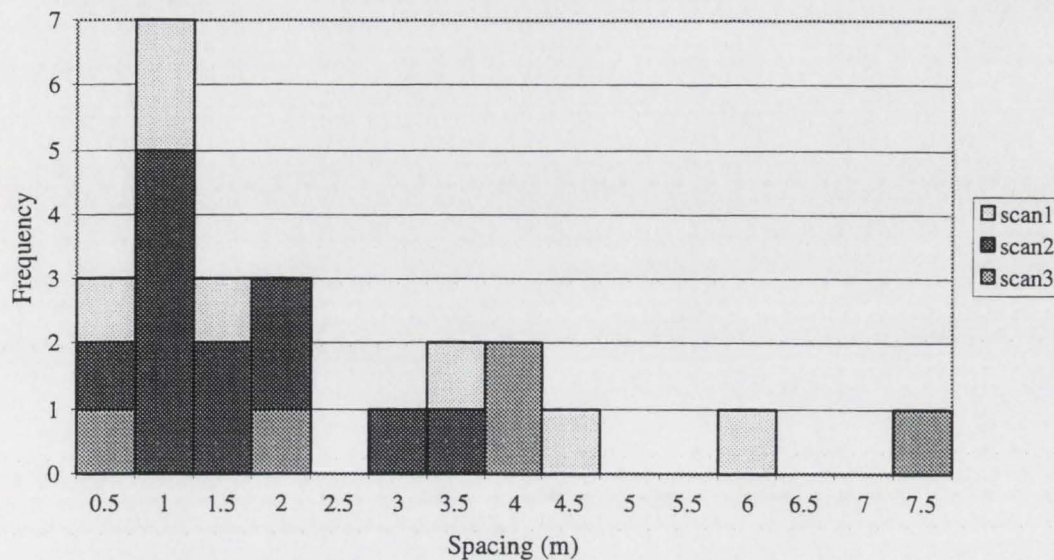


**Figure 50. Histogram of Reflecting Bowl fault spacing at three scanline locations. All locations show varying fault spacing; however, at scan2, there is a high concentration of faults at 1 m spacing. The scanlines encounter a total of 24 faults.**

discontinuous secondary fractures near the end of the fault trace. Interestingly, the faults have dilatant splay fracturing on each end as if the faults were behaving as one when the splay fracturing occurred. The splay angle for Reflecting Bowl has a mean and standard deviation of  $29^\circ \pm 10^\circ$  (Fig. 52).

By using the same criteria for fractures, joints, and faults as I did for Kip Camp, 23 faults were identified and 116 fractures counted (excluding splays and the N-trending fracture set), and the ratio of the number of faults to fractures is about 16.5%. Eleven splaying faults were counted among the 23 faults, and the ratio of the number of faults showing splay fractures is 47.8%.

#### Summary for Reflecting Bowl and Kip Camp Fault Populations

An attempt was made to examine the relationship between mineralized cavity length and width with fault displacement for all mapped faults that were examined.

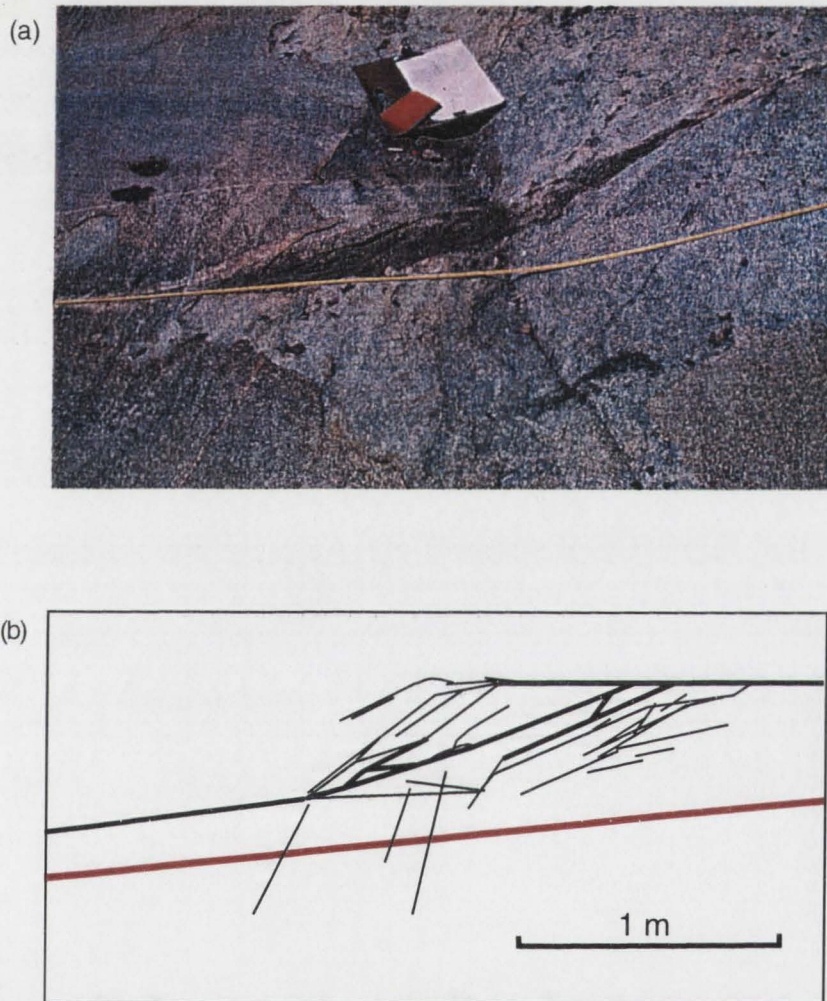


**Figure 51.** Photo and map of Reflecting Bowl rhombochasm. A yellow measuring tape is in the photo foreground and a 1-cm thick felsic dike near the mapboard is in the background. The map shows the fractures surrounding and in the rhombochasm. The heavy black line is a 1-cm thick epidote-chlorite fault filling. The green line shows the rhombochasm boundary and the red line is the 1-cm thick felsic dike.

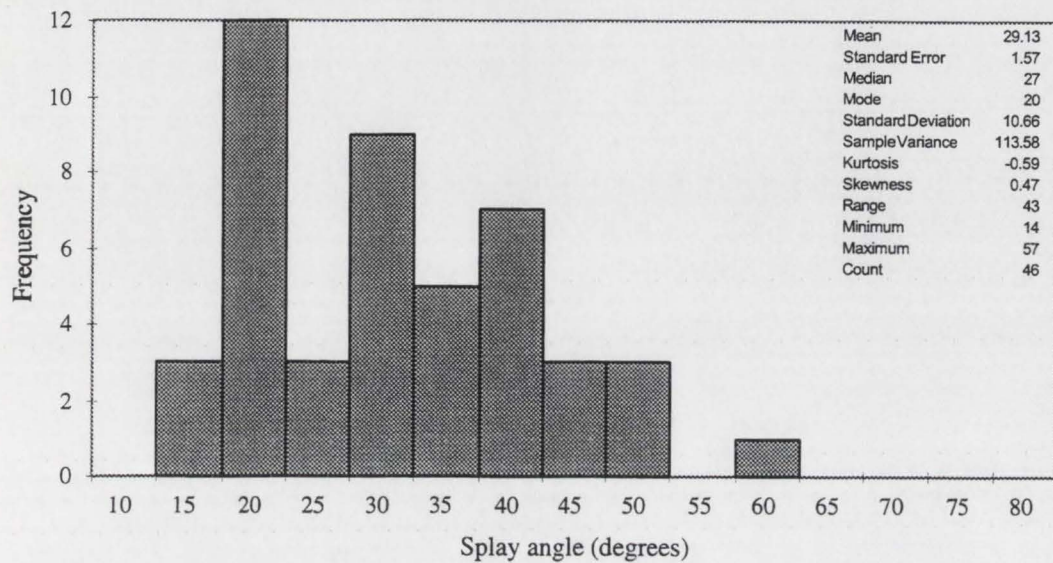


**Figure 52. Histogram of Reflecting Bowl splay angle. The chart shows a high 20° splay angle count and the statistics of the distribution are given in the top right corner.**

Figures 53a and 53b show that mineralized cavity size does not correlate with fault displacement. There is pervasive chlorite-epidote mineralization in most fractures but no consistent pattern of quartz mineralization along the fractures. The mineralized quartz has appeared largely as lenses and there are only a few instances of a single, continuous quartz vein in a fault. Though quartz was mineralized in the complex fault step fractures, subsequent weathering created a rhombochasm and removed the quartz. Another place for quartz mineralization would be the accommodation space created at and near the fault kink.

The length frequency of fractures for the Reflecting Bowl area shows that fracture length follows a power-law distribution of  $l^{-1.219}$  with  $r^2 = 0.778$  (Fig. 54), which is within the reported  $n$  value of 1.2 to 1.8 of Segall and Pollard (1983b). The longest joint trace of the 70 joints is 18 m. Both populations have poor power-law distribution for fault segment tracelengths. Kip Camp has a fault segment tracelength power-law distribution of  $l^{-0.357}$  with  $r^2 = 0.145$  (Fig. 44) and Reflecting

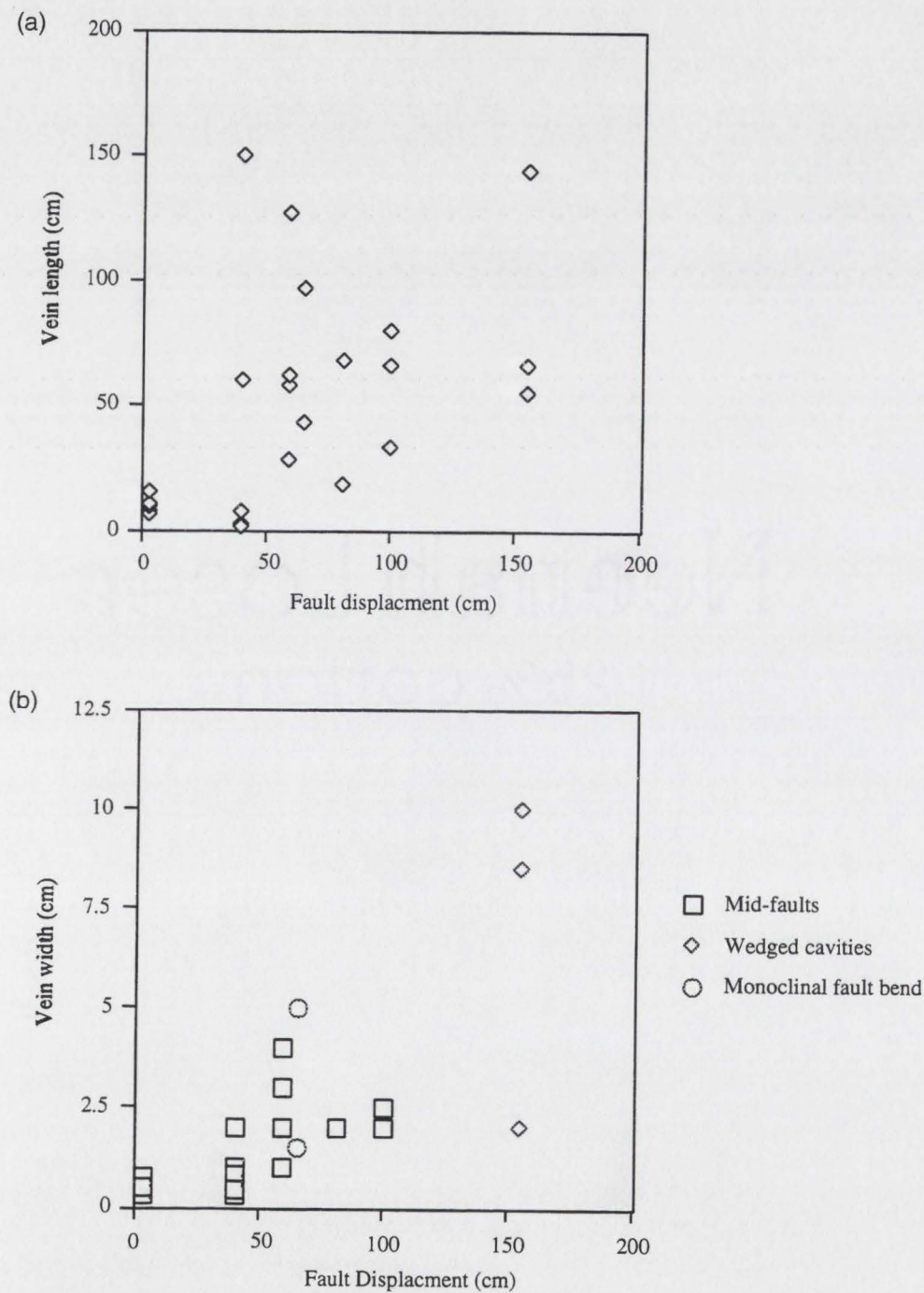


**Figure 53. Plots of mineralized cavity dimensions vs fault displacement. (a) Cavity length vs fault displacement shows no correlation. (b) Cavity width vs fault displacement shows no correlation.**

Bowl has  $l^{-0.233}$  with  $r^2 = 0.054$  (Fig. 47). Note that the  $n$  value for fault segment distribution is at odds with Segall and Pollard's (1983b)  $n$  value for joint distribution. Fault segment tracelengths of 158 fault segments were compiled from all mapped areas and plotted on a distribution chart (Fig. 55). The power-law relationship of the distribution is  $l^{-1.180}$  with  $r^2 = 0.568$ , and this compiled fault segment distribution  $n$  value is near the reported  $n$  value for Segall and Pollard's (1983b) joint distribution. The following problems were note about the length of fault segments:

- 1) some faults could be so well coalesced that they could appear to be an undifferentiable fault;
- 2) several fault tracelengths that were restricted (censored) by the mapping boundary or ground cover; and
- 3) a splay with an extremely low angle angle could be mistaken to be added fault segment length.

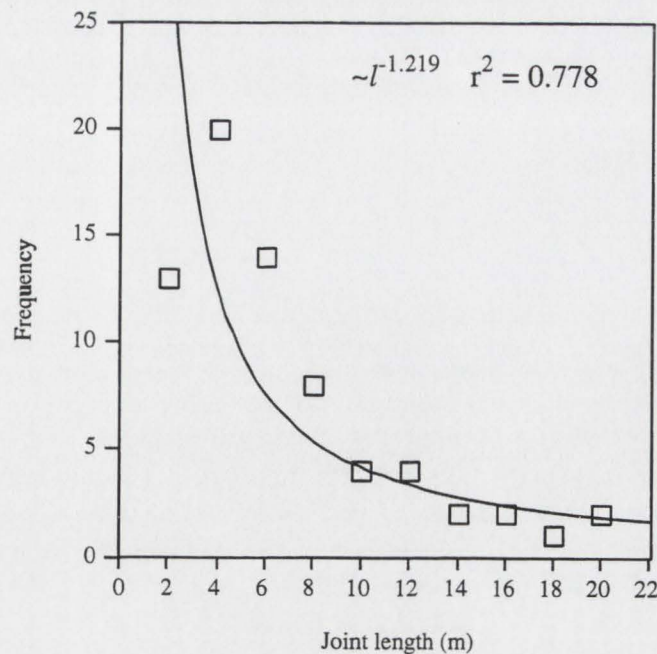


**Figure 54. Frequency of joint length at Reflecting Bowl exhibiting a power-law distribution with  $n = -1.219$  and  $r^2 = 0.78$ .**



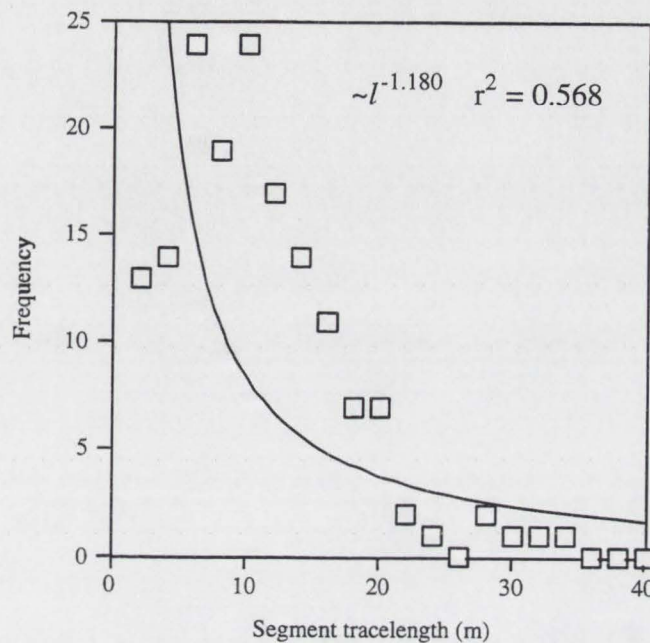


**Figure 55. Frequency of all mapped fault segment tracelengths showing a power-law distribution with  $n = -1.18$  and  $r^2 = 0.57$ .**

To minimize the problem of censoring, another distribution chart with 69 uncensored fault segment tracelengths was plotted and the power-law relationship is  $l^{-0.788}$  with  $r^2 = 0.412$  (Fig. 56). Note that this uncensored fault segment distribution  $n$  value is below the reported  $n$  value for Segall and Pollard's (1983b) joint distribution. Fault segment tracelengths for both Kip Camp and Reflecting Bowl were plotted and they have no fitting trend but there are high concentrations of short fault segments (Figs. 57 and 58).

The lack of uniformity in fracture spacing and fault spacing at Reflecting Bowl is not surprising, as this was observed in similar settings in earlier studies (Segall and Pollard, 1983a; 1983b). However, it appears there are more closely spaced fractures than closely spaced faults and few widely spaced faults and fractures.

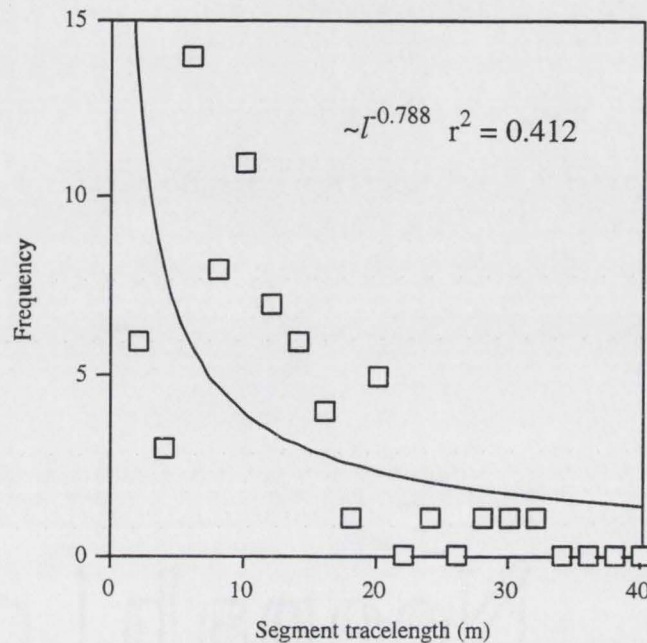


**Figure 56. Frequency of all fully exposed fault segment tracelengths showing a power-law distribution with  $n = -0.79$  and  $r^2 = 0.41$ .**

### Thin-Section Observations

The microscopic structure and mineral assemblages of samples collected from fractures and faults were examined in thin-section for style and type of mineral deformation and alteration. Since the study sites are in the John Muir Wilderness area, power tools were not permitted. The samples were extracted with hammer and chisel, and good exposures of fault and splay fracture juncture were rare. However, almost all aspects of strike-slip fault deformation were sampled. Oriented samples were collected in the field and the samples were reoriented in a sandbox for cutting.

Previous investigations, except Robeson (1998), provided only a few photomicrographs of specific fault features over several papers (Segall and Pollard, 1983a; Segall and Simpson, 1986; Martel et al., 1988; Bürgmann and Pollard, 1994). In this section, we will navigate through thin sections from fault KJ-4 splay fractures, Reflecting Bowl secondary fracture set, and fault KJ-1B fault fill and secondary

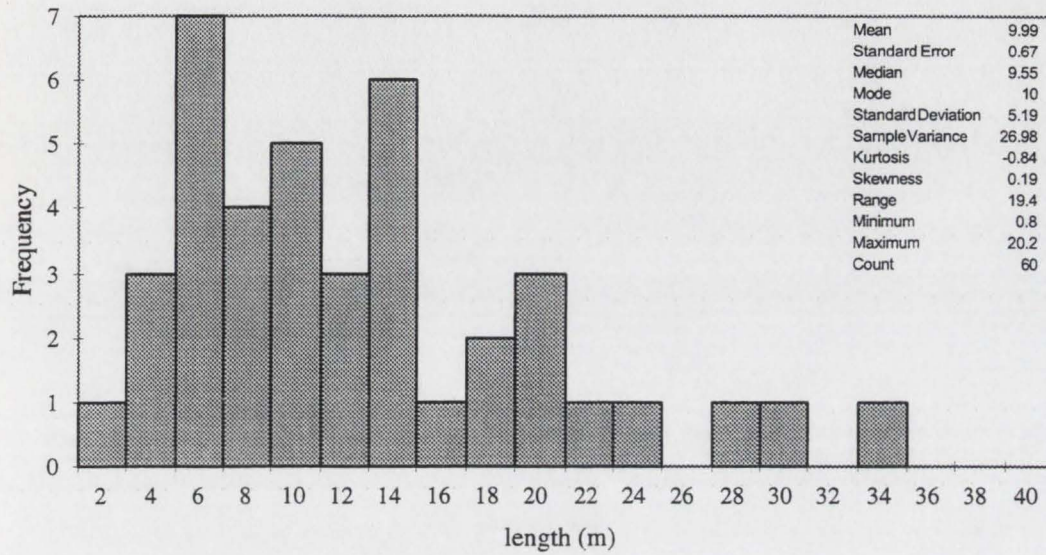


**Figure 57. Histogram of Kip Camp fault segment traelength. The chart shows most of the traelengths are in the range of 6 to 14 m and the statistics of the distribution are given in the top right corner.**

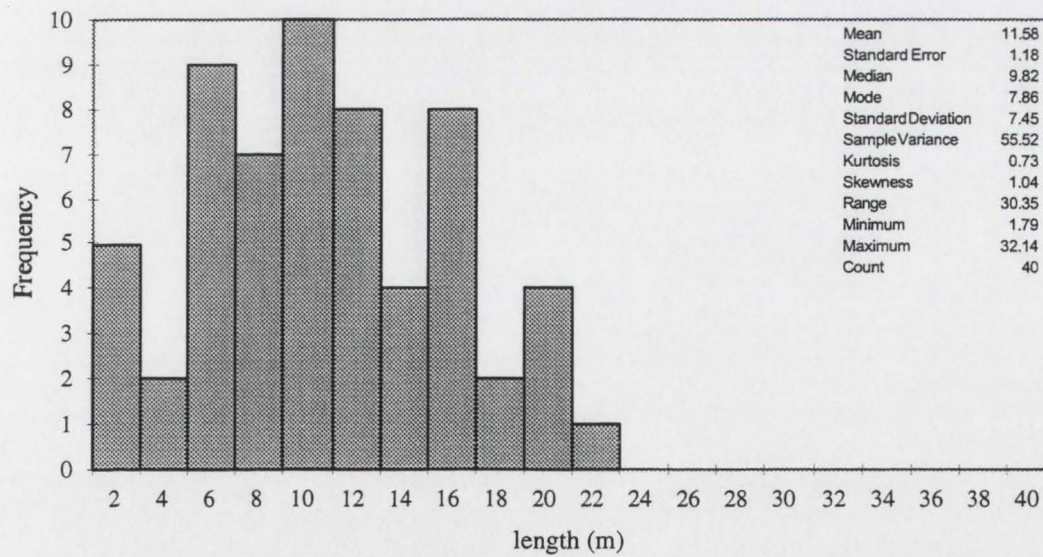


**Figure 58. Histogram of Reflecting Bowl fault segment traelength. The chart shows most of the traelengths are in the range of 6 to 16 m. The statistics of the distribution are given in the top right corner.**

fractures. We will examine more fault-fill thin sections from Reflecting Bowl (RS-6B) and Bear Creek camp (BJS-2); and finally thin sections of the right-lateral step from fault BJ-B.

A sample (KJ4/296) from KJ-4 was taken from the fault step that linked KJ-4 and KJ-4A (Fig. 59a). The sample was located about 2 m from a dike with 4 cm of offset on fault KJ-4A. The other offset indicator is the reabsorbed xenolith along fault KJ-4, about 9.8 m away, with 50 cm offset. The step is probably a dilatant fracture that was formed to accommodate the strike-slip deformation. The fracture is filled with large euhedral strain-free quartz, high birefringence biotite, a zeolite-like mineral, and epidote-chlorite aggregates that showed no evidence of deformation and no evidence of slip (Fig. 59b). The host rock minerals are undeformed and relatively damage-free.

Thin sections RS-2A, RS-2B, and RS-7 are samples from the NW-trending fracture set in Reflecting Bowl. The RS-2 is from an isolated fracture and RS-7 is from the easternmost closely spaced zipper crack-like fracture. Both samples are similar. There is no evidence of shearing, as they are filled with unstrained epidote and the fill crosscuts feldspar and quartz without any offset (Fig. 60). The surrounding host rock is undeformed, but most of its feldspars are sericitized and the biotites are altered; such evidence suggests they were hydrothermally altered.

A sample from fault KJ-1B (Fig. 61a) shows a fracture crosscuts feldspar crystal without any evidence of slip, indicating the secondary fractures of KJ1/396D formed as dilatant fractures (Fig 61b). Figure 61b demonstrates evidence of movement of hydrothermal fluids because of the contrast of the minerals within the fracture and outside of it. Altered biotites are found at the junction of the main fault and splay fracture (Fig. 61c). This may be evidence for a splay fracture nucleation, as sites with biotite may be where the fractures initiate (Gottschalk et al., 1990).

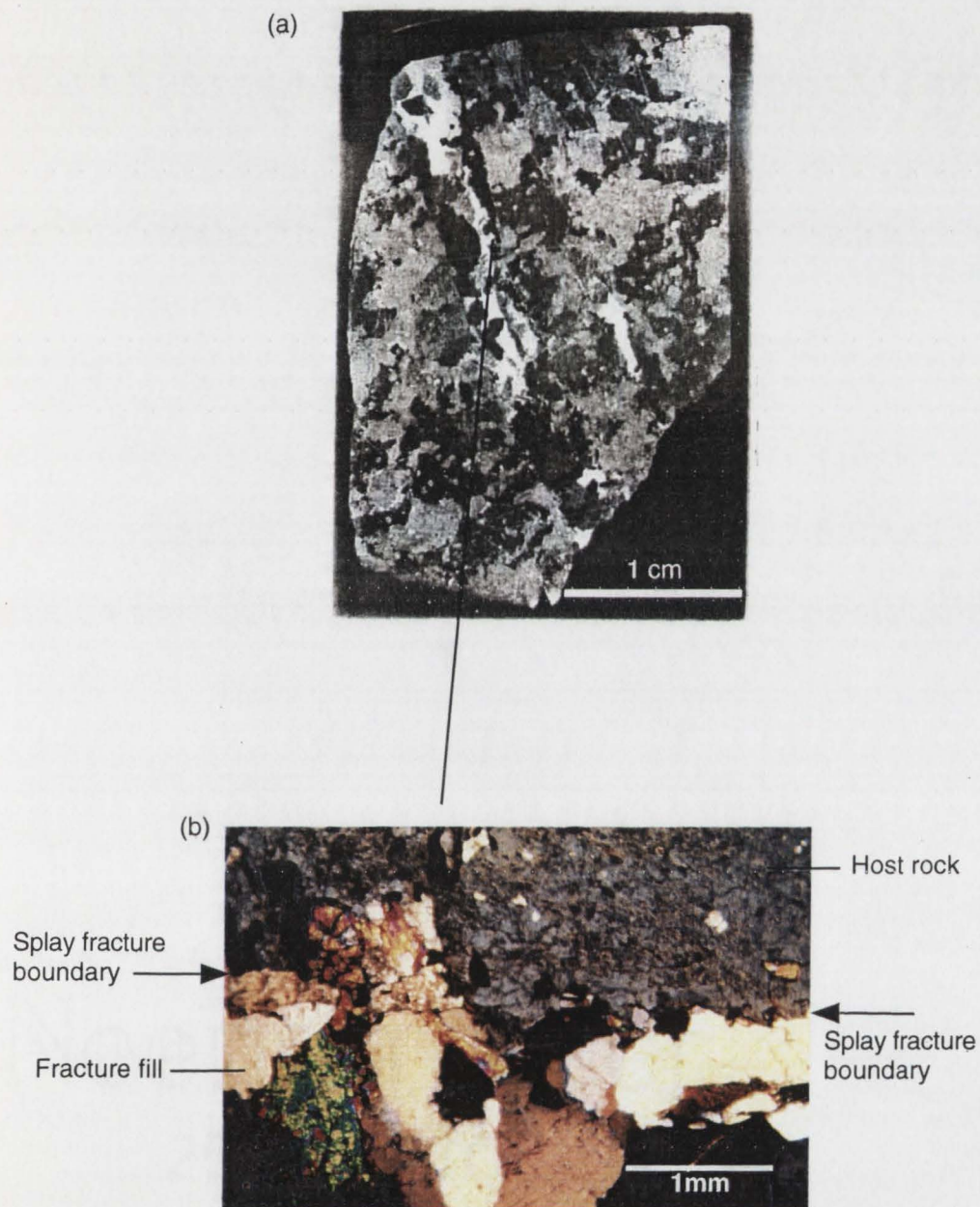


**Figure 59.** Thin section of KJ4/296 from fault KJ-4. (a) Photo negative of KJ2/296 showing two splay fractures. (b) Photomicrograph of unstressed euhedral splay fracture filling against wall rock.



**Figure 60. Photomicrograph of RS-7 from a Reflecting Bowl fracture showing a feldspar crystal that is not offset by the fracture.**

Usually subsequent shearing would easily destroy such evidence, as the fault would be filled with cataclasite. In addition, the epidote-filled fracture shows no evidence of collateral damage. At least two zones of epidote-chlorite aggregates are recognized in the fault of KJ1/396D, indicating more than one episode of mineralization (Fig. 61d) and also two different modes of slip: the debris-free region and cataclasite region. The debris-free zone has little or no cataclasite, which could be located in small quantities along the fault wall and in the cataclasite zone. The other zone is a cataclasite-filled epidote-chlorite aggregate and it is the dominant fault fill that occupied the cavities along the fault walls. It appears that the debris-free aggregate was first deposited before it was fractured and subsequently filled by the cataclasite zone. The splay fracture fill did not contain any cataclasite. Sample KJ1/396 is from fault KJ-1B where a net slip of 65 cm had occurred.

A sample (RS-6B) of fault fill was collected from the middle of a Reflecting Bowl fault and similar zones of epidote-chlorite aggregates could be identified with a

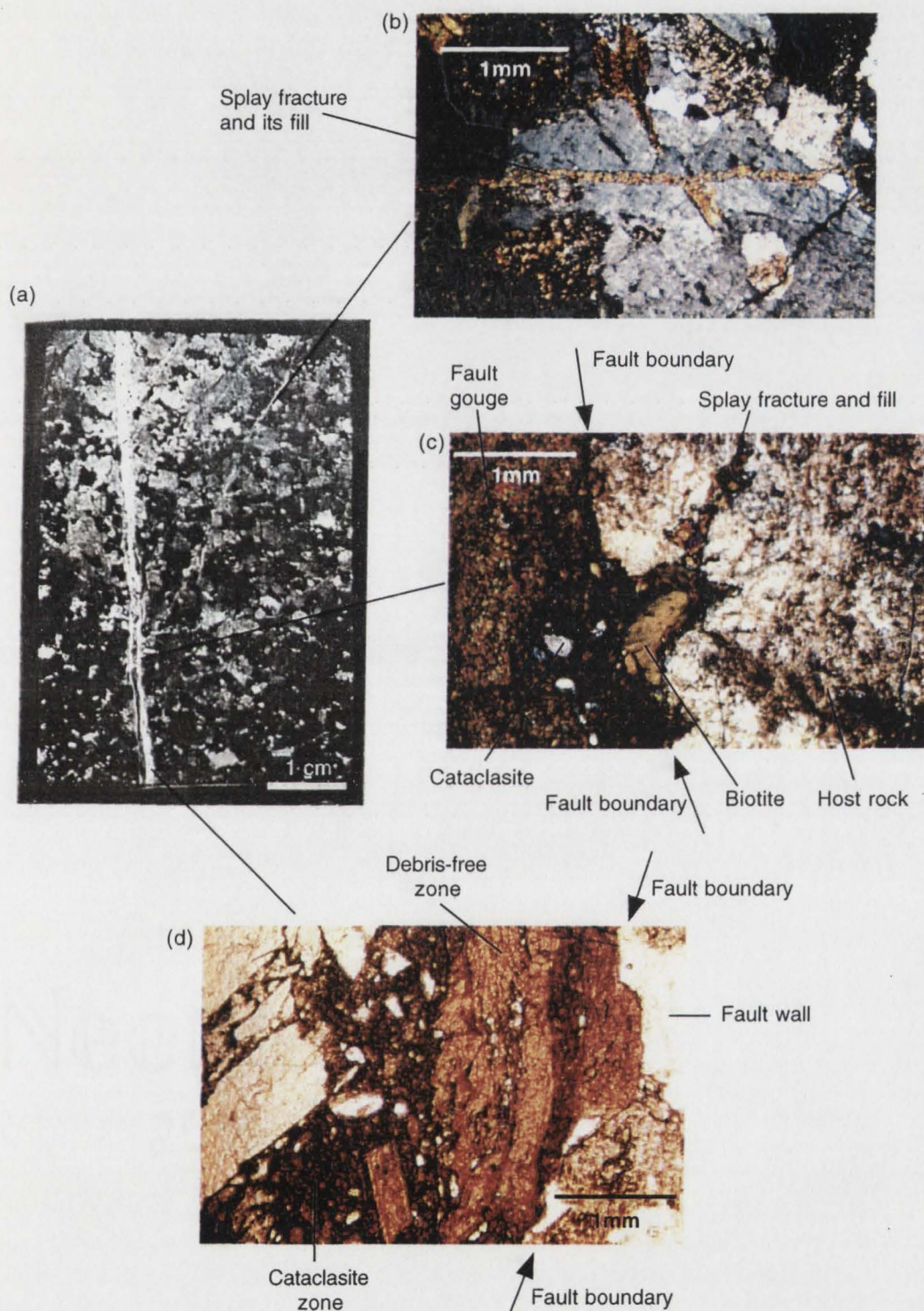


**Figure 61.** Thin section of KJ1/396D from fault KJ-1B. (a) Photo negative of KJ1/396D. (b) The feldspar is not offset by the splay fracture. (c) An altered biotite at the junction of a splay fracture. (d) Distinct zones of cataclasite and non-cataclasite in unpolarized light.

few additional finer- and coarser-grained epidote aggregates, indicating a history of episodic slip movements and hydrothermal events (Fig. 62a). The texture in Figure 60a also suggests several episodes of flow or movement, giving some evidence of flow related to slip. Large wall-rock fragments are also in the fault, as they were probably "plucked" through the repeated actions of fault grinding and pulverization (Fig. 62b). Some of wall-rock fragments were dynamically recrystallized, leaving behind islands of fine-grained quartz aggregate that were freed from other minerals and have the appearance of quartz mineralization to unaided eyes. Unfortunately, there is no offset indicator along the fault to constrain its slip.

The quartz mineralization cavity sample from BJS-2 reveals a ductile deformed vein of foliated fine quartz grains with a sharply defined fault boundary (Fig. 63a). The quartz vein is divided into two segments by fault gouge and each quartz segment is free from other minerals (Fig. 63b). Epidote fill is found in a breach of the quartz foliation and a portion of the vein was brittlely deformed. A quartz mineral band running the length of the ductile fabric was probably the result of dynamic recrystallization (Passchier and Trouw, 1996). Many of the minerals in the surrounding wall rock show some form of dynamic recrystallization, sericitization of feldspars, intracrystalline deformation, recovery, and static recrystallization. The sample is from fault BJ-10 where a dike experiences an offset of 59 cm.

A sample (BJ28D), oriented almost parallel to the slip direction, was retrieved from a right-lateral step in BJB-2 and this sample straddled two dikes with offsets of 1.55 m and 0.6 m. There is no opportunity for net slip calculation. The thin-section reveals a sharp fault contact between the ductile deformation, with different zones of dynamically recrystallization and unfoliated wall rock (Fig. 64a). The first zone is the host rock with phenoclasts of feldspars and quartz. The host rock minerals show signs of dynamic recrystallization and shearing of altered biotites (Fig. 64b). In the



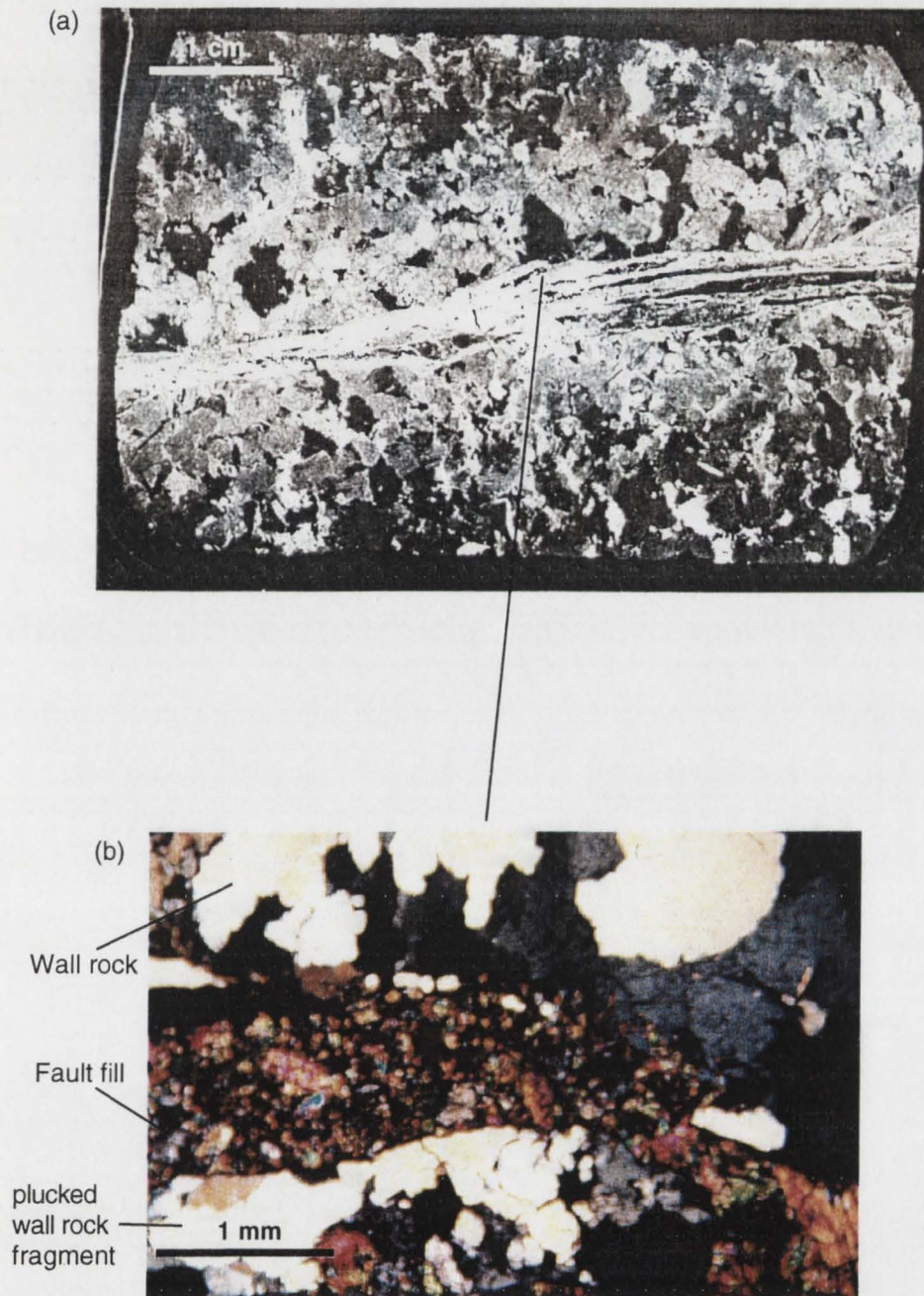


**Figure 62.** Thin section of RS-6B from a Reflecting Bowl fault. (a) Photo negative of RS-6B. (b) Photomicrograph of a plucked wall rock fragment.

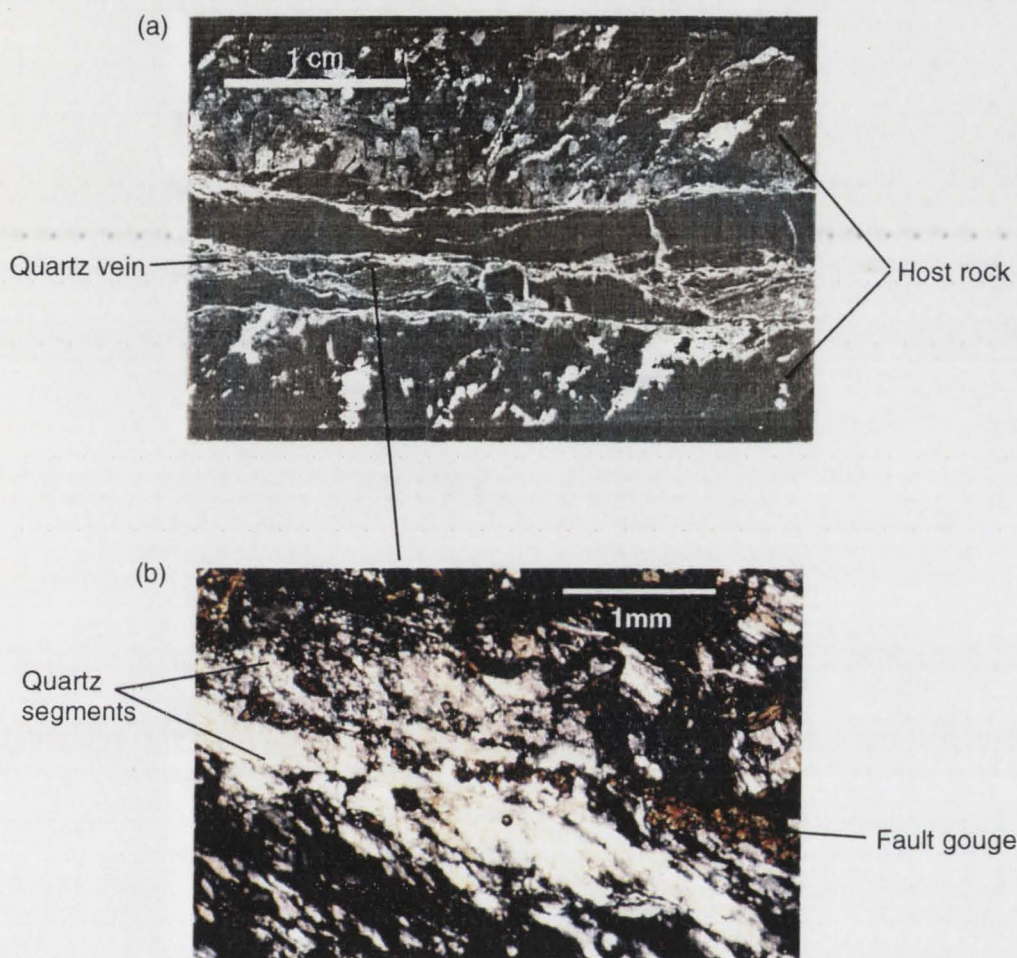


**Figure 63.** Thin section of BJS-2 from fault BJ-10. (a) Photo negative of the thin-section. (b) Photomicrograph showing a vein of epidote-chlorite partitioning ductile quartz.

fault vein, there is a piece of former host rock in a sea of epidote-chlorite-like groundmass and the broken host rock has been dynamically recrystallized. It seems that there is a host rock trapped between the fault and the diffuse zone (Fig. 64c). The trapped host rock has a similar appearance to the broken host rock, with both fine-grained and coarse-grained crystals and more intensely dynamic recrystallization. It is partially penetrated by epidote-rich hydrothermal fluid from the diffuse zone, and almost all of its biotites have turned into chlorite. The diffuse

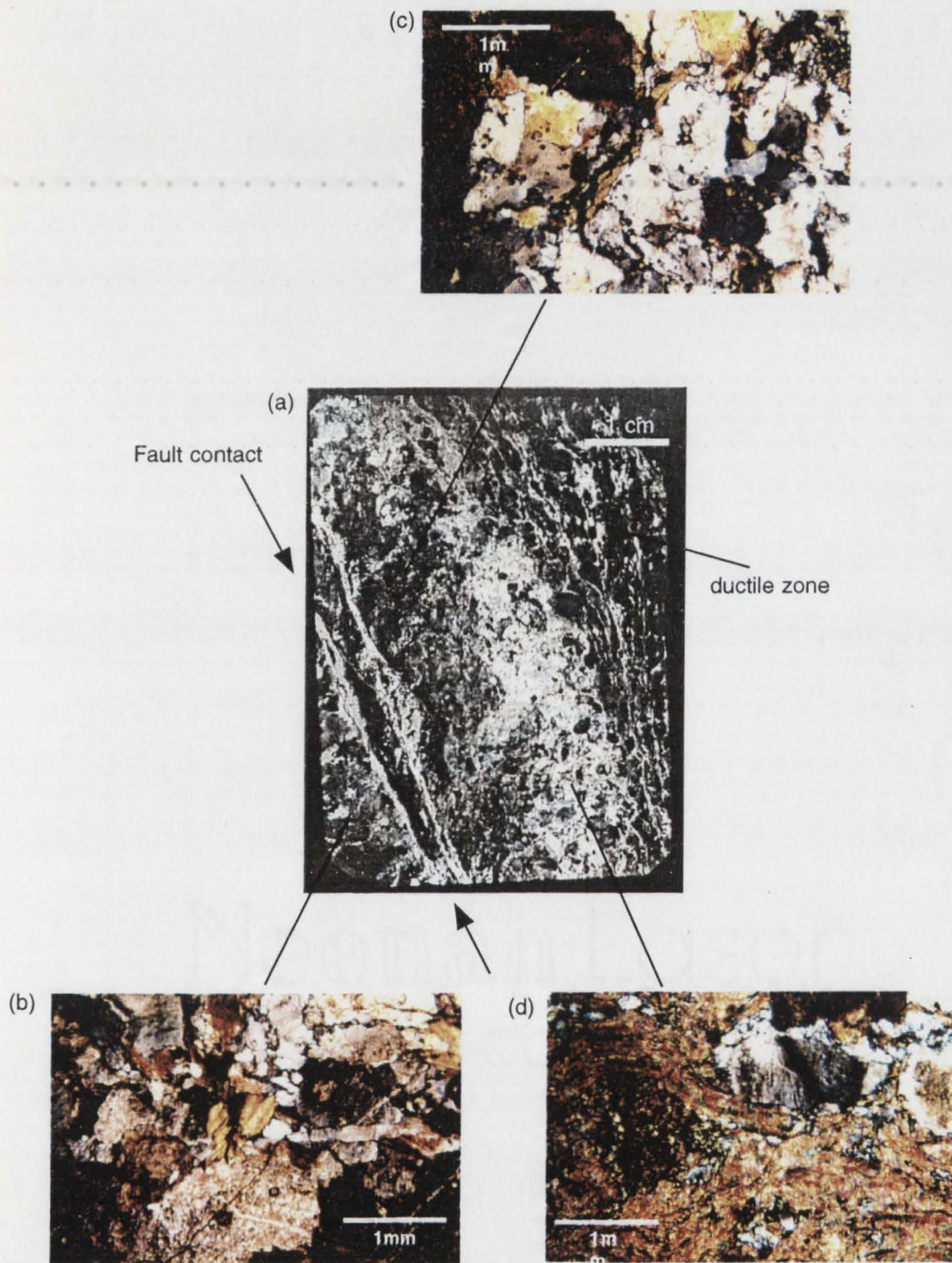


**Figure 64.** Thin section of BJ-28D from a right-lateral step in fault BJ-B. (a) Photo negative of the thin section. (b) Photomicrograph of host rock. (c) Photomicrograph of trapped host rock. (d) Photomicrograph of diffused zone.

zone is dominated by epidote mineralization with little or no signs of any foliation and some signs of chlorite (Fig. 64d). It was noted that the diffuse zone is not exposed on the ground surface. X-ray diffraction (XRD) of a diffuse zone sample revealed very little quartz. Hydrothermal activity probably contributed to the high incidence of feldspar sericitization found in this zone. There is fine-grained quartz aggregate, but it is not foliated as in the ductile zone. The ductile zone is distinctive, as it is mylonitic with bands of foliated epidote-chlorite-fault gouge mix and quartz.

### Summary of Observations

All the studied joints and faults trend northeast with the exception of the Reflecting Bowl secondary joint set, which trends in a northwesterly direction. The majority of the fractures (including joints and faults) terminate without secondary fractures. Faults with secondary fractures have left-lateral dilational steps or right-lateral compressive steps. In the 91 mapped faults, the associated fractures are usually found in the dilational quadrants and have no fractures in the opposite quadrants. The exception is the Bear Creek fault area in which the complex fault-step has both dilatant and compressive secondary fracture surfaces. The presence of a zipper crack band was not observed among the 158 mapped fault segment traces, and isolated faults with secondary fractures are rare. The longest fault segment trace is 32.14 m and the longest joint trace is 22 m. There is a high number of short fault segments in segment tracelength distributions. There are more closely spacing fractures than closely spaced faults and few widely spaced faults and fractures. Fault segment distribution  $n$  values for individual fault populations and uncensored fault segment distributions are well below the reported  $n$  value for Segall and Pollard's (1983b) joint distribution, and only the compiled fault segment distribution has an  $n$  value near the reported  $n$  value for Segall and Pollard's (1983b) joint distribution.

These sheared faults can have offset up to 1.55 m. Regrettably, there are not enough offset indicators on any of the mapped faults to provide slip profiles for individual faults. All of the study sites are about equal distance (1.2–1.5 km) from the Mono Creek Granite, and only the Reflect Bowl and Bear Creek areas have foliated granodiorite fabric related to fault slip.

There is no trend between fault width and fault slip. The width could range from 1 mm to more than 1 cm wide. The faults did not thicken in their centers and then pinch out at their ends.

There is generally a high concentration of splay fractures near faults, with spacings of 5–15 cm, and the splay-fracture spacings far from fault is more disperse. As perpendicular distance increases from faults, there is a pattern of wider splay spacing and fewer splay fractures.

The combined data of all splay-fracture angles from 29 faults with splay fractures (excluding the 14 faults with splay fractures from Kip Camp fault population) resulted in a mean and standard deviation of  $39^\circ \pm 13^\circ$  (Fig. 65). Less than half of the 91 faults (47.3%) exhibited splay fracturing. The distribution of splay-fracture angle usually shows a single peak in the dominant splay angle, and splay-fracture angles below  $10^\circ$  and greater than  $80^\circ$  are rare. There is an apparent decrease in splay angle towards the fault ends.

The splay tracelength distribution charts have high concentrations of short tracelengths (20, 30, or 40 cm, depending on multiple fracture groups) with rapid decrease in the number of long tracelengths. There is an apparent increase in splay tracelength towards to the fault ends. The maximum tracelength of multiple splay fracture groups is restricted by its distance orthogonal to the fault trace. The splay-fracture damage zone appears to maximize its width before the end of the fault and narrows at the end of fault. The decreasing splay angle near fault ends could be

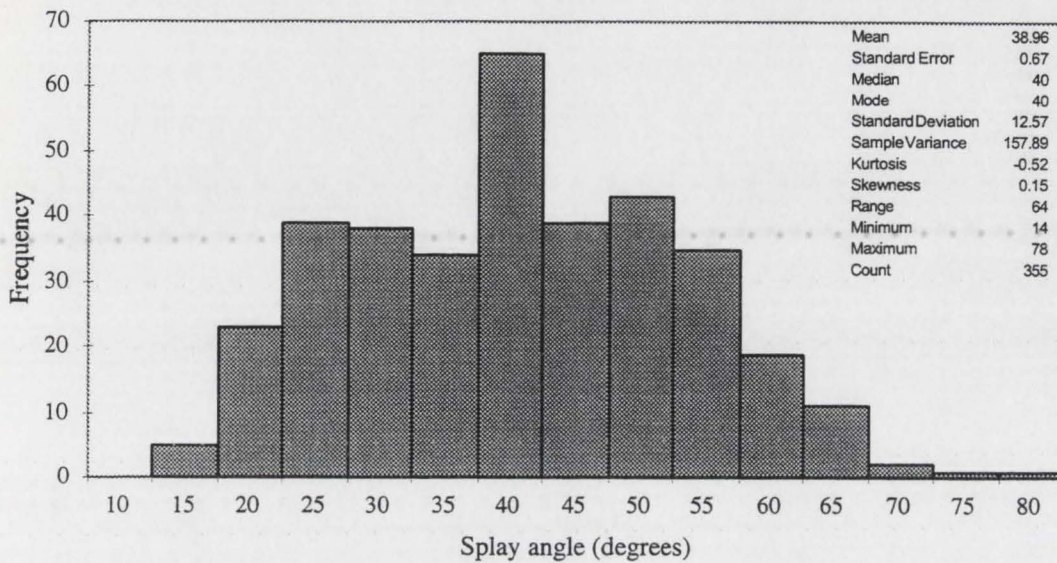


**Figure 65. Histogram of compiled splay-fracture angles from all mapped splay fractures. The chart shows most of the angles, from 29 faults with splay fractures, would likely to appear in the range of 15° to 65°. The statistics of the distribution are given in the top right corner.**

restricting the splay-fracture damage zone from widening even though the splay tracelength has increased towards the fault ends.

Fault displacement could result in single, multiple, or no splays at all. From Segall and Pollard (1983a) Kip Camp, KJ-4, BJ-B, and other maps, there is no correlation between displacement amount and the number of splay fractures, and the locations of splay fracture nucleation sites seem random.

All splay-fracture traces are linear with the exception of fault SF-2, which has splay-fracture traces that could be curvilinear. In addition, splay fractures can also bifurcate and can display en-echelon features. The dihedral angles between the splay plane and the fault plane from all maps range from 20° to 65°, and there is no field data to verify the O, P, or D splay shape suggested in Martel and Boger (1998). It is interesting to note that the dihedral angle range is slightly less than the combined splay angle range.

There is pervasive chlorite-epidote mineralization in most fractures but no consistent pattern of quartz mineralization along the fractures. The mineralized quartz appears largely as lenses and there are only a few instances of a single continuous quartz vein filling fault. However, when the fractures wedged against each other, quartz was mineralized in the wedge (BJ-B and KJ-4). Through quartz was mineralized in the complex fault-step fractures, subsequent weathering created a rhombochasm and removed the quartz. Another place for quartz mineralization would be the accommodation space created at and near the fault kink of the KJ-1 fault group. There is also no consistent pattern between fault displacement and the width and length of quartz cavities. The largest quartz cavity has dimensions of 144 cm by 10 cm. Interestingly, the majority of observed splay fractures have little or no quartz present. From thin-section analysis, quartz mineralization in the field could be one of these three manifestations:

- 1) highly foliated quartz (BJS-2),
- 2) a large dynamically recrystallized quartz island, or
- 3) strain-free quartz fill (KJ4-296).

I did not observe any twisted fractures. In addition, there are no visible damaged zones near fault terminations or around the fault, and microstructural analysis of fault wall and secondary fractures did not reveal any consistent damaged zone. Rather, there are patchy areas of unbroken older fault gouge and zones of dynamically recrystallized wall rock along the fault wall.

## DISCUSSION

In this section, I present the synthesis of my observations and previous investigations. I begin with general comments on the observed faults and secondary features followed with comments on fluid flow in fractures, splay fractures with regards to mechanical models, and finally splay fractures with regards to three-dimensional conceptual models.

Some faults in the study area are the result of several discontinuous fractures connected through left- or right-lateral steps or direct contact. Left-lateral dilatant steps (splay fractures) are by far the most common form of fault linkage in this study. This type of fault linkage could be simple (one splay fracture link) to complex (fault step complex), and fault slip transfer between fault segments may have been accommodated by such linkages. Depending on the evolutionary stage of fault linkage and propagation, such dilatant linkages may not have accommodated any slip transfer, as seen in KJ4/296. The right-lateral compressive step is the counterpart of the left-lateral dilatant step. Alteration halos may not accompany dilatant fractures, but right-lateral steps are observed to have consistently deformed the fabric of the surrounding host rock. Bürgmann and Pollard (1994) concluded that the mechanism for such occurrences in the Lake Edison Granodiorite is crystal plasticity, and it would require increased shear stress at temperatures near the brittle-ductile transition.

Dilatant fractures and pressure solution seams are common in the strike-slip faults in Somerset Limestone (Willemse et al., 1997). Vermilye and Scholz (1998) postulated that for a Mode II shear crack, the greatest compressive stress makes lower angles with the crack plane in the compressive quadrants and higher angles in the tensile quadrants, resulting in an asymmetry of stresses across the fracture plane and in the direction of crack-tip propagation. However, such appearance of both



dilatant and compressive surfaces is rare in granite, and in this study only the Bear Creek fault group has this feature. The tensile quadrant fractures in the Bear Creek fault group fault step complex, along with their associated *S-C* fabrics in the compressive quadrant, seem to match Vermilye and Scholz's (1998) asymmetry.

From my observations, there are two types of rhomb-shaped features in the field: weathered/hollowed out and quartz-filled. I believe the fault step complex was a former hollowed out rhombochasm feature because the complex multiple dilatant fractures (with or without quartz mineralization) would suffer a greater rate of weathering than the single continuous intact quartz fill seen in a rhomb-wedge. Subsequent mechanical weathering created the rhombochasm.

From field and thin-section observations, I could find no other shear fracture growth model that fits other than the fracture-linked model (Segall and Pollard, 1983a; Martel et al., 1988; Martel, 1990) proposed for this study area. Under the fracture-link model, it assumes that the faults will not lengthen and the secondary fracture nucleation and propagation will accommodate all the stresses. It is counterintuitive that as the faults slip, they do not lengthen at all. Robeson (1998) suggested strain-softening, other fault dynamics, or regional stress fields (such as the Rosy Finch shear zone) might allow the faults to lengthen and interact to create the simple fault zones. The right-lateral shear zone in the region could have an effect on the remote stress field that could affect the local stress field, thus modifying the cohesive zone properties leading the varying of splay fracture angles. However, Christiansen and Pollard (1998) pointed out that the magnitude of local stress intensity was much higher than the Rosy Finch shear zone distributed stress and the shear zone might not have greatly affected the local deformation. If Tikoff et al. (1998) could constrain the timing of shearing, it could be responsible for the presence of secondary joint set in Reflecting Bowl and the kink bands in Kip Camp.

The competing process-zone model requires a zone of damaged rock surrounding the fault, and this was not observed in the field or in thin section. Models of Martel and Boger (1998) and Reches and Lockner (1994) have the same stress field shape associated with left-lateral fault slips. With the same stress field, Cooke (1997) and Martel and Boger (1998) suggested splay fracturing while Reches and Lockner (1994) did not have splay fracturing and instead produce tensile microcracks. My thin-section observations do not show the coalesce of microcracks for splay-fracture initiation and propagation. This raise two possibilities in fracture growth. The difference in fracturing could be the inhomogeneous structures between Lake Edison Granodiorite and Westerly Granite. The other possibility is there are two types of fracture mechanisms that could exist under the same stress field shape.

The clustering of splay fractures behind the fault tip suggests agreement with the Martel (1997) cohesive zone model. However, my observations are unable to verify whether the first splay fracture formed is furthest from the fault end and the last fracture formed closest to the end (Martel, 1997), or if the reverse order is true, as suggested by Granier (1985).

Long splay fractures that do not contact with the fault trace have risen the possibility that fractures could nucleate in a near distance from fault beside secondary fracture nucleation from the fault (Pollock and Evans, 1996; Kevin Hestir, 1998, personal commun.). My observations are unable to verify the original location of fracture nucleation.

Fracture spacing and fault spacing are not uniform. There are local regions of intense fracturing but they are tempered by dispersed fractures within the population. Segall and Pollard (1983b) have noted similar observations in their joint study. In sedimentary rock, a joint will restrain growth of other joints that are less than one layer thickness from the joint plane (Segall and Pollard, 1983b). Segall and Pollard

(1983b) reasoned the lack of uniform spacing in granitic rock was due to the fact that no layering exists and that the joint growth is not constrained by any preexisting mechanical property of the rock.

Along the line of the fracture population, the joint size power-law distribution has  $n = 1.2$ , which is within the range Segall and Pollard (1983b) reported for  $n$  of 1.2 to 1.8. The abundance of short joints relative to longer joints was probably the result of elastic interaction of adjacent joints (Segall and Pollard, 1983b). Shorter joints were prevented from further propagation by their longer siblings which consumed most of the strain energy in the rocks (Segall and Pollard, 1983b). However, detailing mapping of the Reflecting Bowl does not have the short joint ( $\leq 2$  m in length) frequency to satisfy the power-law distribution. Although Segall and Pollard (1983b) showed good fit on the power-law distribution for faults and joints, other distributions (e.g., log-normal distribution) could provide better fit (Kevin Hestir, 1998, personal commun.). I have opted to use Segall and Pollard (1983b) power-law distributions and results as the benchmark as there are no other comparable distributions for granitic rock. Further analysis on the joint and fault distributions might help settle the choice on distribution method. This could explain why as the sheared joints begin to link up, the power-law distribution for fault segments appears to break down. It seems likely that for the initial joint population modeling, the reported  $n$  range for the power-law distribution for joints is a good number to use. For the joints that became faults, the fracture-to-fault ratio is still elusive. It is still unclear why a single joint, within a group of joints, will become fault.

#### **Faults, Secondary Fractures, and Fluid Flow**

The hydrothermal alteration and mineralization along secondary fractures near

the fault trace ends are believed to be excellent fluid conduits (Long and Witherspoon, 1985). However, in this study, quartz mineralizations in splay fractures are few and far between. Nevertheless, this does not diminish the importance of secondary fractures in the hydraulic behavior of a fault system. A right-lateral compressive step, the counterpart of a left-lateral dilatant step, would be a poor fluid conduit. The quartz observed in the step could be a recrystallized quartz fragment trapped in the fault, as seen in thin section BJ28D. Bürgmann and Pollard (1994) concluded rock was vertically squeezed out of the right-lateral step. This probably resulted in thrust-fault motion and, in BJ28D, the fault wall was brittlely fractured as it approached the brittle-ductile transition. The fault wall and mylonite seem to create a trap for later fluid flow.

Quartz mineralization commonly can be seen in quartz wedges where two fault segments are in direct contact and push on each other to accommodate fault slip. Such a feature will be a great boon for fluid flow, and field observation has confirmed this. The amount of quartz found in these wedges could easily outstrip the total amount of quartz found in all the faults. Other good locations for fluid migration would be the fault step complex, owing to the multiple dilatant fractures and the voids in the kink band hinges.

The limited length, confined width, and lack of continuous veins of quartz mineralization indicate there is little or no fluid movement along the length and sides of the fault. The dynamically recrystallized fault wall seen in the thin sections will lower the hydraulic conductivity across a fault more than the conductivity parallel to the fault. The only explanation for this is vertical fluid migration through the fault. This supports the notion of chimneys oriented normal to the slip direction with limited anisotropic and channeled fluid flow along the fault (Martel and Boger, 1998). Bürgmann and Pollard (1994) found no preferential quartz loss opposite secondary

fractures, rejecting the notion that localized elevated mean compressive stress might have liberated quartz from the host rock by pressure solution.

The distribution of quartz in faults and the lack of quartz in joints suggest that when the joints were sheared, the reconfigured fracture network probably tapped into a previously untouchable quartz-rich fluid source. After faulting occurs, there is inherent roughness in the fault. Fluid migration may have to negotiate through generations of fault gouge, that may or may not be completely obliterated by faulting, and newly incorporated fault-wall fragments. The distribution pattern of quartz suggests most of the quartz-rich fluid migrated tubularly and not in sheet-like action.

The secondary joint set in Reflecting Bowl could have provided another flow path and it might have before the arrival of quartz in the system. Since only epidote-chlorite is found in these joints, it implies that the secondary joint set has a limited role in the fractured system fluid flow.

In this study, there is no correlation with cavity size and fault displacement; hence, fault size does not have a direct relationship with fluid flow. It is rather the connectivity and permeability of a fault system that determines its fluid flow capability.

### **Splay-Fracture Geometry and Fault Mechanical Models**

My field observation for the mean and standard deviation angle for all splay fractures is  $39^\circ \pm 13^\circ$ , which is slightly higher than the earlier study splay angle of  $25^\circ \pm 10^\circ$  (Segall and Pollard, 1983a). Both results are well below the LEFM theoretical splay angle (Segall and Pollard, 1987) and within the CZT theoretical realm (Martel, 1997).

Segall and Pollard (1987) calculated the theoretical crack-orientation for the strike-slip fault secondary fractures based on LEFM. With uniform load [where

stresses do not vary with the spatial location (Segall and Pollard (1987)] under Mode II conditions, the theoretical angle intersects the fault trace at about  $70^\circ$ . This angle is independent of the principal compressive stress and shear driving stress (Martel, 1997). The theoretical angle does not correlate well with previous studies (Segall and Pollard, 1983a; Granier, 1985; Cruikshank et al., 1991) and this study's field observations of many faults.

Another major attempt to account for the secondary fracture orientations was the "Moab rule" by Cruikshank et al. (1991) based on the LEFM in a mixed-mode of I + II. They assumed the faults were under uniform stress and the secondary fractures opened perpendicular to the greatest circumferential stress near the fault tip. Cruikshank et al. (1991) further related the secondary fracture orientations to the ratio of fault aperture to slip. In their analysis, they concluded that for the observed splay angle of  $25^\circ$  to  $50^\circ$ , the ratio of slip to aperture would be about 2 to 3 times. This conclusion does not hold well for the other faults. In Martel et al. (1988) and this study, some faults have several meters of slip yet the faults are only 1 cm thick. The aperture of the fault opening to slippage is well below the proposed ratio.

The earlier models would create a singular infinite stress at the fault tip if the stress load were uniform, which is unrealistic. Martel (1997) proposed that a cohesive zone at the fault tip behaves plastically, leading the stress near the fracture end zone to be finite. This would account for a nonuniform stress drop when the fault slips, which eliminates the singularity problem. The LEFM models could not account for secondary fracturing along the fault trace behind fault tip, and they allow for only one secondary fracture at the fault tip, which is contrary to field observations (Martel, 1997). Martel's (1997) CZT model is able to account for observed secondary fracture orientations, number, and distribution without any aperture change.

Cooke (1997) has summarized the four leading mechanisms for the growth of multiple splay fractures along a fault:

- 1) multiple slip events produce splay fractures which mark the locations of previous slip-patch terminations (Martel et al., 1988);
- 2) existing fracture filling combined with continued slip promotes adjacent rock fracturing;
- 3) the rise of regions of local stress concentration resulting from purely planar slip surface deviations could subsequently initiate multiple splay fractures (Cooke and Pollard, 1996); and
- 4) the reduction of fault-tip stress singularity allows the development of multiple splay fractures away from fault tip (Martel, 1997).

The flaw in the Martel et al. (1988) slip-patch theory, originally developed for fault step complexes, is the requirement of two fault slip patches to overlap in order to trigger splay-fracture nucleation on both faults (Fig. 66). Field studies have abundant evidence in which splay fractures were formed without any nearby faults developing secondary fractures (Martel et al., 1988; Evans et al., 1996). An interesting observation arising from the theory is that a single slip event would produce a pair of splay fractures, and by counting the number of splay fracture pairs, we could have the number of slip events that occurred.

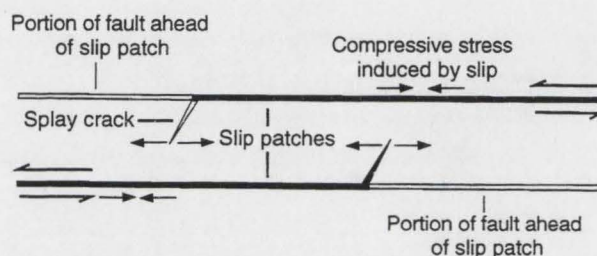


**Figure 66. Left-lateral slip patches that have induced splay cracks on an adjacent fault. Modified from Martel and Pollard (1989).**

Field observations are unable to establish any correlation between fracture filling (quartz or epidote-chlorite) and splay-fracture nucleation. There are possibilities in which the nucleation site fracture filling would reveal more clues under the microscope than to unaided eyes, or certain compositions or shapes of the fracture filling at depth could initiate splay fracturing. Thin-section analysis of KJ1/396 has not revealed any peculiar fracture filling at the nucleation site.

As for the rise of regions of local stress concentration resulting from purely planar slip surface deviations, in order for multiple secondary fractures to occur, a mixed mode of I + III is required (Cooke and Pollard, 1996). Such mixed mode produces either twisting or curving fractures, which is not supported by the field observations.

For the stress singularity problem, CZT may provide a solution. On top of the singularity dilemma, the LEFM is only capable of predicting the initiation and propagation of a single splay fracture. With the CZT model, LEFM could be a special case under CZT. Willemse and Pollard (1998) have found that the overall energy budget for the LEFM and CZT is identical if the CZT end zone is very small and the LEFM singularity extends over a very small area. In addition, flaw length, propagation, and mechanical interaction with neighboring flaws are very similar for both CZT and LEFM flaws (Willemse and Pollard, 1998). Martel (1997) has demonstrated the theoretical possibility of multiple splay fractures using CZT. Under linearly increasing end zone friction strength, the CZT could produce either single or multiple splay fractures depending on the maximum end zone friction coefficient (Cooke, 1997).

Cooke (1997) suggested that lithologic variations, nearby structure interactions, irregular fault geometries, fluid presence, temperature, and other factors could create spatially varying friction along a fault that would promote a zone of



potential splay crack localization. Cooke (1997), after going through the literature on friction in regard to fault surface roughness, fault gouge grain size, and fault gouge thickness, concluded that as a fault accumulates slip, the effective friction coefficient of the fault material is reduced due to decreased fault surface roughness, decreased fault gouge grain size, and/or increased fault gouge thickness. Based on my observations of the patchy mineralization on the fault, it could create a heterogeneous friction surface that could fulfill the conditions for Cooke's (1997) spatial variation of friction along a fault.

Wintsch et al. (1995), after reviewing the literature, concluded that it is highly unlikely that high fluid pressure could occur under strike-slip faulting conditions. Wintsch et al. (1995) advocated that a well-developed phyllosilicate fabric and the replacement of stronger framework silicates by weaker phyllosilicates during fluid-rock reaction could significantly lower the fault friction coefficient. Gottschalk et al. (1990) examined microstructures in sheared gneiss and found that the deformation of favorably oriented micas appeared to have led to local stress concentration that resulted in tensile microcrack nucleation. The throughgoing cracks noted by Gottschalk et al. (1990) in their samples were formed by the coalescence of microcracks in feldspar and quartz grains. This seems to suggest that two different processes have to take place in order for a fracture to nucleate and propagate. The observed presence of biotite at one of the junctions between splay fracture and fault could lend support to hypotheses of Gottschalk et al. (1990) and Wintsch et al. (1995).

Cooke (1997) also postulated that a zone of potential fracture development may nucleate multiple splay fractures, but that they will have to compete against each other to propagate away from the fault. There would be a decrease in splay fracture

density with increasing perpendicular distance to the fault (Cooke, 1997), and this is observed in this study.

### **Splay-Fracture Geometry and Three-Dimensional Conceptual Models**

Three-dimensional conceptual models were introduced earlier and a brief overview in light of the data presented here is provided. Martel and Boger (1998) constructed a CZT-based conceptual model (CZT model) for three-dimensional strike-slip faults (Fig. 2). The other conceptual models for three-dimensional strike-slip fault and their secondary fractures that are based on previous experiments are illustrated in Figure 1 (Adams and Sines, 1978; Germanovich et al., 1994; Scholz, 1990). All models share these similar secondary fracture characteristics:

- 1) The fractures touch the perimeters of the penny-shaped fracture.
- 2) The fractures at the propagation tips are larger than the fractures along the edges.
- 3) The fractures are about parallel to the axis of maximum compression.

All models except the CZT model have a significant portion of the fault intersected by the larger fractures and the fractures form a continuous curved surface. Martel and Boger (1998) reasoned that neither Adams and Sines (1978) nor Germanovich et al. (1994) applied a sufficiently large triaxial compressive load to close the shear fracture, which led to a large stress drop and formed the continuous curved secondary fractures near 3 and 9 o'clock. In the Germanovich et al. (1994) case, the laser-cutting residual in the penny-shaped fracture might have acted as lubricant and caused a large stress drop (Martel and Boger, 1998). Currently, there are no data to forbid a curvilinear splay fracture plane.

Both Figures 1a and 1b have no zipper crack band and Figure 1c cannot have zipper crack bands without a central fracture. In addition, secondary fractures in

Figures 1a and 1b do not propagate across the fault plane. The fact that secondary fractures do not propagate past the fault plane in Adams and Sines (1978) could be due to the penny-shaped fracture seam (Martel and Boger, 1998).

The Martel and Boger (1998) CZT model is the only one that could account for all of the field observations. It could account for multiple discontinuous secondary fractures near the end of a fault and could support the presence of secondary fractures past the end of a fault. Although no zipper crack band is reported in this study, it should be included in the CZT model, as it was reported in previous observations (Martel et al., 1988; Robeson, 1998). The CZT allows Martel and Boger (1998) to model secondary fractures that propagate across the fault (Willemse and Pollard, 1998), and accounts for zipper crack bands both with and without a central fracture. It could also allow for dipping splay-fracture planes, as seen in SF-1 fault-wall traces and in SF-2 and other end-view structures' dihedral angles. This study's observations and data in combination with the improving Martel and Boger (1998) CZT-based model are being conditionally coded and adapted for use in a stochastic model, developed by Hestir et al. (1997). The distribution of fault and fracture sizes and other statistical parameters are being used to condition the statistical model to match the field data, and it will result in a three-dimensional visualization of a fault and its associated fractures (Fig. 67) (Hestir et al., 1997).

Current research is unclear on how well a fracture could retain its shape when it encounters or overlaps other fractures during growth. Aydin and Schultz (1990) concluded that mechanical interaction impedes the amount of segment overlap, but CZT allows faults to overlap for significant distances before impeding each other's growth, even if they are closely spaced (Willemse, 1997). The mechanical interaction of a fault is influenced by the three-dimensional fault shape, the spatial arrangement of multiple segments, and the shear strength distribution along the fault

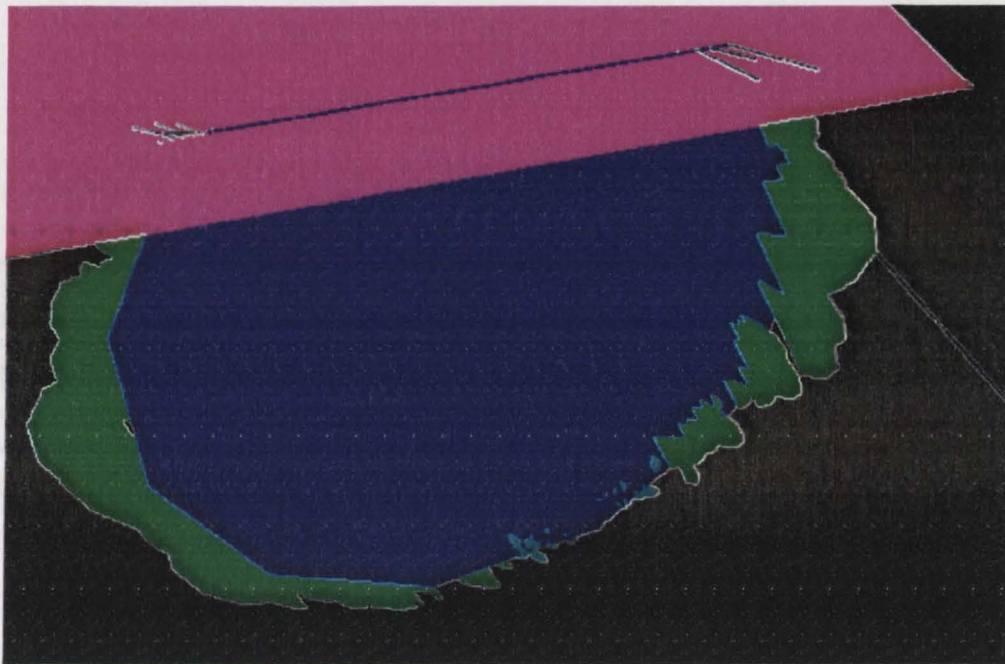


**Figure 67. A fully rendered fault plane and splay fractures fitting the surface trace of a strike-slip fault and its secondary fractures. From Hestir et al. (1997).**

(Willemse, 1997). Nicol et al. (1996) has demonstrated how fault growth restrictions can affect the shape of a fault (Fig. 7). This issue has to be resolved before a truly accurate three-dimensional strike-slip fault can be depicted. After raising the issue of the shape problem, the basic assumption of penny fractures used in mechanical modeling is not without merit. A circular shape is a special case of an ellipse, and it is easy to construct a basic model for testing before venturing out into more complex shapes. The surrounding pluton geobarometries have indicated that if a fracture should initiate at depth, it would be circular or elliptical elongate in the horizontal direction, rather than a vertically elongated ellipse. Nicol et al. (1996) have shown that a crack initiates as a penny and later elongates into an elliptical fracture. Based on my data, it is still very difficult to ascertain the true three-dimensional shape of a strike-slip fault and the shapes of its secondary fractures.

Current modeling efforts are unable to reproduce an undulating chord as

dictated by the field data and they cannot predict the chord of a fault without any splays. The current CZT model also assumes a penny shape for the fault, O, P, and D shapes for splay fractures, and uniform fault width. A better model is needed for the effect of elastic field interaction on fracture shape, as well as for a model for right-lateral deformation. Although multiple-segment faults have behaved like a single fault, there are still certain subtle differences for which the CZT model has yet to account, such as the difference in between the maximum perpendicular distances for the north and south blocks of fault KJ-4. While the CZT could allow for single or multiple secondary fractures, it does not explain why more than half of the studied faults do not have splay fractures. Maybe the faults have propagated in-plane without splaying and this begs more questions as to under what conditions do faults propagate in-plane or splay.

This study has collected three-dimensional field data, such as the geometry of fractures, distribution and size of fractures, and mineralization features, in order to model the three-dimensional structure of strike-slip faults. Field observations have reaffirmed the fracture-linked model for the evolution of faults in the Lake Edison Granodiorite (Segall and Pollard, 1983a; Martel et al., 1988), and have provided additional insight into the proposed vertical fluid circulation model for the fault (Bürgmann and Pollard, 1994; Martel and Boger, 1998). The current fracture mechanics research has shown the CZT to be a far superior mechanical model in comparison to LEFM. This study has also found Martel and Boger's (1998) CZT-based model to be the most promising three-dimensional strike-slip conceptual model.

## CONCLUSIONS

The three-dimensional geometry and the mechanics of small strike-slip faults are not well understood because of the lack of pertinent field data. Close examination of small strike-slip faults and their splay fractures, combined with observations of fracture filling, is crucial to understanding the three-dimensional properties of strike-slip faults. Detailed mapping of the splay fractures has yielded a great wealth of geometrical information (dihedral angle, splay angle, splay-fracture dip, splay-fracture spacing, and splay tracelength). The splay-fracture angle is  $39^\circ \pm 13^\circ$  and the dihedral angle of the splay plane and the fault plane ranges from  $20^\circ$  to  $65^\circ$ . All splay-fracture traces are linear at depth and on the surface, and splay fractures could also bifurcate and could have en-echelon features. Less than half of the faults have splay fracturing. There generally is a high concentration of near-fault splay fractures with 5–15 cm spacing, while the fracture spacing far from the fault is more disperse. As perpendicular distance increases from a fault, there is a pattern of wider splay spacing and fewer splay fractures. The splay tracelength distribution charts have high concentrations of short tracelengths (20, 30, or 40 cm, depending on the splay groups) with a rapid decrease in the number of long tracelengths. The maximum tracelength of multiple splay-fracture groups is restricted by their distance orthogonal to the fault trace. There are an apparent increase in splay tracelength towards fault ends and an apparent decrease in splay angle towards fault ends. The decreasing splay angle near fault ends has restricted the splay-fracture damage zone from widening even though the splay tracelength has increased towards the fault ends. All this information has been used to delineate the three-dimensional relationship between the splay-fracture planes and the fault plane, and to help with the continued development and refinement of three-dimensional mechanical models.

In turn, the three-dimensional geometry, along with the observed quartz cavity distribution and thin-section analysis, has led to the conclusion that a vertical fluid migration system exists among the faults and fractures. The connectivity and permeability of a fault system determine its fluid flow capability, and fault size does not have a direct relationship with fluid flow.

The joint size estimate for the initial joint population is represented by the power-law distribution of joints. The joint power-law distribution of this study agrees with the  $n$  range reported by Segall and Pollard (1983b) for granitic rock, but there are poor fault-segment power-law distribution correlations. The data on fracture and fault spacing, along with the joint power-law distribution, will aid in the creation of a starting joint size population for further simulation and analysis of fault evolution.

## REFERENCES

- Adams, M., and Sines, G., 1978, Crack extension from flaws in a brittle material subject to compression: *Tectonophysics*, v. 48, p. 87-117.
- Anders, M., and Wiltschko, D.V., 1994, Microfracturing, paleostress and the growth of faults: *Journal of Structural Geology*, v. 16, p. 795-816.
- Aydin, A., and Schultz, R.A., 1990, Effect of mechanical interaction in the development of strike-slip faults with echelon patterns: *Journal of Structural Geology*, v. 12, p. 123-129.
- Barenblatt, G.I., 1962, The mathematical theory of equilibrium cracks in brittle fracture: *Advances in Applied Mechanics*, v. 7, p. 55-129.
- Barnett, J.A.M., Mortimer, J., Rippon, J.H., Walsh, J.J., and Watterson, J., 1987, Displacement geometry in the volume containing a single normal fault: *American Association of Petroleum Geologists Bulletin*, v. 71, p. 925-937.
- Bateman, P.C., 1992, Plutonism in the central part of the Sierra Nevada batholith, California: U. S. Geological Survey Professional Paper 1483, 186 p.
- Bateman, P.C., and Wahrhaftig, C., 1966, Geology of Sierra Nevada, *in* Baily, E.H., ed., *Geology of northern California: Bulletin of California Division of Mines Geology*, v. 190, p. 107-172.
- Brace, W.F., and Bombolakis, E.G., 1963, A note on brittle crack growth in compression: *Journal of Geophysical Research*, v. 68, p. 3709-3713.
- Broek, D., 1986, *Elementary engineering fracture mechanics*: Norwell, Massachusetts, Klumer Academics, 516 p.
- Bürgmann, R., and Pollard, D.D., 1994, Strain accommodation about strike-slip fault discontinuities in granitic rock under brittle-to-ductile conditions: *Journal of Structural Geology*, v. 16, p. 1655-1674.



- Christiansen, P.P., and Pollard, D.D., 1998, Nucleation growth and structural development of mylonitic shear zones in granitic rocks: Reply: *Journal of Structural Geology*, v. 20 (in press).
- Cooke, M., 1997, Fracture localization along fault with spatially varying friction: *Journal of Geophysical Research*, v. 102, p. 22425-22434.
- Cooke, M., and Pollard, D.D., 1996, Fracture propagation paths under mixed mode loading within rectangular blocks of polymethyl methacrylate: *Journal of Geophysical Research*, v. 101, p. 3387-3400.
- Cowie, P.A., and Scholz, C.H., 1992, Physical explanation for the displacement-length relationship of faults using a post-yield fracture mechanics model: *Journal of Structural Geology*, v. 14, p. 1133-1148.
- Cox, S.J.D., and Scholz, C.H., 1988, On the formation and growth of faults: an experimental study: *Journal of Structural Geology*, v. 10, p. 413-430.
- Cruikshank, K.M., Zhao, G., and Johnson, A.M., 1991, Analysis of minor fractures associated with joints and faulted joints: *Journal of Structural Geology*, v. 13, p. 865-886.
- Davies, R.K., and Pollard, D.D., 1986, Strike-slip faults and monoclinical kink bands: *Pure and Applied Geophysics*, v. 124, p. 177-201.
- Dugdale, D.S., 1960, Yielding of steel sheets containing slits: *Journal of the Mechanics and Physics of Solids*, v. 8, p. 100-104.
- Engel, L., Klingele, H., Ehrenstein, G.W., and Schaper, H., 1981, An atlas of polymer damage: Surface examination by scanning electron microscope (translated by Welling, M.S.): Englewood Cliff, New Jersey, Prentice-Hall Inc., 256 p.

- Evans, J.P., Martel, S.J., and Yang Junming, 1996, Three-dimensional structure, mineralization, and fluid flow along small strike slip faults in granite: Geological Society of America Abstracts with Programs, v. 28, no. 7, p. A-135.
- Evernden, J.F., and Kistler, R.W., 1970, Chronology of emplacement of Mesozoic batholithic complexes in California and western Nevada: U.S. Geological Survey Professional Paper 623, 42 p.
- Germanovich, L.N., Salganik, R.L., Dyskin, A.V., and Lee, K.K., 1994, Mechanisms of brittle fracture of rock with pre-existing cracks in compression: Pure and Applied Geophysics, v. 143, p. 117-148.
- Gottschalk, R.R., Kronenberg, A.K., Russell, J.E., and Handin, J., 1990, Mechanical anisotropy of gneiss: Failure criterion and textural sources of directional behavior: Journal of Geophysical Research, v. 95, p. 21613-21634.
- Granier, T., 1985, Origin, damping, and pattern of development of faults in granite: Tectonics, v. 4, p. 721-737.
- Hestir, K., Yang Junming, Evans, J.P., Martel, S.J., Long, J.C.S., and Jacobsen, J., 1997, A mechanically based stochastic model for a fault zone conditioned on field data: Geological Society of America Abstracts with Programs, v. 29, no. 6, p. A-198.
- Kistler, R.W., Bateman, P.C., and Brannock, W.W., 1965, Isotopic ages of minerals from granitic rocks of the central Sierra Nevada and Inyo Mountains, California: Geological Society of America Bulletin, v. 76, p. 155-164.
- Kulander, B.R., Dean, S.L., and Ward, B.J. Jr, 1990, Fractured core analysis: Interpretation, logging, and use of natural and induced fractures in core: Tulsa, Oklahoma, America Association of Petroleum Geologists Methods in Exploration Series, No. 8, 88 p.

- Lawn, B., 1993, *Fracture of brittle solids* (second edition): New York, Cambridge University Press, 378 p.
- Lockner, D.A., Byerlee, J.D., Kuksenko, V., Ponomarev, A., and Sidorin, A., 1991, Quasi-state fault growth and shear fracture energy in granite: *Nature*, v. 350, p. 39-42.
- Lockwood, J.P., and Lydon, P.A., 1975, Geologic map of the Mount Abbot quadrangle, central Sierra Nevada, California: U.S. Geological Survey Geologic Quadrangle GQ-1155, scale 1:62,500, 1 sheet, 6 p. text.
- Long, J.C.S., and Witherspoon, P.A., 1985, The relationship of the degree of interconnection to permeability in fracture networks: *Journal of Geophysical Research*, v. 90, p. 3087-3097.
- Martel, S.J., 1990, Formation of compound strike-slip fault zones, Mount Abbot quadrangle, California: *Journal of Structural Geology*, v. 12, p. 869-882.
- Martel, S.J., 1997, Effects of cohesive zones on small faults and implications for secondary fracturing and fault trace geometry: *Journal of Structural Geology*, v. 19, p. 835-849.
- Martel, S.J., and Boger, W.A., 1998, Geometry and mechanics of secondary fracturing around small three-dimensional faults in granitic rock: *Journal of Geophysical Research*, v. 103, p. 21299-21314.
- Martel, S.J., and Evans, J.P., 1996, Structure of a Sierra Nevada fault zone and hydrologic implications: *Geological Society of America Abstracts with Programs*, v. 28, no. 7, p. A-135.
- Martel, S.J., and Pollard, D.D., 1989, Mechanics of slip and fracture along small faults and simple strike-slip fault zones in granitic rock: *Journal of Geophysical Research*, v. 94, p. 9417-9428.

- Martel, S.J., Pollard, D.D., and Segall, P., 1988, Development of simple strike-slip fault zones, Mount Abbot quadrangle, Sierra Nevada, California: *Geological Society of America Bulletin*, v. 100, p. 1451-1465.
- Moore, D.E., and Lockner, D.A., 1995, The role of microcracking in shear-fracture propagation in granite: *Journal of Structural Geology*, v. 17, p. 95-114.
- Nicol, A., Watterson, J., Walsh, J.J., and Childs, S., 1996, The shapes, major axis orientations and displacement patterns of fault surfaces: *Journal of Structural Geology*, v. 18, p. 235-248.
- Noyes, H.J., Wones, D.R., and Frey, F.A., 1983, A tale of two plutons: Petrographic and mineralogic constraints on the petrogenesis of the Red Lake and Eagle Peak plutons, central Sierra Nevada, California: *Geology*, v. 91, p. 353-379.
- Passchier, C.W., and Trouw, R.A.J., 1996, *Microtectonics*: New York, Springer-Verlag, 289 p.
- Pollard, D.D., and Aydin, A., 1988, Progress in understanding jointing over the past century: *Geological Society of America Bulletin*, v. 100, p. 1171-1204.
- Pollock, C.J., and Evans, J.P., 1996, Physical modeling of fault zone evolution from joints reactivated as left-lateral strike-slip faults: *Geological Society of America Abstracts with Programs*, v. 28, no. 7, p. A-245.
- Reches, Z., and Lockner, D.A., 1994, Nucleation and growth of faults in brittle rocks: *Journal of Geophysical Research*, v. 99, p. 18159-18173.
- Reed, W.E., and Hathaway, G.M., 1994, The Long Lake shear zone: implications for dextral sense shear zones in the Sierra Nevada batholith, east-central California: *Geological Society of America Abstracts with Programs*, v. 26, no. 7, p. A-385.

- Renne, P.R., Tobisch, O.T., and Saleeby, J.B., 1993, Thermo-chronologic record of pluton emplacement, deformation, and exhumation at Courtright shear zone, central Sierra Nevada, California: *Geology*, v. 21, p. 331-334.
- Robeson, K.R., 1998, Three-dimensional structure of small strike-slip fault zones in granitic rock: Implications for fault-growth models [Master's thesis]: Logan, Utah State University, 217 p.
- Rudnicki, J., 1980, Fracture mechanics applied to the earth's crust: *Annual Review of Earth and Planetary Sciences*, v. 8, p. 489-525.
- Scholz, C.H., 1990, *The mechanics of earthquakes and faulting*: New York, Cambridge University Press, 437 p.
- Segall, P., and Pollard, D.D., 1983a, Nucleation and growth of strike slip faults in granite: *Journal of Geophysical Research*, v. 88, p. 555-568.
- Segall, P., and Pollard, D.D., 1983b, Joint formation in granitic rock of the Sierra Nevada: *Geological Society of America Bulletin*, v. 94, p. 563-575.
- Segall, P., and Pollard, D.D., 1987, Theoretical displacements and stresses near fractures in rocks: with applications to faults, joints, veins, dikes, and solution surfaces, *in* Atkinson, B.K., ed., *Fracture mechanics of rock*: London, Academic Press, p. 277-349.
- Segall, P., McKee, E.H., Martel, S.J., and Turrin, B.D., 1990, Late Cretaceous age of fractures in the Sierra Nevada batholith: *Geology*, v. 17, p. 1247-1251.
- Segall, P., and Simpson, C., 1986, Nucleation of ductile shear zones on dilatant fractures: *Geology*, v. 14, p. 56-59.
- Smith, L., Forster, C.B., and Evans, J.P., 1990, Interaction between fault zones, fluid flow and heat transfer at the basin scale, *in* Newman, S.P., and Neretnieks, I., eds., *Hydrogeology of low permeability environments*: International

Association of Hydrological Sciences selected papers in hydrogeology, v. 2, p. 41-67.

- Stern, T.W., Bateman, P.C., Morgan, B.A., Newall, M.F., and Peck, D.L., 1981, Isotopic U-Pb ages of zircon from the granitoids of the central Sierra Nevada, California: U. S. Geological Survey Professional Paper 1185, 17 p.
- Tikoff, B., and Saint Blanquat, M., 1997, Transpressional shearing and strike-slip partitioning in the Late Cretaceous Sierra Nevada magmatic arc, California: *Tectonics*, v. 16, p. 442-459.
- Tikoff, B., Teyssier, C., and Saint Blanquat, M., 1998, Nucleation growth and structural development of mylonitic shear zones in granitic rocks: Discussion: *Journal of Structural Geology*, v. 20 (in press).
- Tobisch, O.T., Renne, P.R., and Saleeby, J.B., 1993, Deformation resulting from regional extension during pluton ascent and emplacement, central Sierra Nevada, California: *Journal of Structural Geology*, v. 15, p. 609-628.
- Tobisch, O.T., Saleeby, J.B., Renne, P.R., McNully, B., and Tong Weixing, 1995, Variations in deformation fields during development of a large-volume magmatic arc, central Sierra Nevada, California: *Geological Society of America Bulletin*, v. 107, p. 148-168.
- Twiss, R.J., and Moores, E.M., 1992, *Structural geology*: New York, W.H. Freeman and Company, 532 p.
- Vermilye, J.M., and Scholz, C.H., 1998, The process zone: A microstructural view of fault growth: *Journal of Geophysical Research*, v. 103, p. 12223-12237.
- Wintsch, R.P., Christoffersen, R., and Kronenberg, A.K., 1995, Fluid-rock reaction weakening of fault zones: *Journal of Geophysical Research*, v. 100, p. 13021-13032.

- Willemse, E.J.M., 1997, Segmented normal faults: Correspondence between three-dimensional mechanical models and field data: *Journal of Geophysical Research*, v. 102, p. 675-692.
- Willemse, E.J.M., and Pollard, D.D., 1998, On the orientation and patterns of wing cracks and solution surfaces at the tips of a sliding flaw or fault: *Journal of Geophysical Research*, v. 103, p. 2427-2438.
- Willemse, E.J.M., Peacock, D.C.P., and Aydin, A., 1997, Nucleation and growth of strike-slip faults in limestone from Somerset, U.K.: *Journal of Structural Geology*, v. 19, p. 1461-1477.
- Yielding, G., Freeman, B., and Needham, D.T., 1997, Quantitative fault seal prediction: *American Association of Petroleum Geologists Bulletin*, v. 81, p. 897-917.
- Zheng Jinsong, 1995, A computer program for visualization of three-dimensional fractures [Master's thesis]: Logan, Utah State University, 35 p.

APPENDICES



Appendix A

Three-Dimensional Data Computation

### Three-Dimensional Data Computation

In order to demonstrate the three-dimensional data computation, a walkthrough example is used here to help facilitate the calculation.

A photocopy of a field map was made and slope breaks were marked (Fig. A1). An arbitrary labeling system was employed to identify points along the mapped fractures in which a change in fault geometry (x-, y-, z-direction) occurred. I found that it is more efficient to calculate the three-dimensional data for all slope breaks before calculating any data points, and this will become self-evident later. In this example, in the x-direction, from origin to 84 cm the slope angle is  $4^\circ$  and this is the first slope break on the map (sb1). The second slope break (sb2) is at  $x = 110$  cm, and there is a  $-22^\circ$  slope angle between 84 cm and 110 cm. With the respect to y-direction, the entire fault is tilted at an angle of  $3^\circ$ .

Using the information given above, the three-dimensional data ( $x'$ ,  $y'$ ,  $z'$ ) for point sb1 is computed based on the methods below:

Slope distance of point sb1 to origin (SD): 84 cm

Conversion of field x-direction (x) to true x ( $x'$ ):

$$X' = SD \cos \alpha = 84 \text{ cm} * \cos 4^\circ = 83.795 \text{ cm}$$

Conversion of field y-direction (y) to true y ( $y'$ ):

$$Y' = SD \cos \beta = 0.0 \text{ cm} * \cos 3^\circ = 0 \text{ cm}$$

Elevation (z):

$$Z' = SD \sin \alpha + SD \sin \beta = 84 \text{ cm} \sin 4^\circ + 0.0 \text{ cm} \sin 3^\circ$$

$$Z' = 5.860 \text{ cm}$$

Three-dimensional data ( $x'$ ,  $y'$ ,  $z'$ ) for point sb1 = (83.80, 0.0, 5.86) cm

For point sb2,

Slope distance from sb1 to sb2 (SD): 26 cm

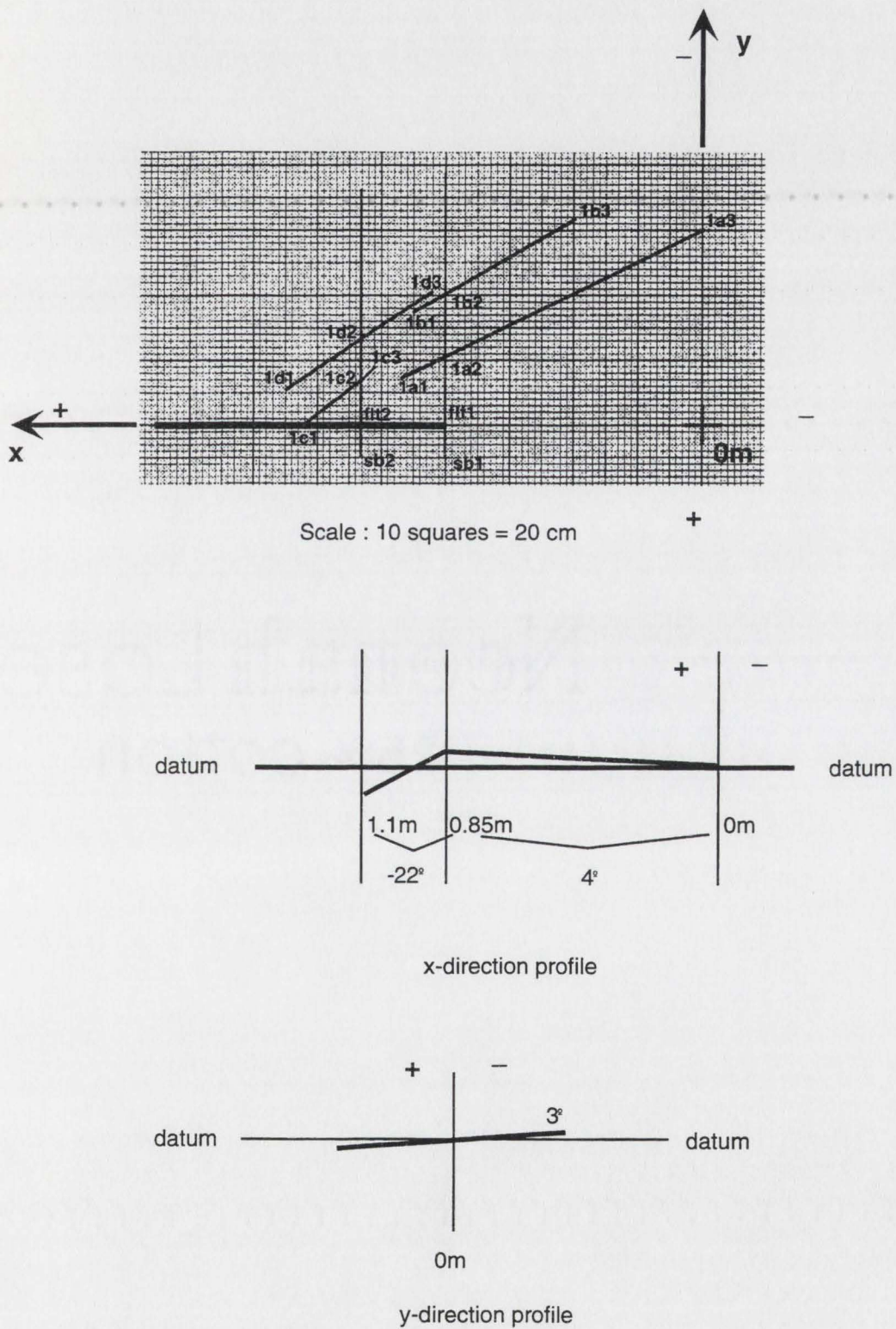


Figure A1. A fracture trace diagram with markings and x and y profiles of the topography.

Conversion of field x-direction (x) to true x (x'):

$$X' = SD \cos \alpha = 26 \text{ cm} * \cos -22^\circ = 24.107 \text{ cm}$$

Conversion of field y-direction (y) to true y (y'):

$$Y' = SD \cos \beta = 0.0 \text{ cm} * \cos 3^\circ = 0.0 \text{ cm}$$

Elevation (z):

$$Z' = SD \sin \alpha + SD \sin \beta = 26 \text{ cm} * \sin -22^\circ + 0.0 \text{ cm} \sin 3^\circ$$

$$Z' = -9.740 \text{ cm}$$

The above calculation for sb2 assumed point sb1 to be the origin; hence, to get the three-dimensional data (x', y', z') for point sb2, the above calculation has to add the x' and z' values of sb1.

$$X' = SD \cos \alpha + x' \text{ of sb1} = 24.107 \text{ cm} + 83.795 \text{ cm} = 107.902 \text{ cm}$$

$$Z' = SD \sin \alpha + SD \sin \beta + z' \text{ of sb1} = -9.740 \text{ cm} + 5.86 \text{ cm} = -3.880 \text{ cm}$$

$$Sb2 = (107.90, 0.0, -3.88) \text{ cm.}$$

In this example, the fault happened to begins at flt1(x, y)=(84, 0.0) cm; hence, the x', y' and z' of flt1 = (83.80, 0.0, 5.86) cm. The fault continues through sb2, and the x', y', and z' of flt2 = (107.90, 0.0, -3.88) cm.

To expedite calculations, a spreadsheet named *xyzcal.xls* was created and the rest of the example data points are calculated and tabulated below.

Slope change at 0

x angle	4°	x value	0
y angle	3°	z value	0

pt name	x	y	SD	x'	y'	z'
flt1	84	0	84.000	83.795	0.000	5.860
1a2	84.000	-19.000	84.000	83.795	-18.974	6.854
1a3	0.000	-60.000	0.000	0.000	-59.918	3.140
1b2	84.000	-38.000	84.000	83.795	-37.948	7.848
1b3	40.000	-63.000	40.000	39.903	-62.914	6.087
1d3	84.000	-40.000	84.000	83.795	-39.945	7.953

## Slope change at 84

x angle	-22°	x value	83.795
y angle	3°	z value	5.86

pt name	x	y	SD	x'	y'	z'
flt2	110.000	0.000	26.000	107.902	0.000	-3.880
1a1	94.000	-15.000	10.000	93.067	-14.979	2.899
1b1	90.000	-35.000	6.000	89.358	-34.952	5.444
1c2	110.000	-11.000	26.000	107.902	-10.985	-3.304
1c3	106.000	-14.000	22.000	104.193	-13.981	-1.649
1d2	110.000	-23.000	26.000	107.902	-22.968	-2.676

## Slope change at 110

x angle	-6°	x value	107.902
y angle	3°	z value	-3.88

pt name	x	y	SD	x'	y'	z'
1c1	124.000	0.000	14.000	121.825	0.000	-5.343
1d1	139.000	-11.000	29.000	136.743	-10.985	-6.336

$$SD=B36-SC\$29$$

$$x'=D36*\text{COS}(\text{RADIANS}(\$C\$30))+\$F\$30$$

$$y'=C36*\text{COS}(\text{RADIANS}(\$C\$31))$$

$$z=D36*\text{SIN}(\text{RADIANS}(\$C\$30))+\$F\$31+C36*\text{SIN}(\text{RADIANS}(\$C\$31))$$

All the above units are in centimeters.

Appendix B

Ribbon Diagram Color Code

<b>Color</b>	<b>Representation</b>
Yellow	Fault
Green	Covered fault
Orange	Assumed fault
Red	Offset indicators
Light Blue	Covered dike
Pink	Splay cracks